Diagrammatic Monte Carlo: recent developments and applications to the Hubbard model

Michel Ferrero

INSTITUT POLYTECHNIQUE DE PARIS

ÉCOLE POLYTECHNIQUE

IP PARIS

Habilitation à diriger des recherches

Diagrammatic Monte Carlo: recent developments and applications to the Hubbard model

Habilitation à diriger des recherches
de l'Institut Polytechnique de Paris
Spécialité : Physique

Habilitation soutenue à Paris, le 7 juin 2023, par

Michel Ferrero

Composition du jury :

André-Marie Tremblay Professeur, University of Sherbrooke, Québec, Canada	Président
Giorgio Sangiovanni Professeur, Institute for Theoretical Physics and Astrophysics, Würzburg, Allemagne	Rapporteur
Ulrich Schollwöck Professeur, LMU München, Allemagne	Rapporteur
Corinna Kollath Professeure, Physikalisches Institut, Universität Bonn, Allemagne	Examinatrice
Thierry Giamarchi Professeur, Department of Quantum Matter Physics, Ecole de Physique, University of Geneva, Suisse	Examinateur

Contents

1 Introduction

Materials with strong electronic correlations host among the most fascinating phenomena of modern condensed matter physics. They originate from a complex interplay between the Coulomb interaction, the kinetic motion of the electrons, the lattice structure and magnetic degrees of freedom. Different phases characterized by distinct symmetries and properties compete. Because they may have very similar (free) energies, small modifications of parameters, such as the electronic density, an external magnetic field or pressure can stabilize one or another phase or give birth to new states of matter. This often results in sophisticated phase diagrams with, for example, unusual spin- or charge-ordered regimes [1], Mott metal-to-insulator transitions [2], quantum critical behavior close to zero-temperature phase transitions [3] or high-temperature superconductivity [4]. An emblematic example of such phase diagrams in shown in Fig. 1. It features the different forms of matter that appear in the hole-doped copper oxides discovered in 1986 [5, 6]. Changes in the number of electronic carriers and temperature yield a number of peculiar phases and regimes with remarkable properties. On the one hand, investigating these phase diagrams raises very fundamental physics questions about the emergence of organized structures in systems involving a large number of interacting particles [7]. On the other hand, correlated materials can have useful properties and it is likely that unconventional features like high-temperature superconductivity or colossal magnetoresistance will find future technological applications. It is then no surprise that the discovery of high-temperature superconductors and other strongly correlated materials has triggered an immense amount of innovative scientific inquiry. Experimental techniques have been developed with ever more sensitive and precise probes on increasingly cleaner samples.

Despite all these advances, many central questions remain. For example, the nature of the pseudogap regime [8, 9] or the mechanisms behind the superconductivity in cuprates is still largely debated [10]. Even more generic features, such as the strange metallic behavior seen in many correlated materials [11], have escaped a generally accepted understanding. Indeed, studying the physics of a large number of interacting quantum entities, the quantum many-body problem, is a formidable theoretical challenge. To date, there is no generic framework that allows to embrace the full complexity of a realistic material, including all electronic and lattice degrees of freedom. There is therefore a crucial need to develop practical tools for calculating and predicting materials properties, as outlined by Dirac in 1929 [12]. A natural first step in this construction of efficient methods for the many-body problem is to start investigating simpler models that nevertheless capture the essence of interacting quantum particles, very much like the Ising model [13, 14] does in the context of classical statistical physics.

Hubbard model Probably the simplest model describing interacting fermions on a lattice is the single-band Hubbard model [15–18] given by the Hamiltonian

$$\mathcal{H} = \sum_{\boldsymbol{r},\boldsymbol{r}',\sigma} t_{\boldsymbol{r}\boldsymbol{r}'} c^\dagger_{\boldsymbol{r}\sigma} c_{\boldsymbol{r}'\sigma} + U \sum_{\boldsymbol{r}} n_{\boldsymbol{r}\uparrow} n_{\boldsymbol{r}\downarrow}, \tag{1}$$

where $t_{\boldsymbol{r}\boldsymbol{r}'}$ are hopping amplitudes between the sites $\boldsymbol{r}$, $\boldsymbol{r}'$ of a lattice, $c^\dagger_{\boldsymbol{r}\sigma}$ creates a fermion with spin σ at site $\boldsymbol{r}$, $n_{\boldsymbol{r}\sigma} = c^\dagger_{\boldsymbol{r}\sigma} c_{\boldsymbol{r}\sigma}$ and U is the Coulomb repulsion experienced by two fermions sitting on the same lattice site. The Hubbard model emphasizes the physics of electronic correlations and, in this simple form, does not include multiple orbitals, non-local interactions or lattice effects. Despite its simplicity, the Hubbard model displays a wide range of correlated electron behaviors ranging from metal-to-insulator transitions to superconductivity and magnetism [19, 20]. It is also believed to be a relevant effective low-energy model for cuprate superconductors [21]. More recently, experiments on cold atoms trapped in optical lattices have also been able to directly simulate the Hubbard model at intermediate temperatures [22–27].

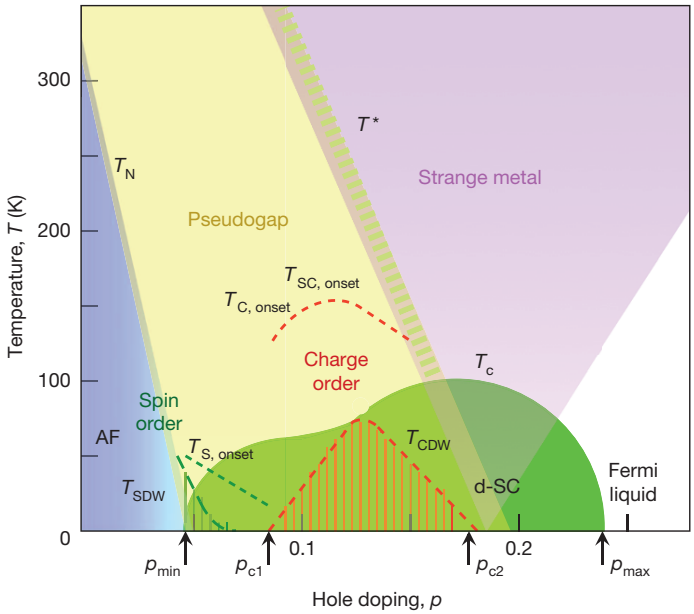

Figure 1: Typical phase diagram of hole-doped copper oxides. The blue and green regions correspond to antiferromagnetic order (AF) and d-wave superconducting order (d-SC) setting in at the Néel and superconducting transition temperatures T_N and T_c, respectively. The yellow and magenta regions indicate the pseudogap and strange metallic regimes, separated by a crossover at T^*. The red and green striped area show the presence of charge and incommensurate spin order below T_{CDW} and T_{SDW}, respectively. Taken from Ref. [6].

Except for special circumstances, such as the one-dimensional case [28, 29], there is no general analytical solution for the Hubbard model (1). In that respect, the development of sophisticated computational methods has been instrumental in making progress in our understanding of the model. As we will discuss below, all numerical approaches are based on some level of approximation. If this has originally led to possible disagreements between different methods, the situation is constantly improving and consensus is progressively reached for certain regimes of parameters of the model, notably thank to multi-method collaborations [30–34]. For example, it is now established that the ground state of the two-dimensional Hubbard model with only nearest-neighbor hoppings at intermediate to strong coupling and near optimal doping does not display superconductivity but rather a stripe ordered phase [32]. The existence of superconductivity in this model has been a central question in the field and more work is still needed to establish how the situation depends on the presence of e.g. a next-nearest-neighbor hopping. Another example where a consensus has been reached is the weak-coupling finite temperature regime of the half-filled two-dimensional Hubbard model (with no nearest-neighbor hopping) which is now largely understood (see Sec. 4 and Ref. [34]). There are however still many exciting regimes where a consensus is lacking, especially in trying to connect the ground-state properties to those found at finite temperature [35, 36]. This can to some extent be attributed to the existence of a dichotomy in the available algorithms for zero and finite temperature.

Ground-state methods A possible approach to characterize the physics of strongly correlated systems is to start from their ground-state properties and infer how they may be controlling their properties at finite temperature. Algorithms aiming at the zero-temperature limit are often wavefunction-based methods. They construct an approximation to the ground-state wavefunction which is used to compute physical observables. We briefly describe two prototypical examples of these algorithms:

- Auxiliary-field quantum Monte Carlo: This algorithm [37–39] starts from a trial wavefunction and projects it to the ground state by applying $e^{-\beta\mathcal{H}}$ for $\beta \to \infty$. The method works in imaginary time on finite lattices. The projection is done stochastically and can suffer from the fermionic sign problem [40]. The latter can be circumvented by a constrained-path approximation that involves a choice of a proper trial wavefunction.

- Density matrix renormalization group: It is a variational wavefunction algorithm [41, 42] that constructs the ground state by diagonalizing the Hamiltonian in a truncated subspace determined by the condition that the spatial extent of the entanglement between basis states should be minimized. The algorithm generally works on strip geometries and is controlled by the number of states that need to be kept in the basis in order to capture the entanglement of the wavefunction.

Finite temperature algorithms A different path to analyze the properties of interacting fermions is to take a top-to-bottom viewpoint, where one studies the physical observables at finite temperature and gradually reduces it to identify the onset of different regimes and possible instabilities on the way to the ground state. Most of the algorithms in this class of methods are stochastic. We again describe some typical examples here:

- Dynamical mean-field theory and extensions: The dynamical mean-field theory [43–45] has been a central tool in the study of correlated systems. It maps the original lattice problem on a self-consistent impurity model. It thus fully captures local correlations but neglects spatial correlations. Several cluster [46] or vertex-based [47] extensions allow for a systematic improvement over single-site dynamical mean-field theory by including spatial correlations. In all these methods, the computational complexity comes from solving a cluster of quantum impurities embedded in a bath, typically with continuous-time quantum Monte Carlo methods [48]. They generally suffer from a fermionic sign problem and are limited by the size of the impurity cluster.

- Determinantal quantum Monte Carlo: This algorithm is a controlled method for the simulation of correlated fermions on a finite lattice [49–53]. It is based on a transformation of the interacting problem into a free fermion system coupled with auxiliary fields. The field configurations are sampled stochastically to compute physical observables. It requires extrapolations with the system size and the Trotter discretization step.

- Diagrammatic Monte Carlo: First developed by Svistunov and Prokof'ev [54], this algorithm is based on the stochastic evaluation of the Feynman diagrams contributing to a given perturbation expansion. The method can work directly in the limit of infinite system size. It is limited by the statistical variance and the perturbation series for physical observables need to be resummed from the knowledge of a small number of perturbation orders. Recent improvements of this method are the topic of the following sections.

Limitations and complementarity The algorithms described above all face some limitation connected to the entanglement of the ground-state wavefunction, the choice of an appropriate guiding wavefunction, the fermionic sign problem or the restricted size or geometry of the system that they can consider. There is no universal method that can tackle all regimes of parameters of a quantum many-body problem and it is very important to take advantage of the complementary viewpoints that they offer. In that respect, attempting to establish a handshake between the results obtained from zero-temperature methods and finite-temperature approaches will certainly prove to be a very fruitful enterprise. There is therefore a great value in continuing to push forward the development of existing algorithms and in conceiving new ones.

Diagrammatic Monte Carlo and its recent developments In the following, we will discuss some recent developments and applications of one of the techniques introduced above: the diagrammatic Monte Carlo algorithm. It is a very versatile approach that has been applied to a variety of physical systems including, among others, the polaron problem [55–58], the electron gas [59–61] or the unitary gas [62]. It will not be our intention to cover all these applications and the presentation will be highly biased towards our own work with results obtained for different incarnations of the Hubbard model at *finite temperature and at equilibrium*. As we will discuss, one of the singular aspects and strength of the diagrammatic Monte Carlo approach is that it can treat very large systems avoiding the need to perform finite-size scaling. On the other hand, there are difficult regimes, especially those characterized by a long magnetic correlation length, where it is still difficult to obtain accurate results and more future developments are needed.

Organization of the following sections In Sec. 2, we introduce the general notion of a diagrammatic Monte Carlo method by taking the particular example of the interaction expansion continuous-time quantum Monte Carlo algorithm. This will set the stage to present the original version of the diagrammatic Monte Carlo method. There have been several important recent algorithmic improvements to the method that have contributed to broaden its scope of applicability. These developments are discussed in Sec. 3. The following three sections present applications of these algorithms to several versions of the Hubbard model. In Sec. 4, we discuss the physics of the half-filled Hubbard model in two dimensions which also includes results obtained from a large body of other many-body methods. We then turn to the physics of the antiferromagnetic phase of the three-dimensional Hubbard model at half-filling in Sec. 5. The third model that we have investigated is the doped two-dimensional Hubbard that we discuss in Sec. 6. In particular, we analyze the behavior of the pseudogap regime and how it is related to the onset of magnetic correlations. We also attempt to establish a connection between our finite-temperature results and ground-state results obtained by auxiliary-field quantum Monte Carlo. We finally conclude and discuss future perspectives in Sec. 7.

2 Diagrammatic Monte Carlo algorithms

There are several algorithms that are designated as diagrammatic Monte Carlo algorithms. What they all have in common is that they stochastically sample the contributions of a perturbation expansion. Different algorithms use expansions of different quantities of interest expanded in different coupling constants. Our main focus will be the algorithm originally introduced by N. Prokof'ev and B. Svistunov [55] and its subsequent developments and applications to the Hubbard model. To avoid confusion, we will denote the latter as DiagMC in the following. But before introducing the DiagMC, we will first examine another perturbation-based algorithm: the continuous-time interaction expansion quantum Monte Carlo (CT-INT) [63–66]. Historically, the CT-INT has been introduced after the DiagMC, but it is useful to review it in order to introduce the formalism and discuss similarities and differences with the DiagMC approach later on.

2.1 An example of a perturbation expansion algorithm: CT-INT

The CT-INT is now mainly used in the context of quantum impurity models, but it can equally be formulated for the Hubbard model (is it then sometimes referred to as determinant diagrammatic Monte Carlo – DDMC). The starting point is a separation of the Hamiltonian into a non-interacting part $\mathcal{H}_0$ and a perturbation part $\mathcal{H}_{\text{int}}$:

$$\mathcal{H} = \sum_{r,r',\sigma} t_{rr'} c^\dagger_{r\sigma} c_{r'\sigma} + U \sum_r n_{r\uparrow} n_{r\downarrow} = \mathcal{H}_0 + \mathcal{H}_{\text{int}}. \tag{2}$$

With this separation, it is natural to work in the interaction picture (operators will have a hat in this picture). The time evolution operator is given by

$$\hat{U}(\tau,\tau') = e^{\tau\mathcal{H}_0} \left[e^{-(\tau-\tau')\mathcal{H}}\right] e^{-\tau'\mathcal{H}_0}. \tag{3}$$

It satisfies the following differential equation

$$\partial_\tau \hat{U}(\tau,\tau') = e^{\tau\mathcal{H}_0} \left(\mathcal{H}_0 - \mathcal{H}\right) e^{-(\tau-\tau')\mathcal{H}} e^{-\tau'\mathcal{H}_0} = -\hat{H}_{\text{int}}(\tau)\hat{U}(\tau,\tau') \tag{4}$$

with the initial condition $\hat{U}(\tau,\tau) = \mathbb{1}$. By iteratively integrating the equation we find

$$\hat{U}(\tau,\tau') = \sum_{n=0}^{\infty} \frac{(-1)^n}{n!} \int_{\tau'}^{\tau} d\tau_1 \cdots \int_{\tau'}^{\tau} d\tau_n \, T_\tau \left[\hat{H}_{\text{int}}(\tau_1)\cdots\hat{H}_{\text{int}}(\tau_n)\right], \tag{5}$$

where we introduced the time-ordering operator T_τ. This expression will be useful to obtain perturbation series for quantities of interest.

2.1.1 Perturbation series for the partition function

The expression (5) for the time evolution operator allows us to find a perturbation expansion of the partition function Z in powers of the Coulomb interaction U, i.e.

$$Z = \text{Tr} e^{-\beta\mathcal{H}} = \sum_{n=0}^{\infty} z_n U^n, \tag{6}$$

where $\beta = 1/T$ is the inverse temperature. Indeed,

$$\begin{aligned}\frac{Z}{Z_0} &= \left\langle \hat{U}(\beta,0)\right\rangle_0 = \sum_{n=0}^{\infty}\frac{(-1)^n}{n!}\int_0^\beta d\tau_1\cdots\int_0^\beta d\tau_n\,\left\langle T_\tau\left[\hat{H}_{\text{int}}(\tau_1)\cdots\hat{H}_{\text{int}}(\tau_n)\right]\right\rangle_0 \\ &= \sum_{n=0}^{\infty}\frac{(-U)^n}{n!}\int_0^\beta d\tau_1\cdots\int_0^\beta d\tau_n \\ &\qquad \sum_{\boldsymbol{r}_1,\ldots,\boldsymbol{r}_n}\left\langle T_\tau\left[\hat{n}_{\boldsymbol{r}_1\uparrow}(\tau_1)\cdots\hat{n}_{\boldsymbol{r}_n\uparrow}(\tau_n)\right]\right\rangle_0\left\langle T_\tau\left[\hat{n}_{\boldsymbol{r}_1\downarrow}(\tau_1)\cdots\hat{n}_{\boldsymbol{r}_n\downarrow}(\tau_n)\right]\right\rangle_0,\end{aligned} \tag{7}$$

where $\langle\hat{A}\rangle_0$ is the average of the observable A in the non-interacting system and $Z_0 = \exp(-\beta\mathcal{H}_0)$. We can now use Wick's theorem to express these averages as simple determinants

$$Z = Z_0\sum_{n=0}^{\infty}\frac{(-U)^n}{n!}\int_0^\beta d\tau_1\cdots\int_0^\beta d\tau_n\sum_{\boldsymbol{r}_1,\ldots,\boldsymbol{r}_n}\det M_\uparrow^{(n)}\,\det M_\downarrow^{(n)}, \tag{8}$$

where the matrices have elements

$$M_\sigma^{(n)} = \begin{pmatrix} G_{0\sigma}(0,0^-) & G_{0\sigma}(\boldsymbol{r}_1-\boldsymbol{r}_2,\tau_1-\tau_2) & \ldots & G_{0\sigma}(\boldsymbol{r}_1-\boldsymbol{r}_n,\tau_1-\tau_n)\\ G_{0\sigma}(\boldsymbol{r}_2-\boldsymbol{r}_1,\tau_2-\tau_1) & G_{0\sigma}(0,0^-) & \ldots & G_{0\sigma}(\boldsymbol{r}_2-\boldsymbol{r}_n,\tau_2-\tau_n)\\ \vdots & \vdots & \ddots & \vdots\\ G_{0\sigma}(\boldsymbol{r}_n-\boldsymbol{r}_1,\tau_n-\tau_1) & G_{0\sigma}(\boldsymbol{r}_n-\boldsymbol{r}_2,\tau_n-\tau_2) & \ldots & G_{0\sigma}(0,0^-)\end{pmatrix}. \tag{9}$$

In these matrices, the non-interacting propagator $G_{0\sigma}$ is given in Fourier space by

$$G_{0\sigma}(\boldsymbol{k}, i\omega_n) = \frac{1}{i\omega_n+\mu-\epsilon_{\boldsymbol{k}}}, \tag{10}$$

where $\epsilon_{\boldsymbol{k}}$ is the non-interacting dispersion of the electrons. From the expressions above, we see that the partition function Z can be expressed as a perturbation series in U. Every coefficient in this series is an integral of a product of determinants over n imaginary times $\{\tau_1,\ldots,\tau_n\}$ and n site positions $\{\boldsymbol{r}_1,\ldots,\boldsymbol{r}_n\}$.

2.1.2 Ratio of perturbation series for the Green function

A very similar derivation can be used to obtain the perturbation series for the interacting Green function

$$G_\sigma(\boldsymbol{r}-\boldsymbol{r}',\tau-\tau') = -\frac{1}{Z}\text{Tr}e^{-\beta\mathcal{H}}T_\tau c_{\boldsymbol{r}\sigma}(\tau)c^\dagger_{\boldsymbol{r}'\sigma}(\tau') \tag{11}$$

Using the time evolution operator, it can be written as

$$G_\sigma(\boldsymbol{r}-\boldsymbol{r}',\tau-\tau') = -\frac{1}{Z}\left\langle T_\tau\left(\hat{U}(\beta,0)\hat{c}_\sigma(\tau)\hat{c}^\dagger_\sigma(\tau')\right)\right\rangle_0 \tag{12}$$

Following the same steps as for the partition function, we end up with

$$\begin{aligned}G_\sigma(\boldsymbol{r}-\boldsymbol{r}',\tau-\tau') = \frac{Z_0}{Z}\sum_{n=0}^{\infty}\frac{(-U)^n}{n!}\int_0^\beta d\tau_1\cdots\int_0^\beta d\tau_n \\ \sum_{\boldsymbol{r}_1,\ldots,\boldsymbol{r}_n}\left\langle(-1)\,T_\tau\left[\hat{n}_{\boldsymbol{r}_1\uparrow}\hat{n}_{\boldsymbol{r}_1\downarrow}(\tau_1)\cdots\hat{n}_{\boldsymbol{r}_n\uparrow}\hat{n}_{\boldsymbol{r}_n\downarrow}(\tau_n)\hat{c}_{\boldsymbol{r}\sigma}(\tau)\hat{c}^\dagger_{\boldsymbol{r}'\sigma}(\tau')\right]\right\rangle_0\end{aligned} \tag{13}$$

We can again use Wick's theorem and express the non-interacting averages in terms of determinants. The only difference is that the matrix corresponding to the spin σ will have one more row and column corresponding to the $\hat{c}_\sigma(\tau)\hat{c}^\dagger_\sigma(\tau')$ terms

$$G_\sigma(\boldsymbol{r}-\boldsymbol{r}',\tau-\tau') = \frac{Z_0}{Z}\sum_{n=0}^{\infty}\frac{(-U)^n}{n!}\int_0^\beta d\tau_1\cdots\int_0^\beta d\tau_n\sum_{\boldsymbol{r}_1,\ldots,\boldsymbol{r}_n}\det\widetilde{M}_\sigma^{(n)}\,\det M_{\bar{\sigma}}^{(n)} \tag{14}$$

where $M_{\bar{\sigma}}^{(n)}$ is the same as above and $\widetilde{M}_{\sigma}^{(n)}$ has elements

$$\widetilde{M}_{\sigma}^{(n)} = \begin{pmatrix} G_{0\sigma}(0,0^-) & \dots & G_{0\sigma}(\boldsymbol{r}_1-\boldsymbol{r}_n,\tau_1-\tau_n) & G_{0\sigma}(\boldsymbol{r}_1-\boldsymbol{r}',\tau_1-\tau') \\ G_{0\sigma}(\boldsymbol{r}_2-\boldsymbol{r}_1,\tau_2-\tau_1) & \dots & G_{0\sigma}(\boldsymbol{r}_2-\boldsymbol{r}_n,\tau_2-\tau_n) & G_{0\sigma}(\boldsymbol{r}_2-\boldsymbol{r}',\tau_2-\tau') \\ \vdots & \ddots & \vdots & \vdots \\ G_{0\sigma}(\boldsymbol{r}_n-\boldsymbol{r}_1,\tau_n-\tau_1) & \dots & G_{0\sigma}(0,0^-) & G_{0\sigma}(\boldsymbol{r}_n-\boldsymbol{r}',\tau_n-\tau') \\ G_{0\sigma}(\boldsymbol{r}-\boldsymbol{r}_1,\tau-\tau_1) & \dots & G_{0\sigma}(\boldsymbol{r}-\boldsymbol{r}_n,\tau-\tau_n) & G_{0\sigma}(\boldsymbol{r}-\boldsymbol{r}',\tau-\tau') \end{pmatrix} \tag{15}$$

We have now found a perturbation series for the partition function and an expression for the Green function that involves a ratio of two series. Indeed, in (13) the partition function Z in the denominator is itself a series in U. Note that similar calculations can be carried out for other observables such as the double occupancy, etc.

2.1.3 Monte Carlo sampling

The final expression for the Green function has the form

$$G_\sigma(\boldsymbol{r}-\boldsymbol{r}',\tau-\tau') = \frac{\sum_{n=0}^{\infty}\frac{(-U)^n}{n!}\int_0^\beta d\tau_1\cdots\int_0^\beta d\tau_n\sum_{\boldsymbol{r}_1,\dots,\boldsymbol{r}_n}\det\widetilde{M}_\sigma^{(n)}\,\det M_{\bar{\sigma}}^{(n)}}{\sum_{n=0}^{\infty}\frac{(-U)^n}{n!}\int_0^\beta d\tau_1\cdots\int_0^\beta d\tau_n\sum_{\boldsymbol{r}_1,\dots,\boldsymbol{r}_n}\det M_\uparrow^{(n)}\,\det M_\downarrow^{(n)}}. \tag{16}$$

Carrying out the integrals over imaginary times and sums over space positions quickly becomes prohibitive with standard integration tools. A natural approach is to sample them stochastically using a Metropolis-Hastings algorithm. In that context, a Monte Carlo configuration would be associated with a given choice of the perturbation order n, a set of imaginary times $\{\tau_1,\dots,\tau_n\}$ and a set of positions $\{\boldsymbol{r}_1,\dots,\boldsymbol{r}_n\}$. We can denote such a configuration with $\mathcal{C}=\{n,\boldsymbol{r}_1,\tau_1,\dots,\boldsymbol{r}_n,\tau_n\}$. The expression for the Green function then becomes

$$G_\sigma(\boldsymbol{r}-\boldsymbol{r}',\tau-\tau') = \frac{\sum_{\mathcal{C}}\frac{(-U)^n}{n!}\det\widetilde{M}_\sigma[\mathcal{C}]\,\det M_{\bar{\sigma}}[\mathcal{C}]}{\sum_{\mathcal{C}}\frac{(-U)^n}{n!}\det M_\uparrow[\mathcal{C}]\,\det M_\downarrow[\mathcal{C}]}. \tag{17}$$

A natural choice for the Monte Carlo weight $\rho(\mathcal{C})$ of a configuration $\mathcal{C}$ is to use the absolute value of the contribution $w(\mathcal{C})$ of that configuration to the partition function

$$\rho(\mathcal{C}) = |w(\mathcal{C})| = \left|\frac{(-U)^n}{n!}\det M_\uparrow[\mathcal{C}]\,\det M_\downarrow[\mathcal{C}]\right| \tag{18}$$

The Monte Carlo estimate of the Green function is then

$$G_\sigma(\boldsymbol{r}-\boldsymbol{r}',\tau-\tau') = \frac{\sum_{\mathcal{C}}^{\mathrm{MC}}\mathrm{sign}(w(\mathcal{C}))\det\widetilde{M}_\sigma[\mathcal{C}]/\det M_\sigma[\mathcal{C}]}{\sum_{\mathcal{C}}^{\mathrm{MC}}\mathrm{sign}(w(\mathcal{C}))}, \tag{19}$$

where $\sum_{\mathcal{C}}^{\mathrm{MC}}$ is a sum over the configurations generated during the Markov process with relative probabilities given by $\rho(\mathcal{C})$. There is freedom about how to propose new configurations in the Markov chain. A simple way to generate ergodic configurations is to have two Monte Carlo "moves": an insertion of an additional vertex at a random imaginary time and a random position and a removal of a randomly chosen vertex in $\mathcal{C}$. The first move increases the current perturbation order $n\to n+1$, while the second move decreases the perturbation order $n\to n-1$. As a side remark, one can efficiently compute the ratio $\det\widetilde{M}_\sigma[\mathcal{C}]/\det M_\sigma[\mathcal{C}]$ by keeping a copy of the inverse matrix $M_\sigma^{-1}[\mathcal{C}]$ and updating it during the Monte Carlo evolution using the Sherman–Morrison formula. The numerical cost for the insertion or removal of a vertex is then $\mathcal{O}(n^2)$.

2.1.4 The fermionic sign problem and the α-trick

In the formulation above, the CT-INT algorithm will suffer from a very strong fermionic sign problem. Its origin comes from the sign changes of the contribution $w(\mathcal{C})$ in the denominator in (19). Indeed, when there is no spin imbalance, both determinants entering $w(\mathcal{C})$ in (18) are the same and their product is positive. A sign alternation then comes from the $(-U)^n$ and subsequent orders have contributions of opposite sign. This leads to an increased variance that eventually makes it impossible to obtain reliable estimates of the physical observables.

A way to improve the sign problem is to change the determinants so that their product will have a sign compensating the $(-1)^n$. This can be partially achieved with the so-called α-trick: rewrite the interaction term in the Hamiltonian as

$$U n_{\boldsymbol{r}\uparrow} n_{\boldsymbol{r}\downarrow} \quad \rightarrow \quad U(n_{\boldsymbol{r}\uparrow} - \alpha_\downarrow)(n_{\boldsymbol{r}\downarrow} - \alpha_\uparrow) + U \sum_\sigma n_{\boldsymbol{r}\sigma}\alpha_\sigma + \text{const} \tag{20}$$

and write the expansion in powers of $U(n_{\boldsymbol{r}\uparrow} - \alpha_\downarrow)(n_{\boldsymbol{r}\downarrow} - \alpha_\uparrow)$. To compensate for this change, the second term $U\sum_\sigma n_{r\sigma}\alpha_\sigma$ must be included as a constant energy shift in the non-interacting part $\mathcal{H}_0$. This artificial introduction of $\alpha_\uparrow$ and $\alpha_\downarrow$ has no consequence on the final result, but it leads to two practical changes. The first is that the non-interacting Green function is now given by

$$G_{0\sigma}(\boldsymbol{k}, i\omega_n) = \frac{1}{i\omega_n + \mu - \epsilon_{\boldsymbol{k}} - U\alpha_\sigma}, \tag{21}$$

which creates a spin imbalance for the non-interacting electrons. The second change brought by the α_σ is that the expansion in powers of U will involve different interaction terms and the matrices now include extra α_σ terms on the diagonal

$$M_\sigma^{(n)} \rightarrow \begin{pmatrix} G_{0\sigma}(0,0^-) - \alpha_{\bar\sigma} & G_{0\sigma}(\boldsymbol{r}_1 - \boldsymbol{r}_2, \tau_1 - \tau_2) & \dots & G_{0\sigma}(\boldsymbol{r}_1 - \boldsymbol{r}_n, \tau_1 - \tau_n) \\ G_{0\sigma}(\boldsymbol{r}_2 - \boldsymbol{r}_1, \tau_2 - \tau_1) & G_{0\sigma}(0,0^-) - \alpha_{\bar\sigma} & \dots & G_{0\sigma}(\boldsymbol{r}_2 - \boldsymbol{r}_n, \tau_2 - \tau_n) \\ \vdots & \vdots & \ddots & \vdots \\ G_{0\sigma}(\boldsymbol{r}_n - \boldsymbol{r}_1, \tau_n - \tau_1) & G_{0\sigma}(\boldsymbol{r}_n - \boldsymbol{r}_2, \tau_n - \tau_2) & \dots & G_{0\sigma}(0,0^-) - \alpha_{\bar\sigma} \end{pmatrix}. \tag{22}$$

Let us consider the contribution to the partition function at order 1. The product of the determinants in this case is

$$\left\langle T_\tau(\hat{n}_{\boldsymbol{r}_1\uparrow} - \alpha_\downarrow)(\tau_1)\right\rangle_0 \left\langle T_\tau(\hat{n}_{\boldsymbol{r}_1\downarrow} - \alpha_\uparrow)(\tau_1)\right\rangle_0 = (\langle n_{\boldsymbol{r}_1\uparrow}\rangle_0 - \alpha_\downarrow)(\langle n_{\boldsymbol{r}_1\downarrow}\rangle_0 - \alpha_\uparrow) \tag{23}$$

If we for example suppose that $\langle n_{\boldsymbol{r}_1\sigma}\rangle_0 \simeq 1/2$ as would be the case for a system close to half-filling, then one could choose

$$\alpha_\sigma = \begin{cases} \frac{1}{2} + \delta & \sigma = \uparrow \\ \frac{1}{2} - \delta & \sigma = \downarrow \end{cases} \tag{24}$$

For some value of δ, we can expect that the two terms $(\langle n_\uparrow\rangle_0 - \alpha_\downarrow)$ and $(\langle n_\downarrow\rangle_0 - \alpha_\uparrow)$ will have different signs so that their product is negative. This would compensate for the $(-U)$ prefactor and make the contribution positive. With similar arguments, one can motivate that at higher orders, such a choice for α_σ may lead to products of determinants that have a sign $(-1)^n$ compensating the $(-U)^n$. In the generic case, the sign problem cannot be completely removed, but tuning the δ parameter can lead to great improvements.

2.1.5 Behavior of the sign problem and limitations of the algorithm

The complexity of the CT-INT algorithm is of order $\mathcal{O}(n^2)$ at every Monte Carlo step. It is clear that the average perturbation order visited during the simulation will control the computational

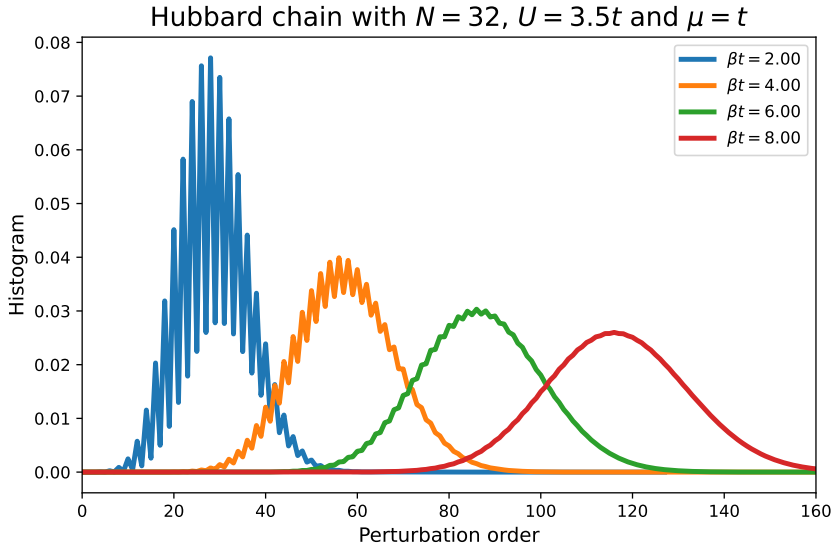

Figure 2: Histograms of the absolute contributions from different perturbation orders to the partition function of the one-dimensional Hubbard chain with $N = 32$ sites, $U = 3.5t$ and $\mu = t$. The histograms correspond to four different temperatures and it is seen that the average perturbation order increases linearly with inverse temperature β.

---

speed of a step in the calculation. It can be shown that the average perturbation order behaves as $\sim U\beta N$, where N is the number of sites considered in the model. An example of the distribution of perturbation orders contributing to the partition function is shown in Fig. 2 for a one-dimensional periodic Hubbard chain

$$\mathcal{H}_{\text{chain}} = -t \sum_{i=1}^{N} \sum_{\sigma} c_{i\sigma}^{\dagger} c_{i+1\sigma} - \mu \sum_{i=1}^{N} \sum_{\sigma} n_{i\sigma} + U \sum_{i=1}^{N} n_{i\uparrow} n_{i\downarrow}, \tag{25}$$

where N is the number of sites in the chain, μ is the chemical potential, t the nearest-neighbor hopping and U the onsite Coulomb repulsion. The polynomial increase of the average perturbation order with system size, inverse temperature and interaction strength certainly makes the algorithm slower, but it is not the major bottleneck of the algorithm.

The real limitation comes from the fermionic sign problem that generically appears. A good quantifier of the sign problem is the average sign in the denominator of (19)

$$s = \langle \text{sign}(w(\mathcal{C})) \rangle \,. \tag{26}$$

There are special cases, such as half-filling, when the sign problem is absent and $s = 1$. But for a doped lattice model, the increase of the average perturbation order is typically accompanied by an exponential reduction of the average sign with decreasing temperature or increasing system size. This is shown in Fig. 3 where we display both the average sign and the average perturbation order for a simulation of the one-dimensional Hubbard chain (25). The average perturbation order increases linearly with inverse temperature and with the number of sites N. When the sampled perturbation order is larger, the sign alternation becomes more dramatic as the imaginary times and positions of the internal vertices are changed. The resulting average sign is suppressed exponentially and the corresponding increase in variance makes it impossible to obtain accurate results at low temperature or larger coupling when the system is large. The impossibility to reach large system sizes with the CT-INT motivates the need to design other algorithms that allow for the simulation of large systems.

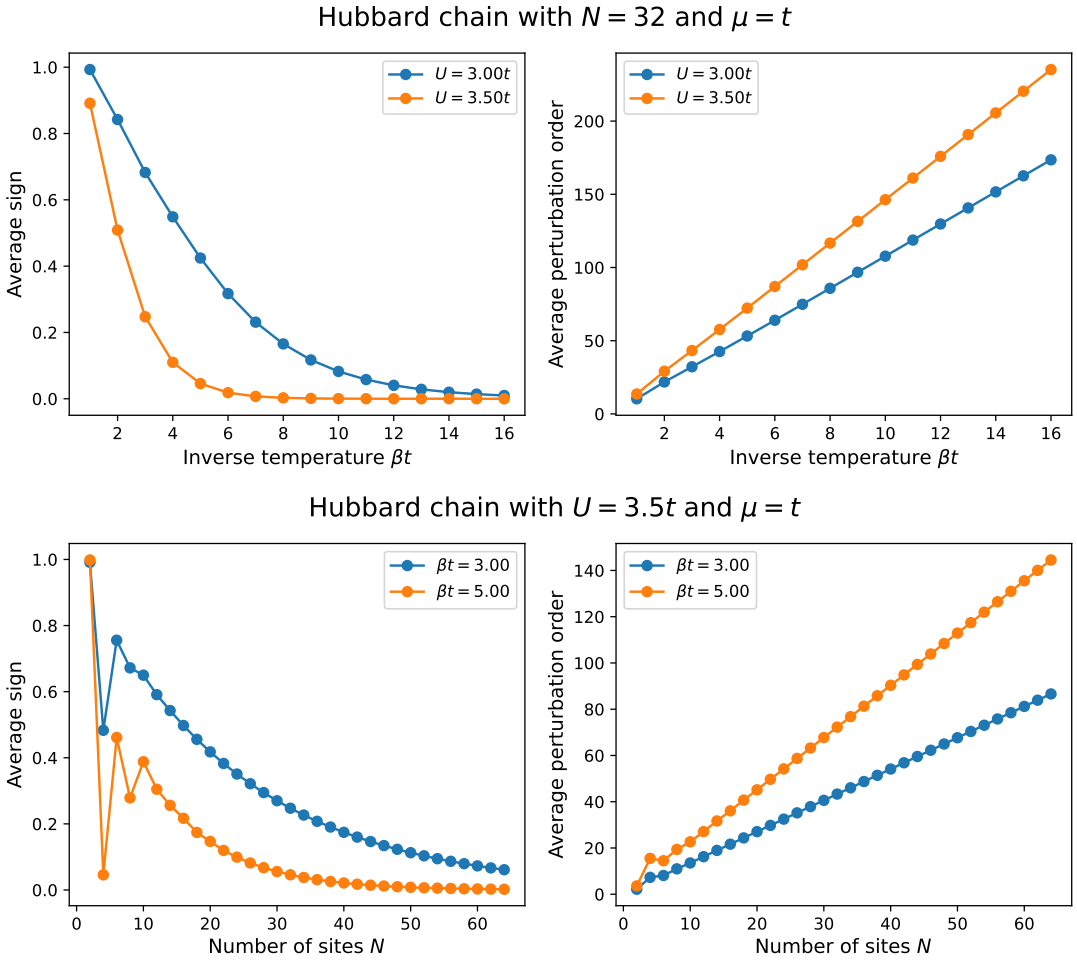

Figure 3: Behavior of the average sign (left panels) and average perturbation order (right panels) in the one-dimensional Hubbard chain. The upper panels display their behavior as a function of the inverse temperature $\beta = 1/T$ for two values of the interaction. The lower panels document the behavior as a function of the system size for two different temperatures. The average sign decreases exponentially with inverse temperature or number of sites.

2.1.6 Some remarks

This introduction to the CT-INT algorithm will be useful to discuss some of the properties of the DiagMC approach. Let us conclude this section by making some observations about the CT-INT algorithm:

- The algorithm is based on the stochastic sampling of a perturbation series, but it is not perturbative and limited to small values of the coupling U. Indeed, the algorithm is numerically exact and when the sign problem can be controlled, it can reach the strong coupling regime. In practice, all relevant perturbation orders are sampled and there is no artificial truncation that needs to be performed.
- Seen as complex functions of U, both the partition function and the numerator in the Green function (16) are *entire* functions. As a result, the corresponding series have infinite convergence radius. For any finite size system and any finite temperature, the coefficients eventually decay exponentially at large perturbation orders and their contribution becomes negligible. The perturbation series is therefore well-controlled mathematically. The limitation comes from the difficulty to accurately sample these coefficients because of the sign problem.
- The CT-INT belongs to the family of diagrammatic Monte Carlo methods, but diagrams are never used in practice. There is a diagrammatic interpretation of the determinants that can be seen as a sum of all Feynman diagrams that can be placed on the set of interaction vertices. But it is always their sum that is sampled, they are never sampled individually.
- There are other continuous-time quantum Monte Carlo algorithms, such as the CT-HYB [67, 68] or the CT-AUX [69] that are mainly targeted at solving quantum impurity models.

2.2 The original DiagMC algorithm

We now turn our discussion to the DiagMC algorithm. The algorithm has been introduced by N. Prokof'ev and B. Svistunov [55] for the polaron problem, but its formulation is very general. The idea of the algorithm is to write a single perturbation series directly for the physical observable of interest and sample its contributions stochastically. It may seem that this is precisely what we have described with the CT-INT algorithm above, but there is an important difference. In the CT-INT algorithm, the expression for the Green function (16) is a *ratio* of two perturbation series in U. The algorithm samples both the numerator and the denominator and then takes the ratio at the very end of the calculation. In the DiagMC algorithm, the Green function is not expressed as a ratio but as a single series

$$G_\sigma(\boldsymbol{r}-\boldsymbol{r}',\tau-\tau') = \sum_{n=0}^{\infty} g_n^\sigma U^n. \tag{27}$$

The coefficients of this series have a clear diagrammatic interpretation: every coefficient g_n^σ is given by

$$g_n^\sigma = \int_0^\beta d\tau_1 \cdots \int_0^\beta d\tau_n \sum_{\boldsymbol{r}_1,\ldots,\boldsymbol{r}_n} F^\sigma(\boldsymbol{r},\tau,\boldsymbol{r}',\tau';\boldsymbol{r}_1,\tau_1,\ldots,\boldsymbol{r}_n,\tau_n), \tag{28}$$

where the function $F^\sigma(\boldsymbol{r},\tau,\boldsymbol{r}',\tau';\boldsymbol{r}_1,\tau_1,\ldots,\boldsymbol{r}_n,\tau_n)$ is the sum of all *connected* diagrams with external vertices $(\boldsymbol{r},\tau)$ and $(\boldsymbol{r}',\tau')$ and internal vertices $\{(\boldsymbol{r}_1,\tau_1),\ldots,(\boldsymbol{r}_n,\tau_n)\}$. The elimination of disconnected diagrams comes from the linked cluster theorem. If one starts from the expression (13) both numerator and denominator have a diagrammatic interpretation: the product of the determinants can be seen as the sum of all possible diagrams at order n, both connected and

disconnected. But once the ratio is taken, all the disconnected diagrams simplify and one is left with only connected diagrams. This is the usual derivation of the Feynman diagrams for the Green function which is eventually written as

$$G_\sigma(\boldsymbol{r}-\boldsymbol{r}',\tau-\tau') = \sum_{n=0}^{\infty} \int_0^\beta d\tau_1 \cdots \int_0^\beta d\tau_n \sum_{\boldsymbol{r}_1,\ldots,\boldsymbol{r}_n} \sum_{k=1}^{M_n} D_k^\sigma(\boldsymbol{r},\tau,\boldsymbol{r}',\tau';\tau_1,\boldsymbol{r}_1,\ldots,\tau_n,\boldsymbol{r}_n), \tag{29}$$

where M_n is the number of different topologies of connected diagrams at order n and the contribution of the k^{th} connected diagram is $D_k^\sigma(\boldsymbol{r},\tau,\boldsymbol{r}',\tau';\tau_1,\boldsymbol{r}_1,\ldots,\tau_n,\boldsymbol{r}_n)$.

2.2.1 Monte Carlo sampling

Again, the imaginary-time integrals and the sums over spatial positions cannot be computed explicitly and a Monte Carlo algorithm is used to sample them. In the original DiagMC, the sum over the different diagram topologies is also done stochastically. A Monte Carlo configuration is then characterized by the set $\mathcal{C} = \{n, k, \boldsymbol{r}_1, \tau_1, \ldots, \boldsymbol{r}_n, \tau_n\}$ and the corresponding Monte Carlo probability is the absolute value of the contribution of a diagram

$$\rho(\mathcal{C}) = |w(\mathcal{C})| = \left| D_k^\sigma(\boldsymbol{r},\tau,\boldsymbol{r}',\tau';\tau_1,\boldsymbol{r}_1,\ldots,\tau_n,\boldsymbol{r}_n) \right|. \tag{30}$$

A given coefficient g_n^σ is then simply

$$g_n^\sigma = \mathcal{K} \sum_{\mathcal{C}}^{\text{MC}} \text{sign}(w(\mathcal{C})), \tag{31}$$

where the sum is over the configurations (here taken at fixed perturbation order n) generated by the Markov chain. Note that a Metropolis-Hastings algorithm will only produce configurations that have well-defined *relative* Monte Carlo probabilities, but it is not able to provide a normalized distribution. When the physical observable is obtained from a ratio, which is usually the case in statistical physics or in the CT-INT algorithm, this missing normalization cancels out in the ratio. But in DiagMC, there is no such ratio, and the Monte Carlo sum needs to be normalized by a constant $\mathcal{K}$. There are different strategies to obtain a normalization. For example, one can compute a known value from the sampled configurations and use it to normalize the result. Another possibility is to compute two subsequent orders at the same time (with moves that add or remove an interaction vertex) starting from order 0, which is known analytically, and use the lowest order to normalize the next order. Other more sophisticated approaches have also been proposed to efficiently compute and normalize all orders at the same time [70].

The Monte Carlo moves start from a given topology and generate new configurations, either by changing the values of the imaginary-time and space positions of the vertices, or by creating new topologies. Actually, in the original formulation of the DiagMC, the diagrams were constructed with vertices carrying an imaginary time and propagators expressed in reciprocal space. Special care had to be taken in the sampling of the diagrams in order to satisfy the momentum conservation. This could be achieved with a worm algorithm that was switching between a physical space where momentum conservation was ensured and a non-physical space where momentum conservation was not imposed [71]. In later implementations of the DiagMC, such as in our work Ref. [72], the diagrams were expressed in real space. This had both the advantage of making the Monte Carlo moves simpler to implement and also made the sampling more efficient because propagators have a fast decay as a function of spatial distance resulting in fairly localized diagrams. Note that the computational cost for a single Monte Carlo move is of order $\mathcal{O}(1)$ in the DiagMC.

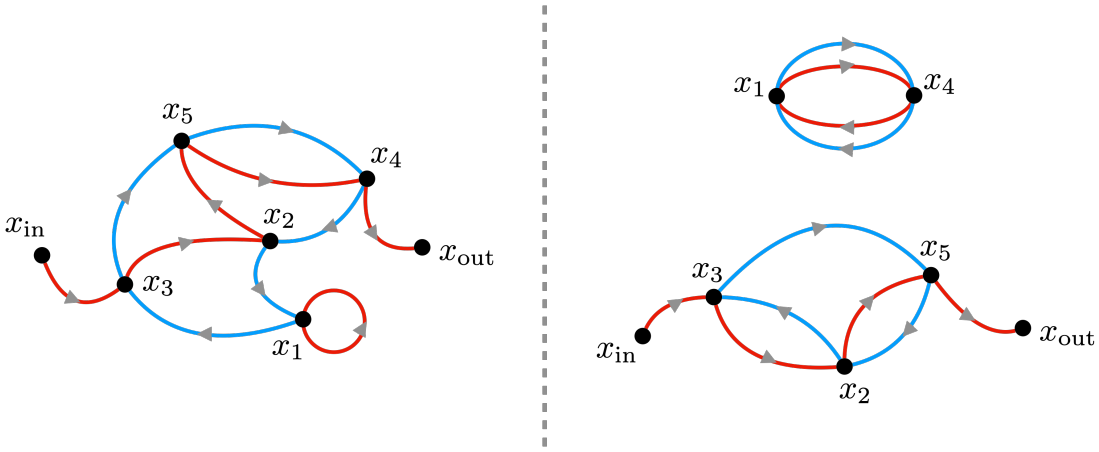

Figure 4: Thermodynamic behavior of connected and disconnected diagrams. Left panel: A connected diagram at order 5. Because propagators decay quickly with the distance, the spatial integral over internal vertices has mainly contributions from diagrams that remain close to x_{in} and x_{out}. As a result, the integral is not dramatically changing when the system size increases. Right panel: A disconnected diagrams at order 5. The disconnected piece involving x_1 and x_4 gives the same contribution to the diagram, no matter how far it is from x_{in} and x_{out}. The spatial integral over the internal vertices x_1 and x_4 will yield a contribution proportional to the system size. For the diagram that only contains disconnected pairs of fermionic loops (tadpoles), the corresponding contribution to the coefficient scales like $(\beta U N)^n$ at order n and strongly increases the average perturbation order.

2.2.2 Thermodynamic limit

Probably the biggest advantage of the DiagMC algorithm is the possibility to investigate very large systems. Unlike other algorithms, such as the CT-INT, the general structure of the contributions g_n^σ does not dramatically change with the system size. Different system sizes induce changes in the free propagators, but those are quite small when the system size is large enough. The system size also enters in the sums over spatial positions. But because the propagators decay quickly with the distance, the diagrams that have a non-negligible contribution are quite localized in space. As a result, only a restricted part of the spatial sums is relevant and it is not scaling with the system size. This property is intimately related to the fact that the diagrams are connected so that all vertices are bound together by the propagators (see Fig. 4).

In contrast, in the CT-INT algorithm, the determinants in the numerator and denominator can be seen as a sum of all possible diagrams, including disconnected ones. In this case, it is clear that diagrams consisting of several pieces can have a large weight even when the pieces are far apart, as shown in Fig. 4. Increasing the system size then directly leads to a larger coefficient growing like N^n at order n (N is the number of sites) and eventually pushes the average perturbation order to larger values.

2.2.3 Nature of the fermionic sign problem

The limitations of the DiagMC come from the difficulty to compute many series coefficients g_n^σ. The sign of the contributions $D_k^\sigma(\boldsymbol{r}, \tau, \boldsymbol{r}', \tau'; \tau_1, \boldsymbol{r}_1, \ldots, \tau_n, \boldsymbol{r}_n)$ changes for different value of the imaginary times and spatial positions. And even for fixed times and positions, different diagram topologies have different signs. Supposing that the perturbation series has a non-zero convergence radius R, the coefficients g_n^σ are expected to decrease as $1/R^n$. This means that at large orders,

the Monte Carlo sampling has to yield a small coefficient, while the number of diagrams increases factorially with absolute values of the contributions from single diagrams remaining of the same order of magnitude. This is how the fermionic sign problem [40] manifests itself in the DiagMC. Having an alternation of signs between different topologies is actually needed: if all diagrams had the same sign, the coefficients would increase factorially with the perturbation order and the series would never converge. In practice, however, this alternation yields a large statistical variance and typically not more than 6 or 7 perturbations orders can be computed with enough accuracy. A lot of the recent efforts aim at improving this sign problem, as discussed in Sec. 3.

2.2.4 Resummation of the series

In the DiagMC, it is directly the series for the physical observable that is computed. This series is less sensitive to the system size and can in principle be computed for very large lattices. However, unlike the partition function or the numerator of (16), the Green function seen as a function of the coupling U is not an entire function. The corresponding series will in general have a finite convergence radius. This introduces the new difficulty of resumming the series at the physical value of U. Various series acceleration or analytical continuation schemes are therefore typically needed in order to obtain the value of the physical observable. With only 6 or 7 perturbation orders, this can become very challenging and often limits the range of applicability of the DiagMC to weak-to-intermediate values of the coupling constant U.

2.3 Determinant-based versus diagram-based approaches

We have presented two prototypical diagrammatic Monte Carlo algorithms that share some similarities but also have some very distinctive differences. The CT-INT algorithm is based on a perturbation expansion of the partition function. It computes physical observables, such as the Green function, as a ratio $(ZG)/Z$ where both the numerator and the denominator are computed during the Monte Carlo. At every step a product of determinants is evaluated. From a diagrammatic perspective, this is a sum of a factorial number of connected and disconnected diagrams and it is obtained in a polynomial effort. If these diagrams were sampled individually, it would lead to a dramatic sign problem and only a few of perturbation orders could be computed. The strength of the determinant is that the sum of all diagrams has a much better behaving sign and very large perturbation orders (several hundreds) can be reached. On the other hand, the fact that the determinants contain disconnected diagrams leads to a rapid increase of the average perturbation order with the system size and an increasingly bad sign problem. As a result, it is difficult to address large systems with such determinant-based methods.

The DiagMC samples the contribution to the actual perturbation series of the physical quantity (not a ratio). For the Green function, those contributions are a set of connected diagrams that are sampled individually. The fact that diagrams are connected makes them more local in space and not as sensitive to the system size that can be taken very large. The sampling of individual diagrams comes with a strong sign problem and only a very limited number of coefficients can be evaluated. This makes the resummation of the series very difficult and the strong coupling regime is often out of reach. A natural way to improve the sign problem would be to explicitly sum all topologies at every Monte Carlo step, but this would come with a factorial computational cost that prohibits reaching large perturbation orders.

Understanding the strengths and limitations of these approaches has been a very important ingredient in the recent developments that took inspiration from both determinant- and diagram-based approaches and eventually lead to great algorithmic improvements. This will be the topic of the next section.

3 Recent algorithmic developments of the DiagMC

The DiagMC algorithm has not seen major improvements between 1998 and 2017. There have been some effort at improving the Monte Carlo sampling and reducing the fermionic sign problem, but the typical perturbation orders that were reachable for the Hubbard model remained quite limited, around 6 or 7. An important development that triggered renewed interest in the diagrammatic approach came in 2017, with the introduction of the connected determinant algorithm (CDet) [73]. From the discussion above, it seems clear that explicitly summing all connected diagrams at a given Monte Carlo step would yield a much better behavior of the sign. But a naive summation would require to add up a factorial number of terms. The idea behind the CDet algorithm is to use a recursive formula involving determinants in order to sum all the connected diagrams with a computational effort that is only exponential. This exponential cost is not as powerful as the polynomial complexity of computing the sum of all diagrams (both connected and disconnected) with a single determinant, but it nevertheless turned out to be a very important advance that made it possible to compute about twice as many perturbation orders as compared to the original DiagMC algorithm. It was soon generalized to compute one-particle irreducible quantities. With more available coefficients, a lot of the effort after that was to find ways to resum the series or formulate modified series with better convergence properties. We will summarize some of these developments here.

3.1 The CDet algorithm

Let us imagine we have a set of n interaction vertices characterized by n imaginary times and n spatial positions. We will denote this set by $V = \{x_1, \dots, x_n\}$ where $x_i = (\boldsymbol{r}_i, \tau_i)$ is a combined index for time and position. This set of internal vertices V will have a certain contribution to the coefficient g_n^σ in the perturbation series of the Green function $G_\sigma(x_{\text{out}}, x_{\text{in}})$. We will write this contribution with $\mathcal{G}_V^\sigma(x_{\text{out}}, x_{\text{in}})$ so that

$$g_n^\sigma = \frac{(-U)^n}{n!} \sum_V \mathcal{G}_V^\sigma(x_{\text{out}}, x_{\text{in}}). \tag{32}$$

From a diagrammatic point of view, $\mathcal{G}_V^\sigma(x_{\text{out}}, x_{\text{in}})$ is given by the sum of all connected diagrams starting at x_{in} and ending at x_{out} with propagators connecting the internal vertices in V. The idea of the CDet algorithm is to start from the sum of all connected and disconnected diagrams which can be expressed as the product of determinants

$$\mathcal{D}_V^\sigma(x_{\text{out}}, x_{\text{in}}) = \det M_V^\sigma(x_{\text{out}}, x_{\text{in}}) \det M_V^{\bar{\sigma}}(\varnothing), \tag{33}$$

where we have introduced the matrices

$$M_V^\sigma(x_{\text{out}}, x_{\text{in}}) = \begin{pmatrix} G_{0\sigma}(x_1, x_1) & \dots & G_{0\sigma}(x_1, x_n) & G_{0\sigma}(x_1, x_{\text{in}}) \\ \vdots & \ddots & \vdots & \vdots \\ G_{0\sigma}(x_n, x_1) & \dots & G_{0\sigma}(x_n, x_n) & G_{0\sigma}(x_n, x_{\text{in}}) \\ G_{0\sigma}(x_{\text{out}}, x_1) & \dots & G_{0\sigma}(x_{\text{out}}, x_n) & G_{0\sigma}(x_{\text{out}}, x_{\text{in}}) \end{pmatrix} \tag{34}$$

$$M_V^{\bar{\sigma}}(\varnothing) = \begin{pmatrix} G_{0\bar{\sigma}}(x_1, x_1) & \dots & G_{0\bar{\sigma}}(x_1, x_n) \\ \vdots & \ddots & \vdots \\ G_{0\bar{\sigma}}(x_n, x_1) & \dots & G_{0\bar{\sigma}}(x_n, x_n) \end{pmatrix}.$$

Then, the disconnected part is removed recursively. Any disconnected diagram in $\mathcal{D}_V^\sigma(x_{\text{out}}, x_{\text{in}})$ is made of two parts: a connected part involving x_{in}, x_{out} and some subset $S \subsetneq V$ of internal vertices

and a part that can be either connected or disconnected and involves the remaining vertices $V\backslash S$, see Fig. 5. For a given S, the sum of all such disconnected diagrams is given by $\mathcal{G}^\sigma_S(x_{\text{out}}, x_{\text{in}})\,\mathcal{D}^\sigma_{V\backslash S}(\varnothing)$. The sum of all connected diagrams is obtained by removing these contributions for all subsets S from the full sum of diagrams $\mathcal{D}^\sigma_V(x_{\text{out}}, x_{\text{in}})$

$$\mathcal{G}^\sigma_V(x_{\text{out}}, x_{\text{in}}) = \mathcal{D}^\sigma_V(x_{\text{out}}, x_{\text{in}}) - \sum_{S\subsetneq V} \mathcal{G}^\sigma_S(x_{\text{out}}, x_{\text{in}})\,\mathcal{D}^\sigma_{V\backslash S}(\varnothing). \tag{35}$$

This equation involves $\mathcal{G}^\sigma(x_{\text{out}}, x_{\text{in}})$ on both sides. However, the set S on the right is always a subset of V. One can therefore evaluate (35) recursively. In practice, this is done with the following steps:

- One starts by computing and storing $\mathcal{D}^\sigma_S(x_{\text{out}}, x_{\text{in}})$ and $\mathcal{D}^\sigma_S(\varnothing)$ for all $S \subseteq V$. If there are n internal vertices, there are $\binom{n}{k}$ subsets including k vertices. Computing the determinant for one of those subsets has a cost of order $\mathcal{O}(k^3)$. The total computational complexity to compute all determinants is then naively

$$\sum_{k=0}^{n} \binom{n}{k} k^3 \simeq 2^n n^2 \frac{3+n}{8} \sim n^3 2^n \tag{36}$$

  This complexity can be brought down to $\mathcal{O}(2^n)$ using a fast principal minor algorithm [74] that we generalized for several applications within diagrammatic Monte Carlo algorithms [75].

- The next step is to compute the starting point of the recursion $\mathcal{G}^\sigma_\varnothing(x_{\text{out}}, x_{\text{in}})$ which is nothing but the free propagator $G_{0\sigma}(x_{\text{out}}, x_{\text{in}})$.

- Then, all the $\mathcal{G}^\sigma_S(x_{\text{out}}, x_{\text{in}})$ with S containing a single vertex are computed using (35). This only involves $\mathcal{G}^\sigma_\varnothing(x_{\text{out}}, x_{\text{in}})$ which has already been computed.

- The construction continues like this, with $\mathcal{G}^\sigma_S(x_{\text{out}}, x_{\text{in}})$ being computed for all S containing 2 vertices, and then 3, ..., until reaching $S = V$ and thus concluding the calculation of $\mathcal{G}^\sigma_V(x_{\text{out}}, x_{\text{in}})$. At every step with k vertices, only connected contributions involving a number of vertices smaller than k are necessary in (35) and those have already been computed in the recursion. When computing the contribution for a subset with k vertices, the sum in (35) involves 2^k terms. The total complexity is then given by

$$\sum_{k=0}^{n} \binom{n}{k} 2^k = 3^n \tag{37}$$

  This complexity can in principle be reduced to $\mathcal{O}(n^2 2^n)$ using a fast subset convolution technique [76]. It however turns out that for the orders that can be reached and once the overhead for the subset convolution is taken into account, the direct $\mathcal{O}(3^n)$ calculation often performs better.

The CDet algorithm is somewhere between the original DiagMC and a single determinant-based algorithm like CT-INT. At every Monte Carlo step, the contribution from all possible topologies involving the n internal vertices is taken into account. A Monte Carlo configuration is then entirely determined by the set $V = \{x_1, \ldots, x_n\}$ and the sampling has to be done over the possible imaginary times and positions of the internal vertices. The computational cost is dominated by the recursion formula (35) which has exponential complexity $\mathcal{O}(3^n)$. It however turns out that the improvement that this brings in terms of fermionic sign problem eventually makes it a much more powerful algorithm that the original formulation of DiagMC. For the Hubbard model, up to 12-13 coefficients can be computed in favorable cases. Also, importantly, it has been shown that if the series for the physical observable is convergent, the CDet algorithm can reach a given accuracy ϵ in a computational time that is a polynomial in ϵ^{-1} [77].

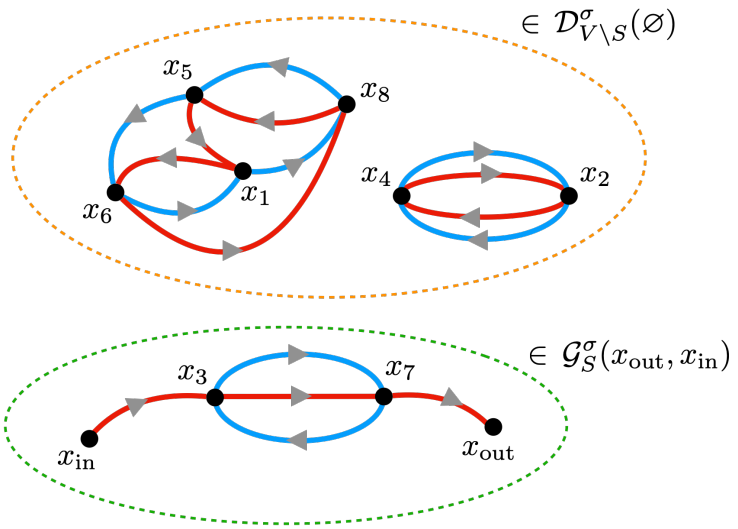

Figure 5: Generic topology of a disconnected diagram. It is composed of a connected part involving the external vertices x_{in} and x_{out} and a subset $S = \{x_3, x_7\} \subsetneq V$ of internal vertices. The other part is a vacuum diagram constructed on the remaining internal vertices in $V \setminus S = \{x_1, x_2, x_4, x_5, x_6, x_8\}$. It does not need to be connected.

3.2 Generalization to one-particle irreducible quantities

The CDet recursion is a method to sum all connected diagrams involving a set V of interaction vertices. The algorithm described for the Green function is easily generalized to quantities such as the double occupancy $\langle n_{r\uparrow} n_{r\downarrow} \rangle$ or other correlators akin to $\langle n_{r\sigma}(\tau) n_{r'\sigma'}(\tau') \rangle$ that can be used to compute spin or charge susceptibilities. When it comes to single-particle properties, it is often important to have access to both the Green function and the associated self-energy. In principle, it is enough to use Dyson's equation to retrieve the self-energy, but it turns out in practice that it leads to very noisy data. We have investigated several approaches to compute the self-energy in order to assess what is the best strategy [78]:

(A) Dyson's equation: The self-energy is simply obtained from the computed Green function via

$$\Sigma_\sigma(x_{\text{out}}, x_{\text{in}}) = G^{-1}_{0\sigma}(x_{\text{out}}, x_{\text{in}}) - G^{-1}_{\sigma}(x_{\text{out}}, x_{\text{in}}). \tag{38}$$

(B) Equation of motion: Using the equations of motion for the Green function, one can show that the self-energy can be obtained as

$$\Sigma_\sigma(x_{\text{out}}, x_{\text{in}}) = \Sigma^{\text{Hartree}}_{\sigma}\, \delta_{x_{\text{out}}, x_{\text{in}}} + \bar{F}_\sigma(x_{\text{out}}, x_{\text{in}}) - \Sigma_\sigma G_\sigma \Sigma_\sigma(x_{\text{out}}, x_{\text{in}}), \tag{39}$$

where $\Sigma^{\text{Hartree}}_{\sigma}$ is the constant Hartree term and $\bar{F}_\sigma$ is the correlation function defined by

$$\bar{F}_\sigma(x_{\text{out}}, x_{\text{in}}) \equiv -U^2 \langle T_\tau n_{\bar{\sigma}} c_\sigma(x_{\text{out}}) n_{\bar{\sigma}} c^\dagger_\sigma(x_{\text{in}}) \rangle. \tag{40}$$

Graphically, the equation for the self-energy can be seen as

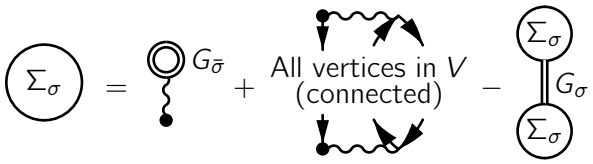

The self-energy is obtained from the correlation function which is the sum of all diagrams with two external interaction vertices connected by all possible combination of propagators. The one-particle-irreducible (1PI) diagrams are filtered out by subtracting all diagrams that are made of two self-energy diagrams connected by a single propagator line [78]. Reorganizing the terms, we can write

$$\Sigma_\sigma = \Sigma_\sigma^{\text{Hartree}} + \bar{F}_\sigma - \left[\bar{F}_\sigma G_{0\sigma} + \Sigma^{\text{Hartree}} G_{0\sigma}\right] \Sigma_\sigma. \tag{41}$$

With the CDet algorithm, the perturbation series for G_σ is computed and used to obtain the Hartree term Σ^{Hartree}. Then, $\bar{F}_\sigma$ is also calculated with the CDet algorithm. Because the perturbation series for $\bar{F}_\sigma$ is at least of order U^2 and that of Σ^{Hartree} at least of order U, the equation (41) provides a recursion for the computation of the series coefficients of the self-energy. The expression (41) does not involve any inversion and is thus expected to provide better results than Dyson's equation with the only additional cost of computing $\bar{F}_\sigma$ which is also of complexity $\mathcal{O}(3^n)$ at order n.

(C) Determinantal approach to sum all 1PI diagrams: The third method is very similar to the equation of motion approach, except that the cancellation to only keep 1PI diagrams is done at every Monte Carlo step, for a given set of internal vertices V, rather than as a post-processing procedure as above. The contribution of the set V to the self-energy is the sum of the Hartree term $UG_V^{\bar{\sigma}}(x_{\text{in}}, x_{\text{in}})\delta_{x_{\text{out}},x_{\text{in}}}$ and a non-local part $\tilde{\Sigma}_V^\sigma(x_{\text{out}}, x_{\text{in}})$ given by

$$\bar{F}_V^\sigma(x_{\text{out}}, x_{\text{in}}) - \sum_{\substack{x'\in V \\ S\subseteq V\setminus\{x'\} \\ S'=V\setminus(S\cup\{x'\})}} F_{S'}^\sigma(x_{\text{out}}, x')\tilde{\Sigma}_S^\sigma(x', x_{\text{in}}) - \sum_{\substack{S\subseteq V \\ S'=V\setminus S}} F_{S'}^\sigma(x_{\text{out}}, x_{\text{in}}) \left(UG_S^{\bar{\sigma}}(x_{\text{in}}, x_{\text{in}})\right), \tag{42}$$

where we have introduced another correlation function that is easily computed in CDet

$$F_\sigma(x_{\text{out}}, x_{\text{in}}) = \Sigma_\sigma G_\sigma(x_{\text{out}}, x_{\text{in}}) \equiv -U\langle T_\tau n_{\bar{\sigma}} c_\sigma(x_{\text{out}}) c_\sigma^\dagger(x_{\text{in}})\rangle. \tag{43}$$

The recursion (42) can again be understood graphically

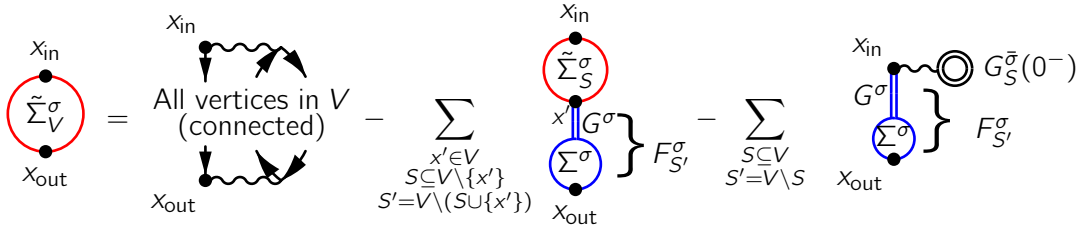

The evaluation of this expression is done recursively for $\tilde{\Sigma}_S^\sigma$ (in red) starting with the order-2 diagram

$$\tilde{\Sigma}^\sigma(x_{\text{in}}, x_{\text{in}}) = \tag{44}$$

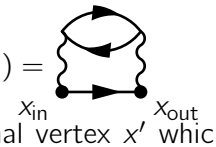

The recursion involves a sum over an internal vertex x' which implies that the correlators F_S^σ have to be computed for all possible pairs of external vertices. This comes with a computational cost $\mathcal{O}(n^2 3^n)$ which dominates the computational time. Eliminating the non-1PI diagrams at every Monte Carlo step is certainly improving the sign problem, but it is not evident whether this compensates for the increased complexity.

We have compared the three approaches described above by computing the self-energy of the two-dimensional Hubbard model

$$\mathcal{H} = -t \sum_{\langle r,r'\rangle,\sigma} c_{r\sigma}^\dagger c_{r'\sigma} + U \sum_r n_{r\uparrow} n_{r\downarrow}, \tag{45}$$

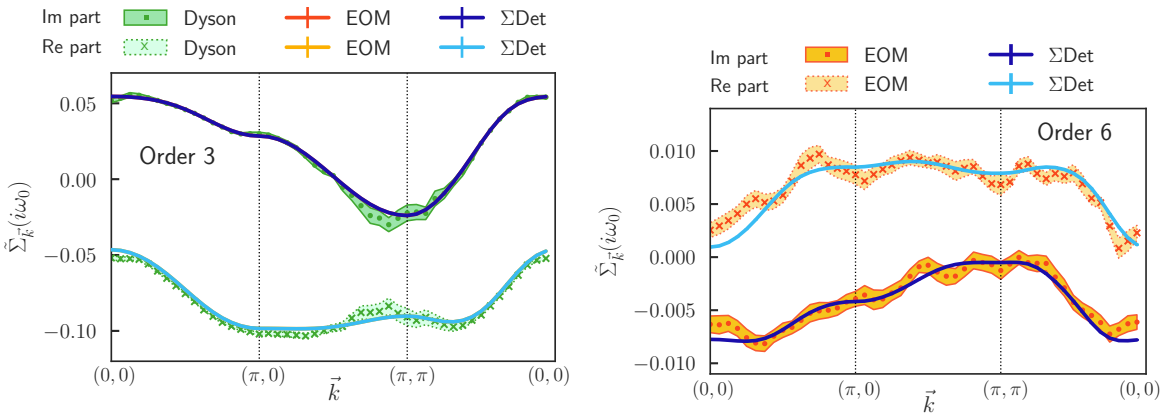

Figure 6: Hubbard model self-energy at the first Matsubara frequency $\tilde{\Sigma}_{\vec{k}}(i\omega_0)$ along the $\vec{k} = (0,0) \to (\pi,0) \to (\pi,\pi) \to (0,0)$ path, as obtained from Dyson's equation (green), the equations of motion approach (orange) and the direct self-energy measurement (blue). Left panel: Contribution at order 3. Right panel: Contribution at order 6 (the Dyson's equation approach is not shown). We use a 32×32 lattice with $\beta t = 2$, $U = 4t$, $\mu = 0$. All simulations lasted 120 CPU hours. Figures taken from [78].

---

with only nearest-neighbor hoppings, on a periodic 32×32 lattice. We will denote the protocols (A), (B), (C) by Dyson, EOM and ΣDet in the following.

In Fig. 6, we display a comparison of different contributions to the self-energy $\Sigma_{\boldsymbol{k},\sigma}(i\omega_0)$ taken at the first Matsubara frequency along a $\boldsymbol{k}$-path in the Brillouin zone and obtained after a simulation of 120 CPU hours. Already at order 3 (left panel), it is clear that Dyson's equation yields much larger error bars and both the EOM and ΣDet are a lot more accurate and have comparable error bars. At order 6 (right panel), Dyson's equation is not able to produce relevant results so we only compare EOM and ΣDet. The EOM approach is shown to have larger variance, a result that continues to be true at larger orders.

The evolution of the variance of the EOM and ΣDet approaches for a selected self-energy as a function of perturbation order is shown in the left panel of Fig. 7. For all computed orders, the variance of the ΣDet is about one order of magnitude smaller than the EOM approach.

The conclusion of this study is that even though the elimination of non-1PI diagrams requires more computational effort in the ΣDet approach (see right panel of Fig. 7), it eventually leads to smaller statistical variance on the evaluation of the self-energy. This is both the result of a more efficient cancellation when it is done for every internal vertex configuration, but it also comes from a more efficient sampling when only self-energy diagrams are kept. Indeed, during the sampling of the F_σ and $\bar{F}_\sigma$ correlators the vertices are less constrained and even though the diagrams are connected they have a larger spatial extent than those involved in the self-energy calculation with a higher irreducibility level. Very similar algorithms to isolate 1PI diagrams have also been described in Ref. [79] and Ref. [80].

3.3 Resummation of the series

The algorithms described above have made it possible to compute more perturbation coefficients. A first application has been a careful study of the weak-to-intermediate regime of the two-dimensional Hubbard model which is described in Sec. 4. However, in the doped case, even with a larger number

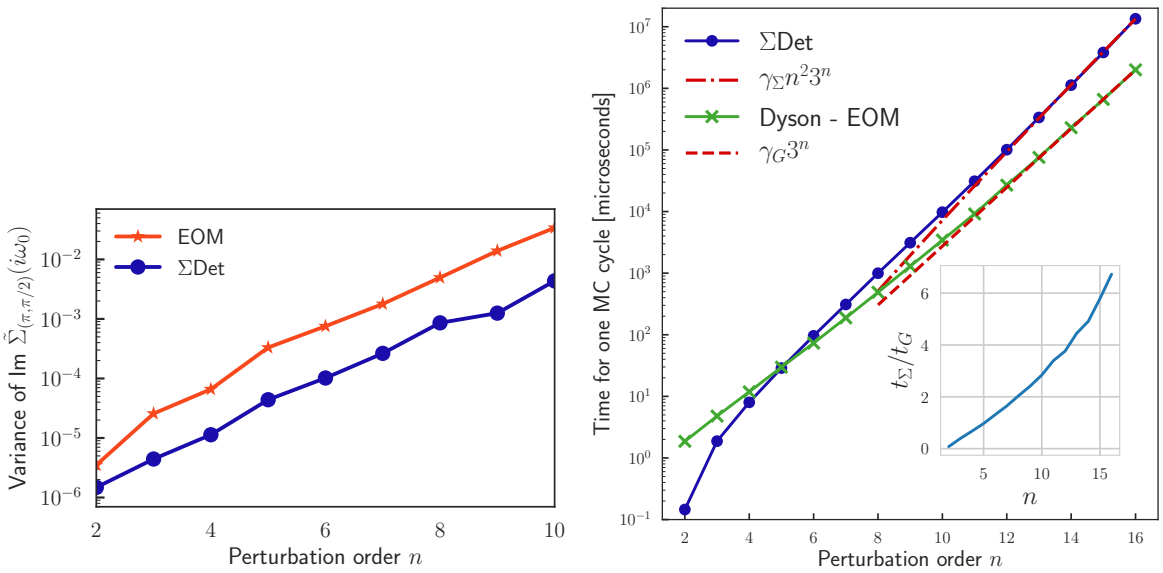

Figure 7: Left panel: Variance of the imaginary part of the Hubbard model self-energy $\mathrm{Im}\Sigma_{(\pi,\pi/2)}(i\omega_0)$. The red line is the EOM approach, while the blue line corresponds to the ΣDet measurement. We use a 32×32 lattice with $\beta t = 2$, $U = 4t$, $\mu = 0$. Right panel: Comparison of the time for one Monte Carlo cycle (in microseconds) between the direct accumulation of the self-energy (blue curve with dots) and the computation of the Green's function using CDet (green curve with dots), on a semilog scale, as a function of the perturbation order n. Each curve is fitted by its expected high-n behavior: $\gamma_\Sigma n^2 3^n$ for the ΣDet (dotted red line) and $\gamma_G 3^n$ for Dyson (dashed red line), where $\gamma_G = 0.0464$ and $\gamma_\Sigma = 0.0012$ are implementation-dependent constants. *Inset*: Ratio of the time of one MC cycle for the ΣDet (t_Σ) and for the CDet (t_G), as a function of the perturbation order n. Figures taken from [78].

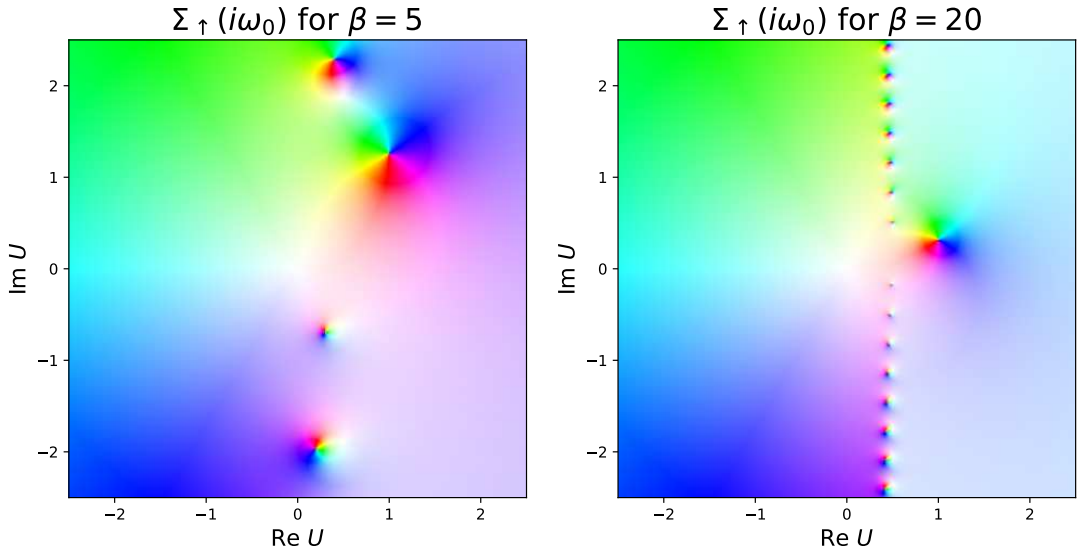

Figure 8: Pole structure of the self-energy of the Hubbard atom with $\epsilon = -1/2$ at the first Matsubara frequency for two temperatures: 1/5 (left panel) and 1/20 (right panel). The color indicates the phase of the complex number and the intensity is proportional to its modulus.

---

of coefficients, the series were difficult to resum in the most interesting regimes of intermediate-to-strong coupling at low temperatures. This difficulty in the doped Hubbard model is not that much a problem of lacking enough coefficients, but mainly comes from the bad behavior of the original series in this regime. Ultimately, it is because the self-energy and other physical observables seen as a function of a complex coupling U have a very non-trivial pole structure. An example of this pole structure can be computed for the simple case of a Hubbard atom, which is a single energy level with a Coulomb repulsion

$$\mathcal{H}_{\text{atom}} = \epsilon \sum_\sigma n_\sigma + U n_\uparrow n_\downarrow. \tag{46}$$

This system can be solved exactly and yields a self-energy

$$\Sigma_\sigma^{\text{atom}}(i\omega_n) = \langle n_\sigma \rangle U + \frac{\langle n_\sigma \rangle (1 - \langle n_\sigma \rangle) U^2}{i\omega_n - \epsilon - (1 - \langle n_\sigma \rangle) U}, \tag{47}$$

where the average occupancy $\langle n_\sigma \rangle$ is

$$\langle n_\sigma \rangle = \frac{e^{-\beta\epsilon} + e^{-\beta(2\epsilon+U)}}{1 + 2e^{-\beta\epsilon} + e^{-\beta(2\epsilon+U)}}. \tag{48}$$

The self-energy at the first Matsubara frequency is shown in the complex plane of U in Fig. 8 for two temperatures. In both cases several poles are seen and their position strongly depends on the physical parameters, such as the temperature.

The closest pole to the origin will set the radius of convergence of the series. In the most favorable situations, the value of interest of U lies within the convergence radius and a simple analysis of the partial sum of the series can be enough to find the value of the observable. But if one is interested in a value of U beyond the convergence radius, it becomes necessary to perform some analytical continuation of the series. There are various methods to do this, many of which have been developed and used in the 60's, at a time when high-temperature series were being studied in the context of statistical physics models. We typically use Padé approximants [81–83], Dlog-Padé approximants [84], integral approximants [85] or conformal maps to evaluate the series beyond its

convergence radius. Comparing the results from different approaches can be used to assess a level of confidence for the resummation.

Unfortunately, the series generally become more difficult to resum in the most interesting regimes. What will in general define the probability of success is the proximity of a pole to the positive real axis. In a situation where the poles lies far from the real positive axis, such as the example on the left panel of Fig. 8, resummation techniques will in general be efficient. When instead a pole is close to the real positive axis and the evaluation has to be done beyond this point (e.g. at $U = 1$ on the right panel of Fig. 8), the resummation will often be impossible. The closer the pole is to the axis, the more coefficients are needed. In practice we observe that by just getting the pole a bit closer to the axis, many more coefficients are quickly needed and because we only have access to $\sim 10 - 12$ coefficients, the resummation becomes the bottleneck of the calculation.

There is no general understanding of what controls the entire pole structure of a physical observable such as the self-energy of the Hubbard model. It is likely that some of the pole have a purely mathematical origin which is not directly connected to a physical property of the system. Other poles, however, do correlate with physical phenomena. For example, if the system displays a second-order phase transition as a function of U, there will be an associated branch cut that goes through the real axis and makes it impossible to resum the series beyond the critical value of U. More generally, if the system moves close to a phase transition, it is expected that some poles will be close to the real axis. An example is the column of poles on the right panel of Fig. 8. As temperature goes to zero, the poles will eventually merge into a branch cut. Its physical origin is the zero-temperature change of particle number at $U_c = 1/2$. Indeed, at zero temperature, the ground state has $\langle n_\uparrow \rangle = 1$ for $U < 1/2$, while it has $\langle n_\uparrow \rangle = 1/2$ for $U > 1/2$. This change of particle number can be seen as a phase transition and has an associated complex pole structure. It is generally believed that regimes (e.g. of the Hubbard model) that are close to a phase transition or that involve very long correlation lengths, will also have intricate pole structures making them difficult to be tackled by perturbation-based techniques.

3.4 Constructing optimized perturbation series

It was soon realized that computing a handful of additional perturbation series coefficients would not solve the inherent difficulty posed by the resummation of the series in situations where poles are lying close to the real axis. This motivated a research direction aiming at formulating different perturbation series yielding the same physical quantities but with better convergence properties [59, 72, 86–90].

3.4.1 The dangers of boldification

A natural approach, which is probably as old as perturbation theory itself, is the boldification of the series: a reorganization of the diagrams in a way that the series is expressed in terms of the interacting propagators rather than the non-interacting ones. While this naturally seems to include more physical content into smaller orders of the perturbation series, it is not clear how the boldification procedure changes the convergence properties of the series. In Ref. [91], we have shown that the bold (skeleton) series for the self-energy of the two-dimensional Hubbard model sometimes convergences to an unphysical solution, see Fig. 9. Our understanding is that this is a consequence of the Luttinger-Ward functional not being a single-valued function [91–95]. In other words, the functional $\Sigma_\sigma[G]$ can have several branches in addition to the physical one and it is impossible to predict if the skeleton expansion for Σ_σ will converge to the physical solution, if it converges at all. This problem is especially dangerous because it is very difficult to

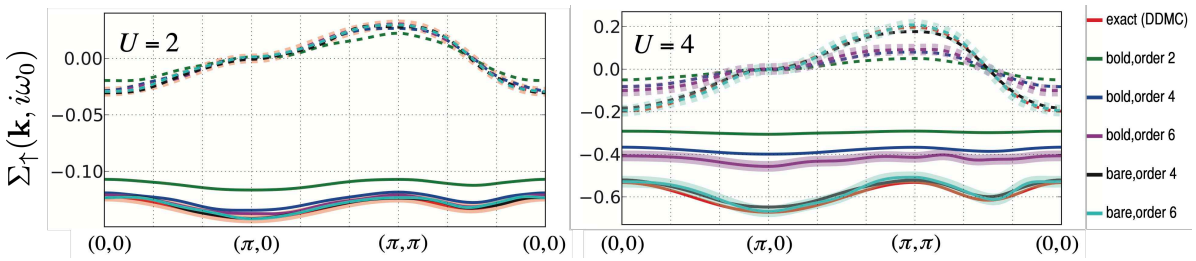

Figure 9: Convergence of the bold (skeleton) and bare series for the self-energy of the two-dimensional Hubbard model at the first Matsubara frequency along a path in the Brillouin zone. The temperature is $T = 0.5t$ and the model is taken at half-filling. The solid and dashed lines correspond to the real and imaginary parts, respectively. Figure adapted from Ref. [91].

---

diagnose whether a converged solution is physical or unphysical [87]. The multivaluedness of the Luttinger-Ward functional has been shown to be related to the divergence of the vertex function and triggered a very interesting series of works investigating the nature and consequences of these divergencies [96–104].

3.4.2 Chemical potential shifts

On the other hand, series expressed in terms of bare (non-interacting) propagators never seem to suffer from misleading convergence. For example, a comparison between the convergence of the bare and of the skeleton series for the self-energy is shown in Fig. 9. The question is then whether there is freedom in the choice of the bare propagator. We have actually already met a change of bare propagators in Sec. 2.1.4 when the α-trick for the CT-INT algorithm was introduced. A very similar strategy can be used to change the bare propagator with an effective shift of the chemical potential. Consider the Hamiltonian

$$\mathcal{H} = \sum_{r,r',\sigma} t_{rr'} c^\dagger_{r\sigma} c_{r'\sigma} - \mu_0 \sum_{r,\sigma} n_{r\sigma} + \xi \frac{(\mu_0 - \mu)}{U} \sum_{r,\sigma} n_{r\sigma} + \xi \sum_r n_{r\uparrow} n_{r\downarrow}, \tag{49}$$

where μ is the physical chemical potential and μ_0 takes an arbitrary value. When $\xi = U$ this Hamiltonian describes the usual Hubbard model with an onsite interaction U at a chemical potential μ. When $\xi = 0$, the Hamiltonian describes non-interacting electrons at a chemical potential μ_0. If we treat ξ as the perturbation expansion parameter, we obtain a series formulated in terms of the modified non-interacting propagator

$$G_{0\sigma}(\boldsymbol{k}, i\omega_n) = \frac{1}{i\omega_n + \mu - \epsilon_{\boldsymbol{k}}} \quad \rightarrow \quad \tilde{G}_{0\sigma}(\boldsymbol{k}, i\omega_n) = \frac{1}{i\omega_n + \mu_0 - \epsilon_{\boldsymbol{k}}}. \tag{50}$$

To compensate for this shift in chemical potential, new diagrams generated by the $\xi((\mu_0 - \mu)/U) \sum_{r\sigma} n_{r\sigma}$ term have to be included in the perturbation series. In the CDet (or ΣDet), this is very easily implemented by just adding an extra term on the diagonal of the matrices (34) entering the recursion (35):

$$M^\sigma_V(x_{\text{out}}, x_{\text{in}}) \rightarrow \tilde{M}^\sigma_V(x_{\text{out}}, x_{\text{in}}) = \begin{pmatrix} \tilde{G}_{0\sigma}(x_1, x_1) - \alpha & \dots & \tilde{G}_{0\sigma}(x_1, x_n) & \tilde{G}_{0\sigma}(x_1, x_{\text{in}}) \\ \tilde{G}_{0\sigma}(x_2, x_1) & \dots & \tilde{G}_{0\sigma}(x_2, x_n) & \tilde{G}_{0\sigma}(x_2, x_{\text{in}}) \\ \vdots & \ddots & \vdots & \vdots \\ \tilde{G}_{0\sigma}(x_n, x_1) & \dots & \tilde{G}_{0\sigma}(x_n, x_n) - \alpha & \tilde{G}_{0\sigma}(x_n, x_{\text{in}}) \\ \tilde{G}_{0\sigma}(x_{\text{out}}, x_1) & \dots & \tilde{G}_{0\sigma}(x_{\text{out}}, x_n) & \tilde{G}_{0\sigma}(x_{\text{out}}, x_{\text{in}}) \end{pmatrix}, \tag{51}$$

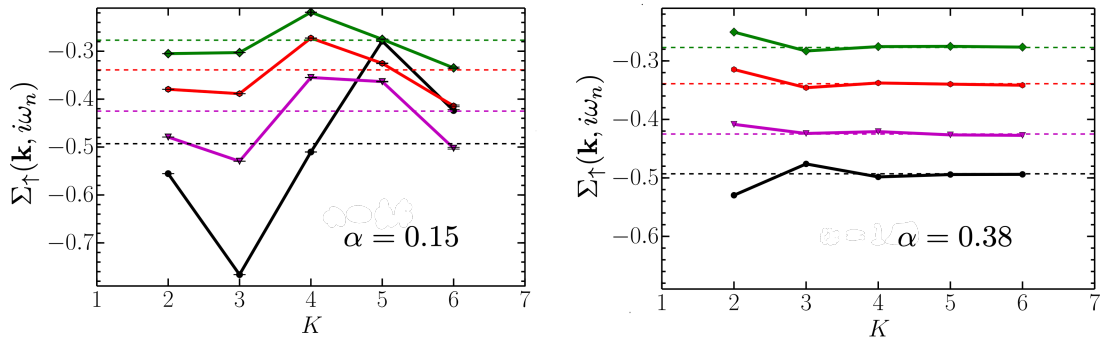

Figure 10: Partial sums up to order K of the series for the imaginary part of self-energy of the Hubbard model with $U = 4t$, $t' = -0.3t$, $\mu = 0$, $T = 0.5t$, $n \sim 0.725$. The results for the first four Matsubara frequencies are shown in black ($n = 0$), magenta ($n = 1$), red ($n = 2$) and green($n = 3$). The panels correspond to two different choices for $\alpha = (\mu_0 - \mu)/U$. The dashed lines are a benchmark from determinantal quantum Monte Carlo [49]. Figure adapted from Ref. [72].

---

where we have introduced $\alpha \equiv (\mu - \mu_0)/U$ to make the connection with the CT-INT algorithm. With these modified propagators and the corresponding compensation terms, the series is now different for every choice of μ_0. However, if they converge, all the series should yield the same physical answer when evaluated at $\xi = U$. Different choices for μ_0 correspond to different ways to reach the physical chemical potential μ at $\xi = U$. Tuning μ_0 (or equivalently α) may therefore lead to series with different convergence properties. Note that the motivation here is different from what drove the introduction of the α-trick in the CT-INT. In the CT-INT, the goal was to reduce the sign problem, and typically different values for $\alpha_\uparrow$ and $\alpha_\downarrow$ were taken. Here, the motivation is to control the pole structure of the physical observable and in general it is not necessary to introduce a spin dependence in $\alpha = \alpha_\uparrow = \alpha_\downarrow$.

We explored the freedom to change the chemical potential of the bare propagator in Ref. [72] and studied how the perturbation series for the self-energy in the Hubbard model was affected. In Fig. 10, we display the partial sums of the series for the self-energy of the Hubbard model on a 16×16 lattice for two different values of α. It clearly appears that some choices lead to much better behaving series that quickly converge to the benchmark values. In this relatively simple regime, a converged solution can already be found with just 4 perturbation orders with a clever choice of α. Some insight into the effect of a changing the bare propagator can be gained by looking at the exactly solvable Hubbard atom (46). Just like for the lattice Hubbard model above, the Hamiltonian can be changed so that the starting point of the perturbation series corresponds to an isolated level at a modified energy $\epsilon_0 = \epsilon + \alpha U$. The self-energy expressed as a function of the expansion parameter ξ is

$$\Sigma_\sigma^{\text{atom}}(i\omega_n) = \langle n_\sigma \rangle \xi + \frac{\langle n_\sigma \rangle (1 - \langle n_\sigma \rangle) \xi^2}{i\omega_n - \tilde{\epsilon} - (1 - \langle n_\sigma \rangle)\xi}, \tag{52}$$

where the average occupancy $\langle n_\sigma \rangle$ is

$$\langle n_\sigma \rangle = \frac{e^{-\beta\tilde{\epsilon}} + e^{-\beta(2\tilde{\epsilon}+\xi)}}{1 + 2e^{-\beta\tilde{\epsilon}} + e^{-\beta(2\tilde{\epsilon}+\xi)}}, \tag{53}$$

and $\tilde{\epsilon} = \epsilon_0 + \xi(\epsilon - \epsilon_0)/U \equiv \epsilon + \alpha U - \xi\alpha$. The pole structure in the plane of the complex variable ξ is shown in Fig. 11. The parameters were chosen so that the density, temperature and coupling are similar to those of the lattice model shown above. Changing the starting point has the effect of moving the poles to different locations in the complex plane. In this example, the optimal value is $\alpha \simeq 0.38$ and the poles have moved outside the circle $\xi = U$ so that the series is converging. For the value $\alpha = 0.15$, poles are still present within the $\xi = U$ circle and the series is not converging.

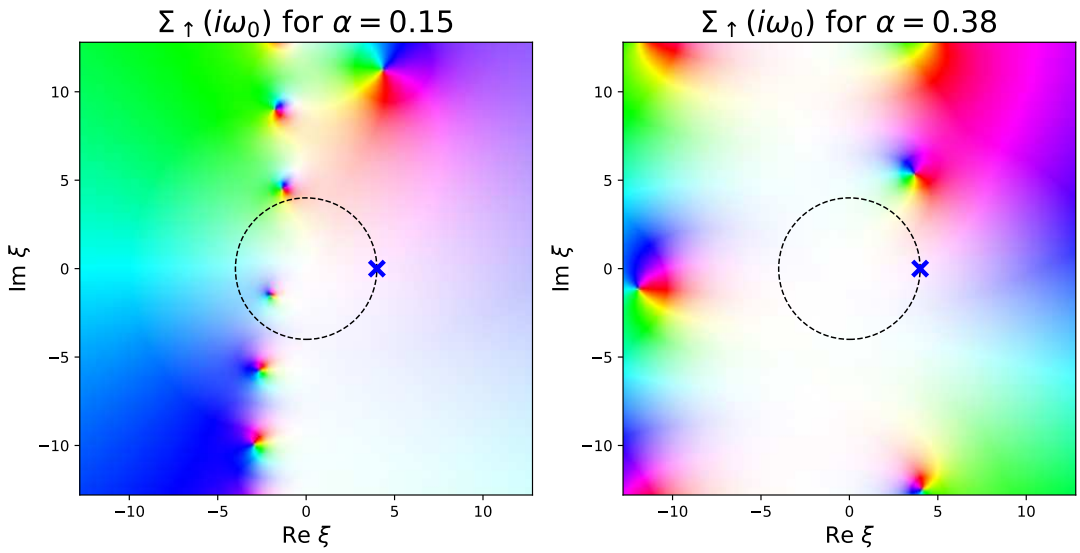

Figure 11: Pole structure of the Hubbard atom self-energy for $U = 4$, $T = 0.5$, $\epsilon = -0.138$, $n \sim 0.725$ and two different values of α. The physical solution is at the cross $\xi = U$ on the unit circle. The color indicates the phase of the complex number and the intensity is proportional to its modulus. Figure adapted from Ref. [72].

Introducing a new degree of freedom offers a handle to improve the convergence properties of the series. But it can become cumbersome to perform lengthy scans for different values of the shifted chemical potential. In practice, it seems that good choices for α are often close to the value $\alpha_{\text{MF}} = \langle n_\sigma \rangle_0$, where the average value is taken in the non-interacting system with chemical potential μ_0. There is some intuition behind this: for this value, the non-interacting propagator is the mean-field solution of the problem. Indeed, α_{MF} is such that

$$\tilde{G}_{0\sigma}(x, x) - \langle n_\sigma \rangle_0 = 0, \tag{54}$$

which is exactly the mean-field equation. From a diagrammatic point of view, starting the expansion around the mean-field solution also reduces the number of diagrams because all diagrams involving a tadpole (a single fermionic loop) vanish. This is a direct consequence of the diagonal of the matrix (51) vanishing for the mean-field propagator. Reducing the number of diagrams typically reduces the contribution from larger order coefficients and incidentally tends to lead to better behaved pole structures.

3.4.3 Renormalized perturbation theory

In the previous section, we derived different series expansions yielding the same physical result by writing a modified Hamiltonian (49) involving a new expansion parameter ξ. For $\xi = U$, the Hamiltonian is equivalent to the physical one, while for $\xi = 0$ it describes non-interacting electrons at a different chemical potential μ_0. Different choices for μ_0 yield different perturbation series in ξ with coefficients that can be computed using the CDet algorithm. Another way to think about the new series coefficients is to start by writing the non-interacting propagator as

$$G_{0\sigma}(\boldsymbol{k}, i\omega_n) = \frac{1}{i\omega_n + \mu_0 + \xi\alpha - \epsilon_{\boldsymbol{k}}}, \tag{55}$$

where $\alpha = (\mu - \mu_0)/U$. When $\xi = U$ the original bare propagator is found, while for $\xi = 0$ it corresponds to the modified propagator $\tilde{G}_{0\sigma}$ for the electrons at the chemical potential μ_0. We

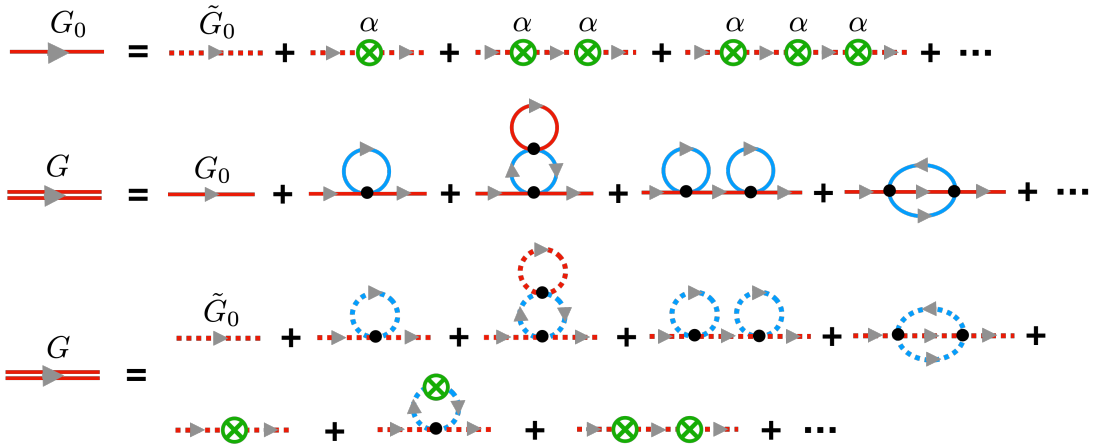

Figure 12: Diagrammatic interpretation of the chemical potential shift. The first row is the series expansion of $G_{0\sigma}$ in terms of the modified $\tilde{G}_{0\sigma}$. When this series is injected in the original perturbation expansion of G_σ (second row) one obtains a new series for G_σ in terms of the modified propagators $\tilde{G}_{0\sigma}$ (third row). It includes an additional family of diagrams with α-insertions.

---

can expand $G_{0\sigma}$ in powers of ξ

$$G_{0\sigma}(\boldsymbol{k}, i\omega_n) = \tilde{G}_{0\sigma} - \xi \tilde{G}_{0\sigma}\alpha\tilde{G}_{0\sigma} + \xi^2 \tilde{G}_{0\sigma}\alpha\tilde{G}_{0\sigma}\alpha\tilde{G}_{0\sigma} + \dots . \tag{56}$$

The modified series in ξ can be retrieved by substituting the bare propagators $G_{0\sigma}$ in the original series with the expression above and gathering all terms involving the n powers of ξ into the corresponding order-n coefficient. Diagrammatically, every propagator line $G_{0\sigma}$ is replaced by a sum of propagator lines $\tilde{G}_{0\sigma}$ involving an arbitrary number of α-insertions that all account for an additional power of ξ, see Fig. 12. The new series is therefore constructed from the usual diagrams with modified propagators $\tilde{G}_{0\sigma}$ and an additional class of diagrams, where a certain number of α-insertions appear.

Generalizing the chemical potential shift approach The chemical potential shift gives a very specific form for the expression (56) of the bare propagator in powers of ξ. It is very tempting to ask whether one could design a more general renormalization scheme, where G_0 would be any function of ξ. This generic renormalization is the topic of our work in Ref. [88]. In order to have a flexible framework to derive a renormalization perturbation theory, it is useful to write the action of the model with a space and time dependent local interaction $\xi(x)$, where $x = (\boldsymbol{r}, \tau)$ is a space-time index. The action becomes a functional of ξ and reads

$$S_{\text{bare}}[G_0, \xi] = -\sum_\sigma \int dx dx'\, c^\dagger_\sigma(x) G^{-1}_{0\sigma}(x, x') c_\sigma(x') + \int dx\, \xi(x) n_\uparrow(x) n_\downarrow(x). \tag{57}$$

The physical result is recovered for $\xi(x) = U$. Constructing a perturbation expansion in powers of ξ, one obtains the series for the Green function

$$G_\sigma(x_{\text{out}}, x_{\text{in}})[\xi] = \sum_{n=0}^{\infty} \frac{(-1)^n}{n!} \int dx_1 \cdots dx_n\, \mathcal{G}^\sigma_{\{x_1,\dots,x_n\}}(x_{\text{out}}, x_{\text{in}})\, \xi(x_1) \cdots \xi(x_n). \tag{58}$$

The coefficients $\mathcal{G}^\sigma_{\{x_1,\dots,x_n\}}$ can be computed using the usual CDet algorithm with non-interacting propagators G_0. A general renormalization scheme is realized by substituting G_0 above with $G_0[\xi]$, a chosen functional of the interaction ξ that we decompose as

$$G^{-1}_{0\sigma}[\xi] = G^{-1}_{R\sigma} + \Delta_{R\sigma}[\xi]. \tag{59}$$

The functional $\Delta_R[\xi]$ can be any series in ξ with the only property that $G_{0\sigma}[\xi = 0] = G_{R\sigma}$ when $\xi = 0$ and the original bare propagator is recovered when $\xi = U$, namely $G_{0\sigma}[\xi = U] = G_{0\sigma}$. For example, the chemical potential shifted propagator (55) corresponds to the choice $G_{R\sigma} = \tilde{G}_{0\sigma}$ and $\Delta_{R\sigma}(x, x')[\xi] = \xi(x)\alpha\delta(x - x')$. When inserted in the action, the renormalized propagator defines a renormalized action

$$S_R[G_R, \xi] = S_{\text{bare}}[G_0[\xi], \xi] = -\sum_\sigma \int dx dx'\, c^\dagger_\sigma(x) G^{-1}_{0\sigma}(x, x')[\xi] c_\sigma(x') + \int dx\, \xi(x) n_\uparrow(x) n_\downarrow(x). \tag{60}$$

Starting from the functional S_R, our goal is to obtain the series expansion of the corresponding Green function in powers of ξ

$$\begin{aligned} \tilde{G}_\sigma(x_{\text{out}}, x_{\text{in}})[\xi] &= \sum_{n=0}^{\infty} \frac{(-1)^n}{n!} \int dx_1 \cdots dx_n\, \mathcal{G}^\sigma_{\{x_1,\ldots,x_n\}}(x_{\text{out}}, x_{\text{in}})[\xi]\, \xi(x_1) \cdots \xi(x_n) \\ &= \sum_{n=0}^{\infty} \frac{(-1)^n}{n!} \int dx_1 \cdots dx_n\, \tilde{\mathcal{G}}^\sigma_{\{x_1,\ldots,x_n\}}(x_{\text{out}}, x_{\text{in}})\, \xi(x_1) \cdots \xi(x_n). \end{aligned} \tag{61}$$

In this equation, $\mathcal{G}^\sigma_{\{x_1,\ldots,x_n\}}(x_{\text{out}}, x_{\text{in}})[\xi]$ can in principle be computed by simply replacing G_0 with $G_0[\xi]$ in the CDet algorithm. When evaluated at $\xi = U$, $\tilde{G}_\sigma[U] = G_\sigma$ and the physical Green function is found, while at $\xi = 0$ it will be equal to G_R. Formally speaking, the series coefficients $\tilde{\mathcal{G}}^\sigma_{\{x_1,\ldots,x_n\}}(x_{\text{out}}, x_{\text{in}})$ of the renormalized series for a given set of internal vertices are given by the functional derivative

$$\tilde{\mathcal{G}}^\sigma_{\{x_1,\ldots,x_n\}}(x_{\text{out}}, x_{\text{in}}) = \frac{\delta^n \tilde{G}_\sigma(x_{\text{out}}, x_{\text{in}})[\xi]}{\delta\xi(x_1) \cdots \delta\xi(x_n)}. \tag{62}$$

While this expression is certainly correct, it is not easily implemented numerically and we need a general strategy to evaluate such functional derivatives.

Zeon algebras A possible approach to isolate the contribution of a given set of vertices is to evaluate the functional (61) for a special choice of the function ξ that involves a collection of commuting null-square variables defining a zeon algebra. More precisely, the n-particle zeon algebra is defined as the abelian algebra generated by the collection $\{z_i\}$ with $1 \leq i \leq n$ along with the scalar $1 = z_0$ subject to the following rules:

$$z_i z_j = z_j z_i \quad \text{for} \quad i \neq j \quad \text{and} \quad z_i^2 = 0 \quad \text{for} \quad 1 \leq i \leq n. \tag{63}$$

Any element in the algebra can be seen as a polynomial

$$Q(z_1, \ldots, z_n) = \sum_{S \subseteq V} q(S) \prod_{j \in S} z_j, \tag{64}$$

where $V = \{z_1, \ldots, z_n\}$ and there is a total of 2^n coefficients $q(S)$. In order to compute the functional derivative (62), it is enough to evaluate $\tilde{G}_\sigma(x_{\text{out}}, x_{\text{in}})[\xi]$ for the special case

$$\xi(x) = \sum_{j=1}^{n} z_j\, \delta(x - x_j) \tag{65}$$

and the prefactor of the $z_1 \cdots z_n$ term in the resulting polynomial will yield the series coefficient $\tilde{\mathcal{G}}^\sigma_{\{x_1,\ldots,x_n\}}(x_{\text{out}}, x_{\text{in}})$. Intuitively, evaluating a functional at ξ given by (65) will filter out only the contributions that come from the specific values of the given internal vertices $\{x_1, \ldots, x_n\}$. The coefficient associated for example with the term in $z_3 z_4 z_7$ in the polynomial describes the contribution that involves only the internal vertices x_3, x_4, x_7. In that respect, the zeon algebra can the thought of as a mathematical bookkeeping device.

Replacing ξ with (65) means that we will have to manipulate polynomials of zeon variables. Addition and subtraction are trivially implemented. The multiplication of two polynomials Q_1 and Q_2 involves a sum over all subsets of $V = \{z_1, \ldots, z_n\}$. Indeed, let

$$Q_3(z_1, \ldots, z_n) = Q_1(z_1, \ldots, z_n) Q_2(z_1, \ldots, z_n). \tag{66}$$

If $q_i(S)$ is the coefficient of $\prod_{j \in S} z_j$ in $Q_i(z_1, \ldots, z_n)$ then we have that

$$q_3(V) = \sum_{S \subsetneq V} q_1(S) q_2(V \setminus S). \tag{67}$$

This operation can be done in $\mathcal{O}(2^n)$ operations. The division

$$Q_3(z_1, \ldots, z_n) = Q_1(z_1, \ldots, z_n) / Q_2(z_1, \ldots, z_n) \tag{68}$$

is instead obtained from a subset convolution and requires $\mathcal{O}(3^n)$ operations in the recursion:

$$q_3(V) = q_1(V) - \sum_{S \subsetneq V} q_3(S) q_2(V \setminus S). \tag{69}$$

The recursion (69) is very reminiscent of the CDet recursion (35). There is simple reason for that: The CDet formula can be found from the fraction (16) where the interaction U is replaced by (65)

$$G_\sigma[\xi] = G_\sigma(z_1, \ldots, z_n) = \frac{Z G_\sigma(z_1, \ldots, z_n)}{Z(z_1, \ldots, z_n)}. \tag{70}$$

Recognizing $\mathcal{D}^\sigma_V(\varnothing)$, $\mathcal{D}^\sigma_V(x_{\text{out}}, x_{\text{in}})$ and $\mathcal{G}^\sigma_V(x_{\text{out}}, x_{\text{in}})$ in (35) as the coefficients of the polynomials $Z(z_1, \ldots, z_n)$, $Z G_\sigma(z_1, \ldots, z_n)$ and $G_\sigma(z_1, \ldots, z_n)$, respectively, one sees that the fraction exactly leads to the CDet formula.

The renormalized perturbation series algorithm (RDet) In practice, RDet algorithm is implemented as follows:

1. At a given Monte Carlo step, a certain configuration of internal vertices $V = \{x_1, \ldots, x_n\}$ is sampled during the computation of the order n contribution to the Green function.

2. First, the renormalized bare propagator (59) is evaluated for ξ given by (65). This will yield a polynomial $G_{0\sigma}(z_1, \ldots, z_n)$.

3. This polynomial is inserted in the matrices (34) and the CDet recursion (35) is computed. As a result, the polynomials $\tilde{\mathcal{G}}^\sigma_S(z_1, \ldots, z_n)$ are obtained for all $S \subseteq V$. Eventually, the contribution of the internal vertices V to the Green function coefficient $\tilde{\mathcal{G}}^\sigma_V(x_{\text{out}}, x_{\text{in}})$ at order n in ξ is given by the prefactor of the $z_1 \cdots z_n$ term in the polynomial

$$P(z_1, \ldots, z_n) = \sum_{S \subseteq V} \frac{(-1)^{|S|}}{|S|!} \tilde{\mathcal{G}}^\sigma_S(z_1, \ldots, z_n) \prod_{j \in S} z_j, \tag{71}$$

   where $|S|$ is the cardinality of the set S.

4. Note that both steps above involve manipulations of polynomials with zeon variables which are computationally more expensive than similar operations with usual complex numbers.

5. It can be shown that the numerical complexity for the calculation of the coefficient in the renormalized perturbation series is $\mathcal{O}(n^3 4^n)$.

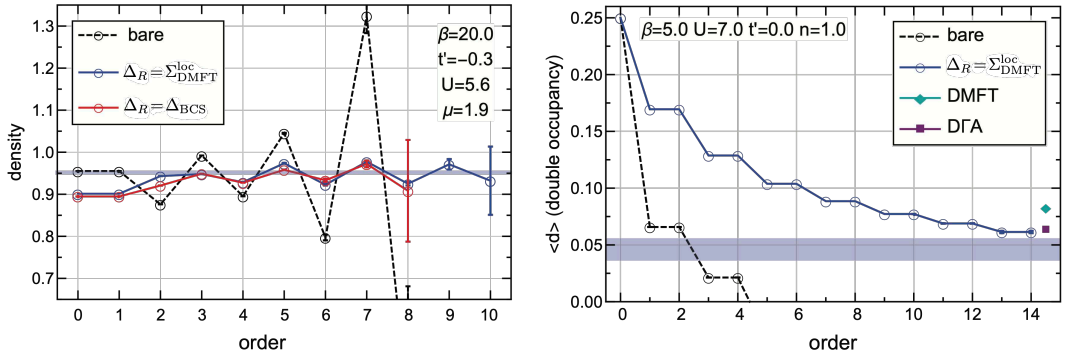

Figure 13: Comparison of the bare series with the renormalized series defined by (72) with two choices for Δ_R. The system considered is the two-dimensional Hubbard model. Left panel: Partial sum for the density for the parameters shown in the label. They correspond to a hole doping of about 5%. Right panel: Partial sum for the double occupancy for the parameters shown in the label. The system is half-filled. The result from DMFT and $D\Gamma A$ are shown for comparison. Figure adapted from Ref. [88].

Convergence properties of the renormalized series We have investigated the following form for the renormalized bare propagator functional

$$G_{0\sigma}^{-1}(x,x')[\xi] = G_{0\sigma}^{-1}(x,x') - \Delta_R(x,x') + \xi(x)\xi(x')\Delta_R(x,x')/U^2. \tag{72}$$

The function $\Delta_R(x,x')$ can be chosen freely. We considered two possibilities

1. A BCS-inspired ansatz with
$$\Delta_R(\boldsymbol{k}, i\omega_n) = \frac{\Delta^2}{i\omega_n + \gamma\epsilon_{\boldsymbol{k}}}. \tag{73}$$
The motivation behind this choice is to construct the perturbation series around a free propagator that already has suppressed fermionic excitations. It may be useful to analyze the Hubbard model in regimes where the solution is expected to have incoherent metallic behavior.

2. A bare propagator constructed from a DMFT solution
$$\Delta_R(\boldsymbol{k}, i\omega_n) = \Sigma^{\rm loc}_{\rm DMFT}(i\omega_n), \tag{74}$$
where $\Sigma^{\rm loc}_{\rm DMFT}$ is the self-energy obtained from the DMFT solution of the considered model. In this case again, the bare propagator is expected to already display some properties of the interacting solution and may prove to be a good starting point.

We compare the series generated by the two choices above with the results of the original bare series (that do include a chemical potential shift) computed for the two-dimensional Hubbard model. The partial sums as a function of perturbation order for the density in the doped $t' = -0.3t$ regime and for the double occupancy at half-filling are shown in Fig. 13. For both these examples, the bare series strongly diverges and resummation tools have a very difficult time to provide an accurate result. Instead, the renormalized series have a much better behavior and can be evaluated at the physical value of U with Padé approximants. It is interesting to note, that even though the computational effort to compute the renormalized coefficients is more important, more coefficients can be obtained (as many as 14 for the double occupancy). The reason is the reduced variance and the more local sampling of vertices in the renormalized case.

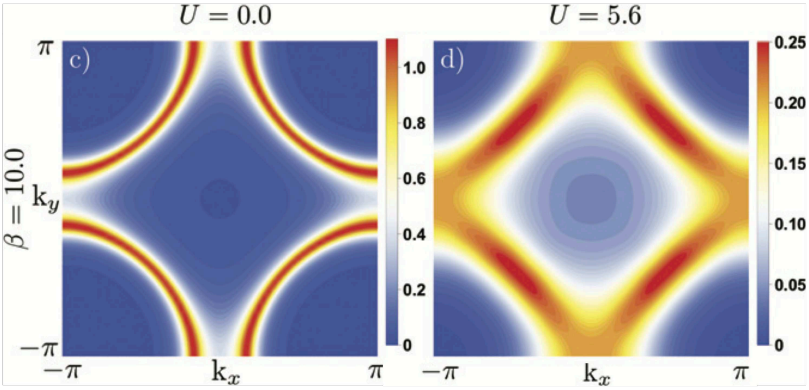

Figure 14: Spectral function $A(\boldsymbol{k})$ for the hole-doped two-dimensional Hubbard model with $t' = -0.3t$ at $n \simeq 0.95$ and $T = 0.1t$ as obtained from the RDet algorithm with the renormalized propagator defined by (72) and $\Delta_R = \Sigma^{\text{loc}}_{\text{DMFT}}$. Figure adapted from Ref. [88].

We have also computed the spectral function in the hole-doped two dimensional Hubbard model using the RDet algorithm with $\Delta_R = \Sigma^{\text{loc}}_{\text{DMFT}}$. The result is shown in Fig. 14. In this regime, the Hubbard model already displays a clear nodal/antinodal dichotomy with more coherent quasi-particles at the node and a suppression of spectral weight close to the antinode. Our previous diagrammatic Monte Carlo calculations in Ref. [72] could evaluate 7 perturbation orders at temperature $T = 0.2t$, while here we are able to reach $T = 0.1t$ with 10 perturbation orders. We can conclude that using renormalized series may be a useful tool to investigate systems in their strong coupling regime. More work is however needed to understand how the choice of Δ_R needs to be tuned to a given physical problem. Let us finally mention that we have also designed a similar scheme with an implementation of a one-loop renormalization of the interaction vertex [89].

3.5 Broken-symmetry perturbation series

It is often believed that perturbation-based approaches are not suited for the investigation of phase transitions. Indeed, when a second-order phase transition is triggered by an increase of the perturbation expansion parameter, such as the coupling U, it will appear as a branch cut in the complex-U plane of physical observables. This makes any attempt to resum the series at values of the coupling inside the ordered phases hopeless. There is however a scheme that makes it possible to circumvent this difficulty and study systems in the vicinity of phase transitions using broken-symmetry perturbation series. This possibility comes from the freedom in choosing the starting point of the perturbation expansion. For concreteness, we will focus on the example of the antiferromagnetic phase in the half-filled three-dimensional Hubbard model, but similar derivations can be made for other ordered phases and other models. In a similar way as we did for shifted chemical potential expansions in Sec. 3.4.2, we introduce a Hamiltonian

$$\mathcal{H} = -t \sum_{\langle \boldsymbol{r},\boldsymbol{r}'\rangle,\sigma} c^\dagger_{\boldsymbol{r}\sigma} c_{\boldsymbol{r}'\sigma} - \left(1 - \frac{\xi}{U}\right) h \sum_{\boldsymbol{r}} p_{\boldsymbol{r}} S^z_{\boldsymbol{r}} + \xi \sum_{\boldsymbol{r}} (n_{\boldsymbol{r}\uparrow} - \frac{1}{2})(n_{\boldsymbol{r}\downarrow} - \frac{1}{2}), \tag{75}$$

where the first term describes a nearest-neighbor hopping, $S^z_{\boldsymbol{r}} = (n_{\boldsymbol{r}\uparrow} - n_{\boldsymbol{r}\downarrow})/2$ and $p_{\boldsymbol{r}} = \pm 1$ depending on whether $\boldsymbol{r}$ belongs to one or the other sub-lattice of the bipartite cubic lattice. When $\xi = U$, this Hamiltonian describes the Hubbard model with an onsite interaction U with no external magnetic field, which is the system that we are interested in. For $\xi = 0$, it instead describes non-interacting electrons in a staggered magnetic field h. For any value of $\xi \neq U$, the Hamiltonian (75) describes a spin broken-symmetry system in a staggered field of amplitude $(1-\xi/U)h$. Constructing

the perturbation series in ξ around a state which is readily symmetry broken has the advantage that one can reach the possibly ordered state at $\xi = U$ without going through a phase transition and singularities in the complex-ξ plane may be avoided. The value of the artificial external field h does not change the properties of the model at $\xi = U$ and one can use h as a tuning parameter to optimize the convergence properties of the broken-symmetry series. In practical terms, the broken-symmetry perturbation series is easily implemented by replacing the usual non-interacting propagators with the non-interacting propagator $\tilde{G}_{0\sigma}$ of the system in the presence of the staggered magnetic field. The matrices (34) appearing in the recursion (35) acquire an extra $hp_{\mathbf{r}}\sigma/2U$ term on the diagonal.

We have used this approach to compute the properties of the magnetically-ordered phase of the three-dimensional Hubbard model [105] which will be discussed in Sec. 5 below. We have also constructed a similar expansion around a BCS state in order to study the phase transition between the superconducting and the normal phase of the negative-U three-dimensional Hubbard model in an external Zeeman field [106].

4 Weak-to-intermediate coupling regime of the half-filled Hubbard model in two dimensions

One of the first applications of the improved DiagMC algorithms described above has been the systematic study of the half-filled two-dimensional Hubbard model

$$\mathcal{H} = -t \sum_{\langle \boldsymbol{r},\boldsymbol{r}'\rangle,\sigma} c^\dagger_{\boldsymbol{r}\sigma} c_{\boldsymbol{r}'\sigma} - \frac{U}{2}\sum_{\boldsymbol{r},\sigma} n_{\boldsymbol{r}\sigma} + U \sum_{\boldsymbol{r}} n_{\boldsymbol{r}\uparrow} n_{\boldsymbol{r}\downarrow}, \tag{76}$$

where the first term only includes a hopping t between nearest-neighbor sites of a square lattice and the chemical potential has been set to $\mu = U/2$ to ensure that $\langle n_\sigma \rangle = 1/2$. This model has particle-hole symmetry and its non-interacting Fermi surface follows the antiferromagnetic Brillouin zone. The density of states $\rho(\omega)$ associated to the dispersion $\epsilon_{\boldsymbol{k}} = -2t(\cos(k_x) + \cos(k_y))$ has a van Hove singularity at $\omega = 0$ stemming from the flat dispersion around the $(\pm\pi, 0), (0, \pm\pi)$ points in the Brillouin zone.

4.1 Crossover from a metallic state to a quasi-ordered insulating-like state

At zero temperature, the ground state of (76) is an antiferromagnet for all values of $U > 0$. At weak coupling, this is a consequence of the $\boldsymbol{q} = (\pi, \pi)$ nesting property of the Fermi surface which creates a Slater [107] antiferromagnetic band insulating state. At finite temperature $T > 0$, long-range order is forbidden by the Mermin-Wagner theorem [108, 109]. Nevertheless, one can expect that there is a regime above $T = 0$ where the antiferromagnetic correlation length ξ is very large and grows exponentially with $1/T$. The fact that diagrammatic Monte Carlo can reach large system sizes makes it a good method to address these regimes that are challenging for other many-body techniques. The left panel of Fig. 15 summarizes the first systematic results obtained with the ΣDet algorithm in Ref. [110] in the weak-to-intermediate coupling regime.

Four different regions appear. At high temperatures $T \gtrsim 0.4t$, thermal fluctuations prevent the formation of long-lived quasiparticles and the system is incoherent. For $U \lesssim 3t$ and as temperature is decreased, a metallic region (M) with coherent quasiparticles appears. This crossover happens around a temperature T^N_{QP} at which the thermal de Broglie wavelength $v^*_F/(\pi T)$ along the nodal $(\pi/2, \pi/2)$ direction becomes larger than the lattice spacing. Here v^*_F is the renormalized Fermi velocity. In the metallic region, the self-energy $\Sigma(\boldsymbol{k}, i\omega_n)$ is metallic-like and characterized by a negative slope of its imaginary part at low Matsubara frequencies

$$\mathrm{slope}\left(\Sigma(\boldsymbol{k}, i\omega_n)\right) = \left.\frac{d\mathrm{Im}\Sigma(\boldsymbol{k}, i\omega)}{d i\omega}\right|_{\omega\to 0} < 0. \tag{77}$$

Note that because of the perfect nesting property of the Fermi surface, this metallic state is not a proper Fermi liquid (see Ref. [34] for an in-depth discussion). When the temperature is further decreased or if the interaction strength is increased, the magnetic correlation length gradually increases [111]. The associated antiferromagnetic fluctuations enhance the quasiparticle scattering rate and eventually lead to the formation of a pseudogap in the single-particle spectrum. The system becomes a quasi-ordered insulating-like state (I). The crossover between the metallic state and this insulating-like state can be characterized by the change of slope of the imaginary part of the self-energy $\Sigma(\boldsymbol{k}, i\omega_n)$. With increasing U or decreasing T, the change of slope is first observed at the antinode $\boldsymbol{k} = (\pi, 0)$ (red points) and is followed by the node $\boldsymbol{k} = (\pi/2, \pi/2)$ (blue points). There is a small non-Fermi liquid (nFL) region, where the nodal self-energy is still metallic-like, while it is insulating like at the antinode.

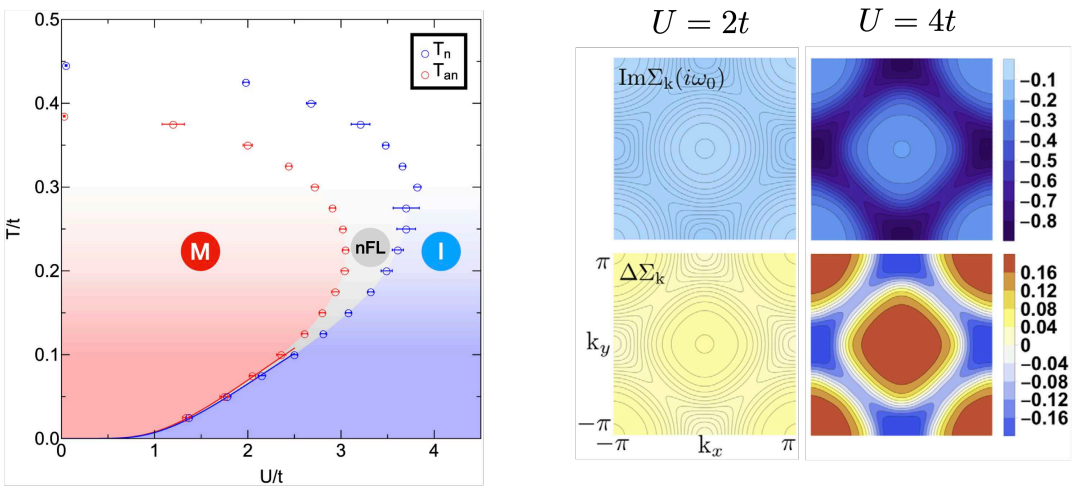

Figure 15: Left panel: Phase diagram as obtained from ΣDet for the half-filled two-dimensional Hubbard model in the weak-to-intermediate coupling regime. The red area (M) is a good metal, the blue region (I) is a quasi-ordered insulating-like state. They are separated by a non-Fermi liquid region (nFL). The red (blue) points are determined from the change of slope of the antinodal (nodal) self-energy at low Matsubara frequencies. Right panel: Imaginary part of the self-energy at the first Matsubara frequency (top row) and the difference between the values at the first two Matsubara frequencies (bottom row) as a proxy for the slope. The temperature is $T = 0.2t$. Adapted from Ref. [110].

A more detailed description of the self-energy in the metallic and insulating-like region in shown in the right panel of Fig. 15. In the metallic state at $T = 0.2t$ and $U = 2t$, the self-energy is very uniform over the Brillouin zone and its slope is negative for all values of $\boldsymbol{k}$. On the contrary, in the insulating regime, at $T = 0.2t$ and $U = 4t$, there is significant momentum differentiation and $\mathrm{Im}\Sigma(\boldsymbol{k}, i\omega_0)$ is more negative (with a positive slope) along the antiferromagnetic Brillouin zone and even a bit more so at the antinode. The resulting large scattering rate is responsible for the destruction of coherent quasiparticles in this regime.

As previously discussed in Refs [112–114], the formation of a quasi-ordered insulating state pre-empts the Mott transition observed in single-site dynamical mean-field theory [43] and its cluster extensions [115, 116]. It is still an open question whether there is some signal of a Mott transition at a finite value of U inside the quasi-ordered state. This regime is currently not reachable by the ΣDet algorithm. Indeed, when the correlation length becomes very large, it is likely that a pole appears close to the real axis in the complex-U plane of the self-energy. This makes the resummation increasingly difficult and resummation can only be carried out for values of U just a bit larger than the crossover scale depicted on Fig. 15.

4.2 A multi-method, multi-messenger study

The possibility to obtain unbiased results in the weak-to-intermediate coupling regime was one of the motivations to carry out a comparative study of the Hubbard model (76) with a comprehensive set of state-of-the-art many-body methods [34]. Our study provides an assessment of the ability of different methods to properly describe the regimes discussed above and elucidates the role of spin fluctuations using several (multi-messenger) physical observables. We focus on the specific value $U = 2t$ and analyze the properties of the Hubbard model as a function of the temperature T. The algorithms that we considered in our study can be organized in different groups:

1. **Benchmark methods**. We have used the CDet and ΣDet algorithms described above as well as determinantal quantum Monte Carlo (DQMC) [49–53] to obtain benchmark results down to temperatures $T \simeq 0.06t$. Both methods are numerically exact and can compute both single- and two-particle response functions.

2. **Mean-field methods**. The dynamical mean-field theory (DMFT) [43–45] provides a very useful reference point beyond which spatial fluctuations must be included.

3. **Cluster extension of DMFT**. Two possible ways to include spatial correlations within the DMFT framework are the dynamical cluster approximation (DCA) [46, 117, 118] and cellular DMFT (CDMFT) [46, 115, 119, 120] that we used with its center-focused extrapolation [121]. They are controlled approximations, but are limited by the size of the cluster that can be computed.

4. **Vertex-based extensions of DMFT**. Spatial correlations within dynamical mean-field theory methods can also be included by computing higher-order Green functions. We have obtained results with the dynamical vertex approximation (DΓA, ladder version) [112, 114, 122], the triply irreducible local expansion (TRILEX) [123–125] in various flavors, the dual fermion (DF, ladder version) [126–128] and the dual boson (DB, single-shot) [129–131] approaches [47].

5. **Other approaches**. We have also included results from the two-particle self-consistent approach (TPSC, TPSC+) [132, 133], the functional renormalization group (fRG) [134] (up to one loop with Katanin substitution) and the parquet approximation (PA) [135, 136].

In the following, we will discuss some selected results from our work [34] and compare the methods above in the different regimes of the model. It is useful to start with the dynamical mean-field description of the half-filled Hubbard model to then start assessing the role of non-local spatial correlations.

4.3 Dynamical mean-field solution

Within the dynamical mean-field theory, local fluctuations are taken into account, but spatial fluctuations are ignored. The results of the dynamical mean-field theory can therefore be used as a simple starting point to then evaluate the role of non-local spatial correlations. The DMFT phase diagram is shown in Fig. 16. Just like the exact phase diagram in Fig. 15, it shows a high-temperature incoherent state which turns into a metallic state in the weak-coupling regime as temperature is decreased below $T \simeq T_{\text{QP}}^{\text{DMFT}}$. Because DMFT does not take spatial fluctuations into account, the Mermin-Wagner theorem is not satisfied and the DMFT solution has a second-order phase transition to an ordered antiferromagnetic state at a finite Néel temperature $T_{\text{Néel}}^{\text{DMFT}}$. The temperature at which this phase transition appears can be interpreted as the temperature at which the magnetic correlation length becomes very large in the exact solution that does however not allow for magnetic order. Taken together, the temperatures $T_{\text{QP}}^{\text{DMFT}}$ and $T_{\text{Néel}}^{\text{DMFT}}$ define crossover lines that are in fairly good agreement with the exact result. The magnetic correlation length ξ obtained by DMFT and static mean-field theory is shown on the right panel of Fig. 16. The correlation lengths diverge at the Néel temperature predicted by the two methods, $T_{\text{Néel}}^{\text{MFT}}$ and $T_{\text{Néel}}^{\text{DMFT}}$. It is interesting to see that the correlation length predicted by DMFT is very close to the DiagMC one down to temperatures $T \simeq 0.1t$.

It is instructive to compare the self-energy obtained by DMFT with the benchmark self-energy. This is shown in Fig. 17. The top row is the ΣDet result for the nodal ($\boldsymbol{k} = (\pi, 0)$) and antinodal ($\boldsymbol{k} = (\pi/2, \pi/2)$ self-energy $\Sigma(\boldsymbol{k}, i\omega_n)$ for different temperatures. The three characteristic regimes can be identified: for $T \gtrsim 0.3$ the imaginary part of self-energy has a positive slope and the system

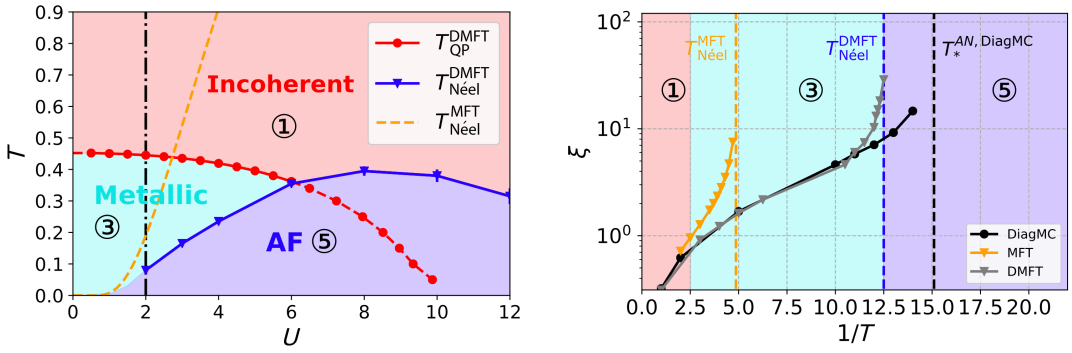

Figure 16: Left panel: Phase diagram obtained by single-site dynamical mean-field calculations. The red region is an incoherent state. At lower temperatures and $U \lesssim 5t$, a metallic state (cyan region) with coherent quasiparticle appears. At larger couplings (or low temperatures) there is a second-order phase transition to a antiferromagnetic insulator (blue area). Right panel: Correlation length at $U = 2t$ as a function of the temperature T as obtained from static mean-field theory (yellow), DMFT (gray) and DiagMC (black). Both static mean-field and DMFT see a divergence at a finite Néel temperature. Taken from Ref. [34].

---

is in its incoherent regime. For $0.1t \lesssim T \lesssim 0.3t$, coherent quasiparticles exist and the self-energy has a negative slope. Below $T \simeq 0.1$, the low-frequency part of $\Sigma(\boldsymbol{k}, i\omega_n)$ starts to display a kink with positive slope, marking the formation of a pseudogap in the spectral function.

The DMFT self-energy is shown in the second row of Fig. 17. Because of the local approximation of DMFT, $\Sigma(\boldsymbol{k}, i\omega_n)$ has no $\boldsymbol{k}$-dependence. It compares fairly well to the ΣDet results down to $T \simeq 0.3t$, especially at the node, but then starts to depart from the benchmark. This temperature is about the temperature where the magnetic correlation length starts to exceed one lattice site (see Fig. 16) and it makes sense that this is where spatial correlations beyond DMFT need to be taken into account. Note that an inspection of the local part of the self-energy shows that it compares well to the ΣDet solution down to $T \simeq 0.1t$ (see Fig. 5 of Ref. [34]). Below $T \simeq 0.08t$, the DMFT solution is magnetically ordered with a gap corresponding to a Slater mechanism. The gap is opened via a non-zero real part of the self-energy that effectively creates a band insulator at low energies. The imaginary part of the DMFT self-energy continues to be regular even at these low temperatures. In the true solution, the spin symmetry cannot be broken and the real part has to vanish for all temperatures $T > 0$ because of particle-hole symmetry. The opening of a pseudogap in the spectral function then necessarily has to come from a more singular behavior of the imaginary part of $\Sigma(\boldsymbol{k}, i\omega_n)$. This singular behavior is clearly seen on Fig. 17 for temperatures below $T \simeq 0.06$.

4.4 Single-particle properties beyond mean-field theory

In this section, we analyze how the single-particle properties are modified when spatial fluctuations are included in different many-body techniques.

Cluster extension of DMFT These extensions of the dynamical mean-field theory include spatial fluctuations and momentum dependence in the self-energy by solving an auxiliary cluster of coupled impurities embedded in a bath. The precise expression of the self-consistency depends on the chosen extension (DCA or CDMFT), but in all cases, the scale over which spatial fluctuations are taken into account is basically set by the size of the impurity cluster. The self-energies obtained by DCA and CDMFT are shown and compared to the benchmark in Fig. 18. For both DCA and CDMFT, the

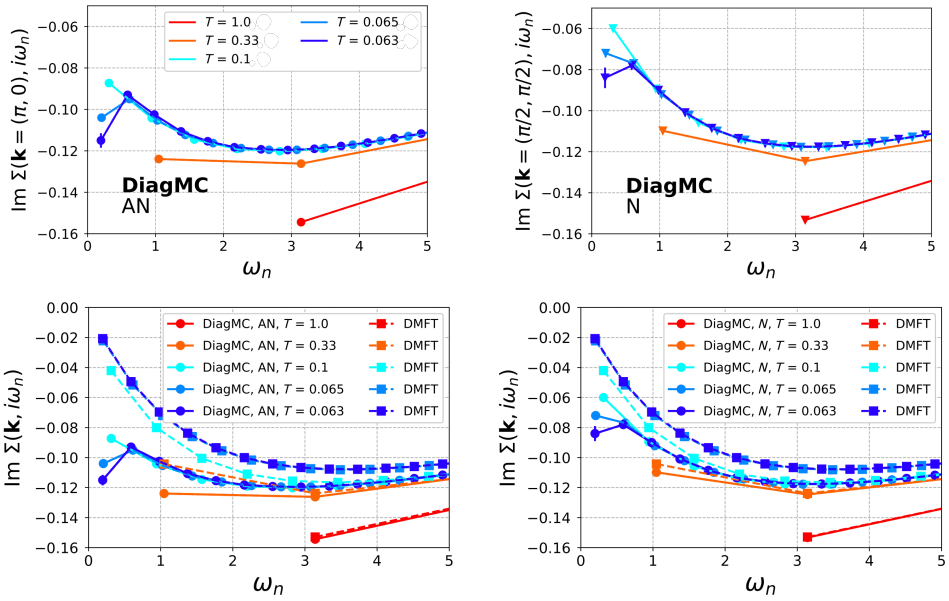

Figure 17: Top row: Imaginary part of the self-energy $\Sigma(\boldsymbol{k}, i\omega_n)$ at the antinode $\boldsymbol{k} = (\pi, 0)$ (left) and at the node $\boldsymbol{k} = (\pi/2, \pi/2)$ (right) as obtained by the ΣDet algorithm for different temperatures. Bottom row: Same as top row but with the DMFT self-energy displayed as well. Note that below $T \simeq 0.8t$, the DMFT solution is magnetically ordered. Taken from Ref. [34].

---

crossover from the incoherent state to the metallic state is well described and agrees quantitatively with the benchmark. When entering the metal, the self-energies start acquiring a momentum dependence that was absent in the single-site DMFT solution and nodal-antinodal differentiation is present for temperatures below $T \simeq 0.33$. The self-energies are in good quantitative agreement in the metallic regime down to $T \simeq 0.1t$. However, both methods are unable to open a pseudogap in the insulating-like regime and the corresponding self-energies remain regular at low frequencies down to the smallest temperature $T \simeq 0.06$. This is not very surprising. From Fig.16, it appears that the correlation length is $\xi \simeq 15$ in this temperature regime. The correlation length that can be captured with a cluster of N sites is about $\sqrt{N}/2$ and it would take a cluster of 1000 sites to correctly describe the spatial fluctuations at $T = 0.6$. This is currently out of reach for cluster methods. Cluster methods are actually more suitable for regimes where the correlation length is shorter, either at strong coupling or by doping the system away from half-filling.

Vertex-based extensions of DMFT Long-ranged spatial correlations may be more efficiently treated with diagrammatic extensions of DMFT, such as DΓA, TRILEX, DF or DB. The antinodal self-energies obtained by theses approaches are shown in Fig. 19. The incoherent to metallic crossover is again well described by all the methods, in very good quantitative agreement with the ΣDet benchmark. Except for the TRILEX, the diagrammatic extensions of DMFT also see the onset of a pseudogap at lower temperatures. The agreement with the benchmark is less quantitative though. The DF method seems to be performing best, while DΓA slightly overestimates the scattering rate, while DB seem to underestimate them.

Other approaches The self-energies of three other families of methods (TPSC/TPSC+, fRG and PA) are also displayed on Fig. 19. They all capture the crossover into a state with more coherent quasiparticles and momentum differentiation. The onset temperature of the insulating pseudogap regime is however quantitatively different from the benchmark. The TPSC approach, in its original

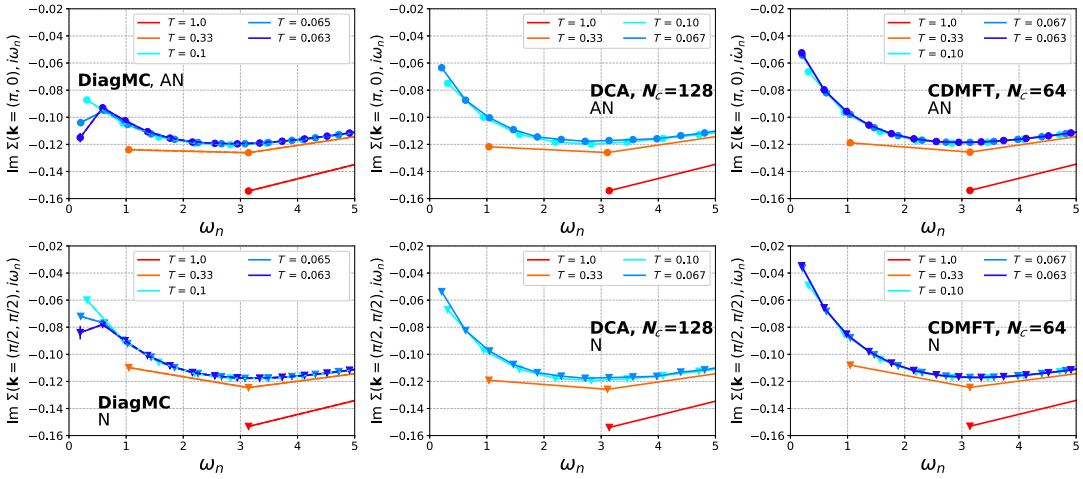

Figure 18: Imaginary part of the self-energy at the antinode (AN, top row) and at the node (N, bottom row) as obtained from the benchmark (left), DCA (middle) with 128 sites in the cluster and CDMFT (right) with 64 sites in the cluster. Taken from Ref. [34].

---

version, tends to overestimate this temperature because spin fluctuations are overestimated as well. A recent improvement of the method, TPSC+, that partially feeds back the self-energy into the fluctuation propagators, leads to results that are in much better agreement with the benchmark. The PA seems to eventually capture the insulating behavior at the antinode albeit at a lower temperatures $T < 0.05$ in comparison to DiagMC. The fRG calculations can be carried out only down to a temperature scale $T \simeq 0.07$ at which the running coupling constants diverge [137]. Down to this temperature, however, fRG is in qualitative agreement with the benchmark and shows a non-metallic behavior at the antinode.

4.5 Double occupancy and Pomeranchuk effect

The double occupancy is a very useful probe to examine the nature of the regimes of the Hubbard model. According to the used algorithm, it can either be measured directly, or obtained from the self-energy (and Green function) via the Galitskii-Migdal formula [138]

$$D = \frac{T}{U} \sum_{\boldsymbol{k},n} \Sigma(\boldsymbol{k}, i\omega_n) G(\boldsymbol{k}, i\omega_n). \tag{78}$$

The double occupancy results for several methods is displayed in Fig. 20. The benchmark result from DiagMC and DQMC is shown in black. Starting from high temperature, the double occupancy first decreases with decreasing temperature. It then reaches a minimum value at intermediate $T \simeq t$, grows again down to $T \simeq 0.1t$ and finally drops quickly when entering the pseudogap regime.

The high-temperature decrease of D upon cooling is easily explained by considering the expression of the double occupancy in an isolated Hubbard atom:

$$D_{\text{atomic}} = \frac{1}{2 + 2\exp(U/(2T))}. \tag{79}$$

The increase seen when cooling the system in the temperature range $0.1t \lesssim T \lesssim t$ is a manifestation of the Pomeranchuk effect, which has been documented very early in the half-filled Hubbard model [139]. Note that it takes place in a large part of the metallic regime. It can be understood from the Maxwell equation

$$\left.\frac{\partial D}{\partial T}\right|_U = -\left.\frac{\partial S}{\partial U}\right|_T. \tag{80}$$

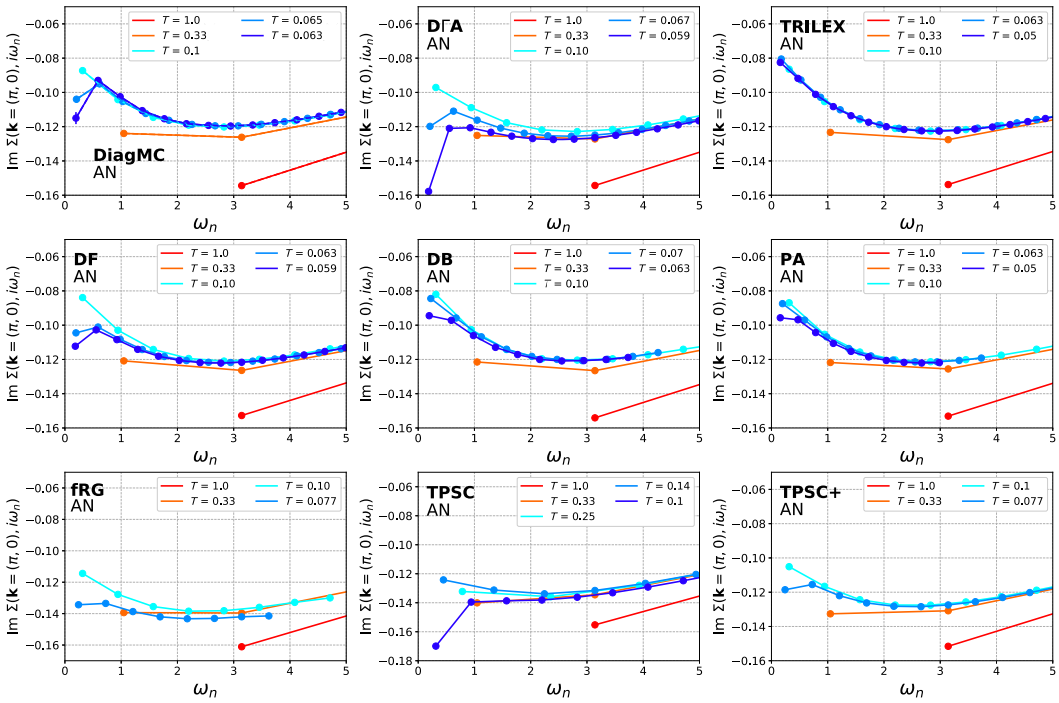

Figure 19: Imaginary part of the self-energy at the antinode as obtained from various many-body methods (see label). Taken from Ref. [34].

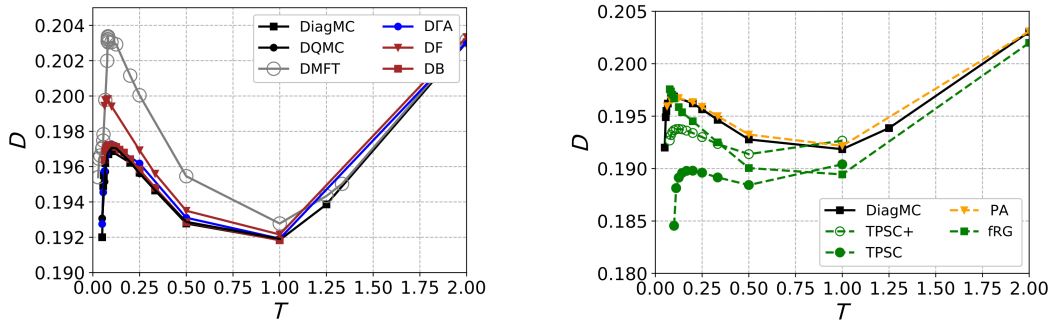

Figure 20: Double occupancy versus temperature as obtained from various many-body methods (see label). Adapted from Ref. [34].

In the metallic regime, an increase of the correlation U leads to a larger entropy (because of the increase of the effective mass with U which controls the slope of the linear entropy in the metal). As a result, the temperature derivative of D is negative. Eventually, D has a drop below $T \simeq 0.1t$ when long range magnetic correlations set in. This is because entering the Slater antiferromagnetic correlation regime is accompanied by a gain of potential energy because of the localization of the electrons in this insulating regime.

As shown in Fig. 20, DMFT is able to capture these different trends even though it overestimates the amplitude of the effect [140, 141]. The drop in the DMFT calculation is a consequence of the system entering an ordered phase, but as discussed earlier it happens at roughly the correct temperature.

All the many-body methods are able to capture the Pomeranchuk effect, but only those that form an insulating pseudogap state at low temperatures correctly describe the drop of D. Cluster extensions of DMFT and the TRILEX method therefore do not see the decrease of D upon cooling at low temperature. Vertex-based methods as well as TPSC/TPSC+ and PA all yield a drop. DΓA, DB and the PA are in remarkable agreement with the benchmark, while DF, TPSC/TPSC+ are qualitatively correct.

4.6 Magnetic correlations beyond mean-field theory

We next investigate the magnetic correlations of the two-dimensional half-filled Hubbard model in order to elucidate the role of spin fluctuations in establishing the low-temperature pseudogap insulator. Surprisingly, it will turn out that magnetic fluctuations are already present well above the pseudogap regime, in the metallic regime. We will discuss their origin and consequences below.

Antiferromagnetic spin susceptibility The first quantity that we inspect is the spin susceptibility $\chi_{\rm sp}(\boldsymbol{q}, i\Omega_n)$ given by

$$\chi_{\rm sp}(\boldsymbol{q}, i\Omega_n) = \int_0^\beta d\tau \sum_{\boldsymbol{r}} e^{i\tau\Omega_n} e^{-i\boldsymbol{q}\boldsymbol{r}} \langle S_z(\boldsymbol{r}, \tau) S_z(0, 0)\rangle \,, \tag{81}$$

where $\beta = 1/T$ and $S_z(\boldsymbol{r}, \tau) = n_\uparrow(\boldsymbol{r}, \tau) - n_\downarrow(\boldsymbol{r}, \tau)$. Note that we do not include the prefactor $1/2$ in our definition of S_z. Because of the perfect nesting of the Fermi surface, the spin susceptibility is always most enhanced at $\boldsymbol{q} = (\pi, \pi)$. The antiferromagnetic static susceptibility $\chi_{\rm sp}(\boldsymbol{q} = (\pi, \pi), i\Omega_n = 0)$ is shown in Fig. 21 for various methods. The benchmark result from CDet and DQMC is most visible on the top left panel (black line). At high temperature, the susceptibility essentially corresponds to that of a collection of independent fluctuating moments with a Curie law $\chi_{\rm sp}(\boldsymbol{q} = (\pi, \pi), i\Omega_n = 0) \sim T^{-1}$. At low temperatures $T \lesssim 0.07t$, when the pseudogap opens and the charge degrees of freedom start to be frozen, the susceptibility sees an exponential grow. The spin dynamics in this regime is expected to be described by a non-linear sigma model [132, 142–145] and the exponential growth is predicted in the lower critical dimension $d = 2$. It is more surprising that the behavior of the susceptibility between these two limits, in the metallic regime, seems to be exponential as well, albeit with a different exponent. It is quite counter-intuitive that lowering the temperature can lead to both more coherent quasiparticles and, at the same time, larger and longer-ranged spin fluctuations. We will discuss this point more in details below.

The susceptibilities obtained by dynamical mean-field theory and its cluster extensions are also shown on the top left panel. They are in good agreement at high temperatures but eventually depart from the benchmark and diverge at a finite Néel temperature, because the Mermin-Wagner

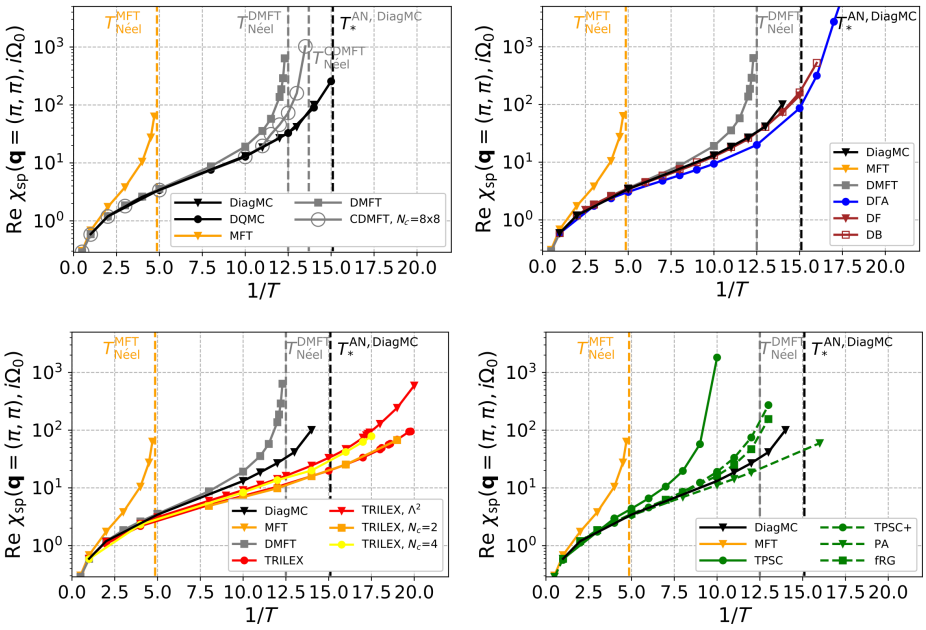

Figure 21: Antiferromagnetic static spin susceptibility $\chi_{sp}(\boldsymbol{q} = (\pi, \pi), i\Omega_n = 0)$ as a function of inverse temperature on a logarithmic scale obtained from various many-body methods (see labels). Adapted from Ref. [34].

---

theorem is not satisfied in these methods. The Néel temperature decreases with larger clusters and should eventually go to zero, but this decrease is logarithmically slow with system size [121, 146].

Vertex-based methods (top right panel) do respect the Mermin-Wagner theorem and do not have a divergent susceptibility. They all nicely capture the three different regimes of χ_{sp}. The DF and DB solutions are very close to the benchmark and can be computed down to temperatures slightly below the benchmark methods. The DΓA [112, 114, 122] slightly underestimated the spin susceptibility but can be converged down to lower temperatures. The TRILEX method (bottom left panel) also find the low temperature exponential scaling with some differences between different versions of the method.

Finally, the fRG and PA approaches correctly describe the high-temperature behavior and part of the metallic state. The fRG does not respect the Mermin-Wagner theorem and eventually overestimate the susceptibility. The PA method does not seem to be able to resolve the pseudogap region. The TPSC has the correct trends but overestimates spin fluctuations. This is partly corrected by the TPSC+ which is in good agreement with the benchmark down to $T \simeq 0.1t$ and then qualitatively describes the low-temperature exponential increase.

Magnetic correlation length The spatial extent of the magnetic correlations can be obtained by extracting the correlation length ξ from the susceptibility $\chi_{sp}(\boldsymbol{q}, i\Omega_n)$, assuming it has an Ornstein-Zernike form [147] close to its maximum at $\boldsymbol{Q} = (\pi, \pi)$

$$\chi_{sp}(\boldsymbol{q}, i\Omega_n = 0) \simeq \frac{A}{(\boldsymbol{q} - \boldsymbol{Q})^2 + \xi^2}. \tag{82}$$

The susceptibilities computed by the different methods are generally very well fitted by the Ornstein-Zernike form above. The resulting correlation length ξ is shown in Fig. 22. The qualitative behavior of ξ is very similar to $\chi_{sp}(\boldsymbol{Q}, i\Omega_n = 0)$ discussed above. In particular, the three regimes are clearly visible in the benchmark data. Especially, the correlation length has a clear exponential scaling in

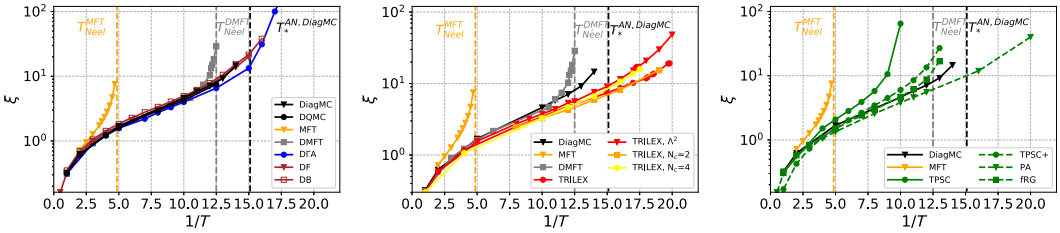

Figure 22: Magnetic correlation length ξ extracted from the magnetic susceptibility as a function of inverse temperature on a logarithmic scale obtained from various many-body methods (see labels). Taken from Ref. [34].

---

the metallic regime for $0.08t \lesssim T \lesssim 0.2t$. The second exponential regime in the insulating-like region just starts to be visible in the CDet calculations. It is more apparent in the DΓA results that can be carried out down to lower temperatures. As for the susceptibility, the vertex-based extensions of DMFT all shown the three regimes, as well as TPSC/TPSC+.

In summary, the magnetic correlations go through three regimes as temperature is lowered. Down to $T \simeq 0.2t$ they follow a Curie mean-field behavior with correlation lengths that do not exceed $\xi \simeq 2$. At intermediate temperatures, mostly in the metallic regime $0.08t \lesssim T \lesssim 0.2t$, the magnetic correlations increase exponentially with inverse temperature reaching correlation lengths as large as $\xi \simeq 10$ in a regime where coherent quasiparticles are still seen, at least at the node. In the pseudogap quasi-ordered low temperature regime $T \lesssim 0.08t$, the susceptibility and correlation length acquire another exponential growth which is associated to the freezing of the charge degrees of freedom.

4.7 Nature and consequences of spin fluctuations

In this section, we discuss in more details how spin fluctuations affect the physics in the different regimes described above. In particular, we analyze the mechanisms that open the low-temperature pseudogap. We also examine the effect of the exponentially growing magnetic correlations on the coherence and nature of the quasiparticles in the metallic regime.

Spin-fluctuation theory to the test The simplest version of spin-fluctuation theory expresses the self-energy as the result of a coupling between the electrons and a spin collective mode described by the susceptibility

$$\Sigma_{\rm SF}(\boldsymbol{k}, i\omega_n) = g^2 T \int \frac{d^2\boldsymbol{q}}{(2\pi)^2} \sum_m G_0(\boldsymbol{k}+\boldsymbol{q}, i\omega_n + i\Omega_m)\, \chi_{\rm sp}(\boldsymbol{q}, i\Omega_m), \tag{83}$$

where G_0 is the non-interacting electronic propagator, $\chi_{\rm sp}$ is the spin susceptibility and g is a coupling constant that quantifies the strength of the coupling. In order to gauge whether (83) can be used as a starting point to analyze the role of magnetic correlations, we compare it directly with self-energies obtained by DΓA at the antinode $(\pi, 0)$ in Fig. 23. We therefore compute (83) using the $\chi_{\rm sp}$ obtained by DΓA and, for simplicity, we choose $g^2 = 3U^2/8$. Note that other choices can be made. For example, in TPSC the choice $g^2 = 3U^2\langle n_\uparrow n_\downarrow\rangle / 8\langle n_\uparrow\rangle\langle n_\downarrow\rangle$ ensures both rotational invariance and that the Galitskii-Migdal equation is satisfied [148].

It appears that the spin-fluctuation expression (83) is in very good agreement with DΓA at high temperatures and in good qualitative agreement in the metallic and insulating regimes where it

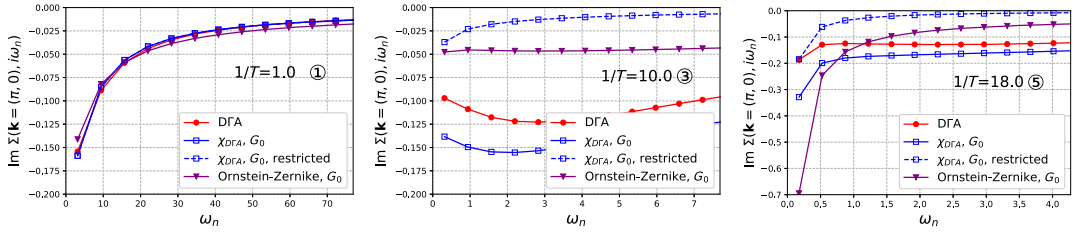

Figure 23: Self-energy obtained by spin-fluctuation theory compared with DΓA results in three regimes: the incoherent high-temperature regime (left), the metallic state (middle) and the low-temperature pseudogap insulator (right). Different versions of the spin-fluctuation formula are considered (see labels). Taken from Ref. [34].

---

slightly overestimates the self-energy. We can further ask whether the momentum integral in (83) is dominated by momenta near $\boldsymbol{Q} = (\pi, \pi)$. The dashed curves in Fig. 23 are obtained by restricting the integration over momenta such that $|q_i - Q_i| < 2\xi^{-1}$, $i \in \{x, y\}$. At high temperature and in the pseudogap insulator, this restriction does not lead to qualitative changes and spin fluctuations are dominated by the Brillouin zone area close to the antiferromagnetic wave vector. In the metallic regime, however, results change qualitatively and the self-energy obtained from the restricted integral does not have a metallic behavior. In the metallic regime, including spin fluctuation from all wave vectors is essential. We also examine if the DΓA susceptibility can be replaced in (83) by an Ornstein-Zernike fit of the form

$$\chi_{\rm sp}(\boldsymbol{q}, i\Omega_n) = \frac{A}{(\boldsymbol{q} - \boldsymbol{Q})^2 + \xi^{-2} + \frac{|\Omega_n|}{\gamma}}, \tag{84}$$

where γ is a Landau damping coefficient. The resulting violet curve on Fig. 23 is in very good agreement at high temperatures. In the pseudogap low-temperature regime, it is qualitatively similar to the DΓA result but overestimates the self-energy. Not surprisingly, it also yields a qualitatively wrong result in the metallic region, again because it only considers momenta centered around $\boldsymbol{Q} = (\pi, \pi)$.

Pseudogap insulating regime The self-energy in the pseudogap insulating regime is qualitatively well described by the spin-fluctuation expression (83) with the susceptibility $\chi_{\rm sp}$ taking an Ornstein-Zernike form (84). This allows for a deeper analytical understanding of this regime, see Refs [132, 145]. In particular, the pseudogap at a momentum $\boldsymbol{k}_F$ on the Fermi surface (that we suppose different from the antinode) appears in the renormalized classical regime [132, 149] where the temperature satisfies the condition $\pi T \gg \omega_c$ and ω_c is an important low energy scale defined by

$$\omega_c = \frac{v_F}{\xi} = \frac{v_F}{\xi_0} e^{-2\pi\rho_s/T}. \tag{85}$$

Above, v_F is the Fermi velocity at $\boldsymbol{k}_F$ and we have assumed an exponential growth of the correlation length at low temperatures, with ρ_s being the spin stiffness of the system. The condition $\pi T \gg \omega_c$ can be rewritten as $\xi \gg v_F/\pi T$ which means that the renormalized classical regime corresponds to the regime where the correlation length is much larger than the thermal de Broglie wavelength, i.e. the maximum distance over which an electron wave packet remains coherent despite thermal agitation [132]. The system can be seen as if it were ordered over the scale where coherence is not destroyed by thermal fluctuations. In this regime, only the first Matsubara frequency contributes to (83) and we find

$$\mathrm{Im}\Sigma(\boldsymbol{k}_F, i\omega_n) = -\tilde{g}\frac{T}{\sqrt{\omega_n^2 - \omega_c^2}} \ln \frac{\omega_n + \sqrt{\omega_n^2 - \omega_c^2}}{\omega_n - \sqrt{\omega_n^2 - \omega_c^2}}, \tag{86}$$

where prefactors have been gathered into $\tilde{g}$. When $\omega_n \gg \omega_c$, which is the case in the pseudogap insulator, we find that

$$\mathrm{Im}\Sigma(\boldsymbol{k}_F, i\omega_n) \sim -2\tilde{g}T\frac{1}{\omega_n}\ln\frac{\omega_n}{\omega_c}. \tag{87}$$

We recognize a negative divergent behavior in the self-energy of the pseudogap insulating regime. This self-energy yields a spectral function $A(\boldsymbol{k},\omega) = -\mathrm{Im}[\omega+\mu-\epsilon_{\boldsymbol{k}}-\Sigma]/\pi$ that displays a pseudogap between two peaks separated by a distance $4\sqrt{\pi\tilde{g}\rho_s}$. The widths of the peaks [144, 145, 150] are of order $(\tilde{g}T^2/\rho_s)^{1/2}$. As temperature goes to $T=0$, the peaks evolve into the ground-state insulating gap due to the long-range antiferromagnetic order. Note that the analysis above is not valid for a momentum taken at the van Hove singularity $\boldsymbol{k}=(\pi,\pi)$. In that case, the self-energy is even more singular as discussed in Sec. VII.B. of Ref. [34].

Metallic regime The metallic region in Fig. 15 has been identified as the region where the slope of the imaginary part of the self-energy is negative. A closer inspection of the quantities

$$Z_{\boldsymbol{k}} = \left[1-\frac{\partial \mathrm{Im}\Sigma(\boldsymbol{k},i\omega_)}{\partial\omega}\bigg|_{\omega\to 0}\right]^{-1} \qquad \gamma_{\boldsymbol{k}} = \tau_{\boldsymbol{k}}^{-1} = -Z_{\boldsymbol{k}}\,\mathrm{Im}\Sigma(\boldsymbol{k},i\omega)\Big|_{\omega\to 0} \tag{88}$$

shows that the metallic phase is actually divided into two subregions. In a Fermi liquid, $Z_{\boldsymbol{k}}$ would correspond to the quasiparticle spectral weight and $\gamma_{\boldsymbol{k}}$ to the inverse of the quasiparticle lifetime. Because of the nesting property of the Fermi surface, the metallic regime is a non-Fermi-liquid (see discussion in Sec. VII.C. of Ref. [34] for details), but $Z_{\boldsymbol{k}}$ and $\gamma_{\boldsymbol{k}}$ still give some intuition about the behavior of the quasiparticles. In particular, $Z_{\boldsymbol{k}}$ and $\gamma_{\boldsymbol{k}}$ both decrease upon cooling over most of the metallic region, see cyan area in Fig. 24. This is the expected behavior for a conventional metal. But below $T\simeq 0.1t$ and still above the pseudogap formation temperature, $Z_{\boldsymbol{k}}$ and γ_k start increasing. This change of behavior can be understood by expressing the zero-frequency scattering rate in terms of the spectral representation of χ_{sp}

$$-\mathrm{Im}\Sigma(\boldsymbol{k},i0^+) \sim g^2\int d^2q\int d\omega\frac{1}{\sinh(\beta\omega)}\mathrm{Im}\chi_{\mathrm{sp}}(\boldsymbol{q},\omega)\delta(\omega-\epsilon_{\boldsymbol{k}+\boldsymbol{q}}). \tag{89}$$

The width in frequency of $1/\sinh(\beta\omega)$ is of the order of the temperature T, while $\mathrm{Im}\chi_{\mathrm{sp}}$ has a typical extent set by the Landau damping γ and peaks at at the characteristic spin-fluctuation frequency

$$\omega_{\mathrm{sf}} = \gamma\xi^{-2} \tag{90}$$

as can be seen from expression (84). As a result, when $T \lesssim \omega_{\mathrm{sf}}$, only the low-frequency part of $\mathrm{Im}\chi_{\mathrm{sf}}$ matters and the prominent peak in $\mathrm{Im}\chi_{\mathrm{sf}}$ is filtered away. The contribution to the scattering rate in this regime is therefore small and does not prevent the formation of quasiparticles. Note that ω_{sf} is a function of temperature so that the condition $T \lesssim \omega_{\mathrm{sf}}$ characterizes the metallic region above $T\simeq 0.1t$. Instead, when $T \gtrsim \omega_{\mathrm{sf}}$, the peak of the susceptibility does contribute to the scattering rate and leads to a rapid decrease of the quasiparticle lifetime with increasing antiferromagnetic spin fluctuations. This is the region $T \lesssim 0.1t$. In summary, the two low-energy scales ω_c and ω_{sf} eventually define three low-temperature regions:

1. $T \gtrsim \omega_c \Leftrightarrow T \lesssim 0.06t$: The pseudogap insulating regime, where the spin fluctuations close to $\boldsymbol{Q}=(\pi,\pi)$ dominate the scattering. The Ornstein-Zernike form provides a good approximation in this renormalized classical regime.

2. $\omega_{\mathrm{sf}} \lesssim T \lesssim \omega_c \Leftrightarrow 0.06t \lesssim T \lesssim 0.1t$: The low-temperature metallic regime where a precursor pseudogap starts opening. The scattering rate is non-metallic and increases upon cooling. The spin fluctuations close to $\boldsymbol{Q}=(\pi,\pi)$ represent an important fraction of the scattering rate which increases when the magnetic correlation length and the spin susceptibility increase.

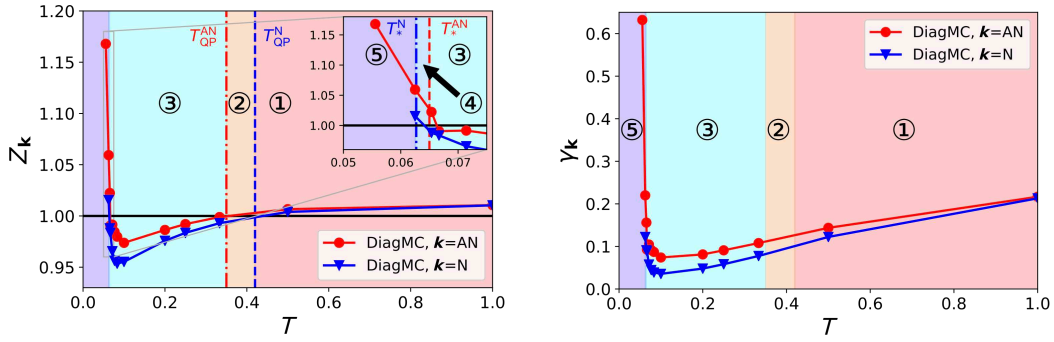

Figure 24: Quasiparticle parameters Z_k (left) and γ_k (right) at the antinode (red) and node (blue) for the ΣDet benchmark as a function of the temperature T. Region ① is the incoherent regime, ③ the metallic regime, ⑤ the pseudogap insulating regime. ② and ④ are nodal/antinodal differentiated regions. Taken from Ref. [34].

---

3. $T \lesssim \omega_{sf} \Leftrightarrow T \gtrsim 0.1t$: The more conventional metallic regime. All wave vectors of the spin fluctuations need to be taken into account in order to properly describe the scattering rate. A direct inspection of χ_{sp} shows that the Ornstein-Zernike misses an important part of the spectral weight away from $\boldsymbol{Q} = (\pi, \pi)$. The contribution from wave vectors close to (π, π) can be shown to be proportional to $g^2(A/\gamma)T^2\xi^3$. The increase of the correlation length ξ is balanced by a rapid decrease of the (A/γ) term via the increasing Landau damping and prevents the destruction of coherent quasiparticles. This is how in the metallic regime, both long-range magnetic correlations that grow exponentially and coherent quasiparticles can coexist.

4.8 Conclusion

The two-dimensional Hubbard model at half-filling has been studied in details at weak coupling with a special focus on the different regimes appearing at $U = 2t$ as a function of temperature. Despite its apparent simplicity for this low coupling value, the model displays very rich physics and is still very challenging for state-of-the art computational methods, especially in its low-temperature regime. It has therefore been an ideal testbed for a comprehensive comparison of different many-body techniques. In this context, the modern versions of DiagMC, CDet and ΣDet, together with DQMC have provided unbiased benchmark results. Through a systematic analysis of one- and two-particle observables, we have precisely characterized the regimes with particular attention on the nature and role of the spin fluctuations. At high temperatures, the system is incoherent. It gradually turns into a metal with coherent quasiparticles upon cooling. All the many-body methods are able to quantitatively describe this first crossover. As temperature is further lowered in the metallic regime, the magnetic correlation length increases exponentially and cluster extensions of DMFT depart from the benchmark result because they cannot treat impurity cluster sizes that are large enough. Even though the magnetic correlation length is very large, we have shown that the scattering rate is determined by spin fluctuations from all wave vectors, not just those close to $\boldsymbol{Q} = (\pi, \pi)$ and, as a result, long-range magnetic correlations can coexist with well defined quasiparticles. At lower temperature, the pseudogap insulating regime is reached with a further exponential increase of the correlation length. All methods eventually break down, even if diagrammatic extensions of DMFT are in good semi-quantitative agreement with the benchmark down into the pseudogap regime. Finally, TPSC/TPSC+, fRG and PA capture the correct qualitative physics but are not always in good quantitative agreement.

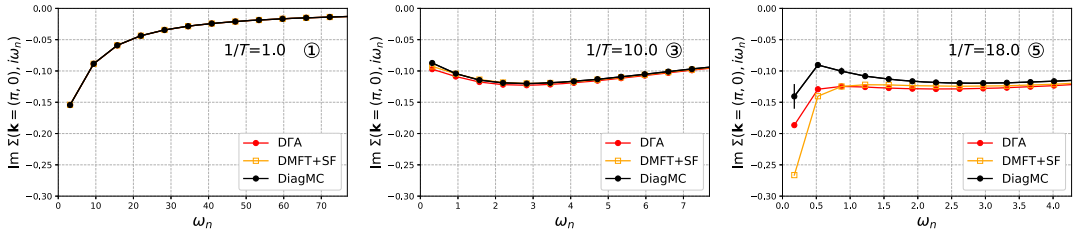

Figure 25: Imaginary part of the self-energy obtained from the combination of DMFT with spin-fluctuation theory in three different temperature regimes: high-temperature incoherent (left), metallic (middle) and pseudogap insulating (right). Results from DiagMC and DΓA are shown for comparison. Taken from Ref. [34].

Having benchmark results available makes it possible to explore new approaches and determine their level of accuracy. One of the outcomes of our study is that while DMFT does not capture spatial fluctuations, it still does a very good job at evaluating local observables, even at a quantitative level in the metallic regime where the magnetic correlation length is already large. This has motivated a simple approximation where the self-energy is taken as the sum of the local DMFT self-energy supplemented by the non-local part of the spin-fluctuation (83):

$$\Sigma(\boldsymbol{k}, i\omega_n) \simeq \Sigma_{\mathrm{DMFT}}(i\omega_n) + [\Sigma_{\mathrm{SF}}(\boldsymbol{k}, i\omega_n) - \Sigma^{\mathrm{loc}}_{\mathrm{SF}}(i\omega_n)], \tag{91}$$

where Σ_{SF} is computed with (83) using the DΓA approximation for χ_{sp}. Results for this approximation are shown in Fig. 25 in the three main regimes. They are in good quantitative agreement all the way down to the pseudogap opening where they still provide a qualitatively correct behavior. This is documenting that while the local physics needs a non-perturbative treatment, even at $U = 2t$, the non-local part can be treated perturbatively.

In the future, it would be very useful to carry out a similar analysis to analyze the strong coupling regime. This will however need to involve methodological developments as there are currently no many-body techniques that can provide a complete benchmark with full momentum resolution at larger values of U. It would be interesting to explore whether clever choices of renormalized propagators in an RDet approach would allow to reach larger couplings and circumvent the difficulties of the series resummations.

5 Unbiased calculations of the antiferromagnetic phase in the three-dimensional Hubbard model

One of the outstanding challenges in the physics of strongly correlated materials is to understand their phase diagrams, how different phases compete and what are the mechanisms that give rise to one phase or another. It is therefore desirable to have powerful tools and models to address these questions. The three-dimensional Hubbard model is maybe the simplest platform to investigate the potential of different computational approaches to study phase transitions in systems of correlated fermions. We will consider the simplest half-filled case, described by the Hamiltonian

$$\mathcal{H} = -t \sum_{\langle r,r'\rangle,\sigma} c^\dagger_{r\sigma} c_{r'\sigma} + U \sum_r n_{r\uparrow} n_{r\downarrow} - \frac{U}{2} \sum_{r,\sigma} n_{r\sigma}, \tag{92}$$

where t is a nearest-neighbor hopping amplitude on an $L \times L \times L$ cubic lattice, U is the local Coulomb interaction and we have set the chemical potential to $\mu = U/2$ in order to maintain the system at half-filling. Note that this model can be realized with cold atoms trapped in optical lattices [151] and experiments have been able to measure nearest-neighbor magnetic correlations [24, 152, 153] in cubic geometries. This provides further motivation to develop methods that can quantitatively compare with experiments.

5.1 Magnetic phase diagram and current limitations

The phase diagram at half-filling as a function of U and temperature is understood to a large extent. At zero temperature, antiferromagnetic order is stabilized for any value of $U > 0$. As temperature is increased, the order is eventually suppressed at the Néel temperature T_N and a paramagnetic state is stabilized [154]. The resulting dome-shaped area of antiferromagnetic order has a maximum at a value $U \sim 8t$, see Fig. 27. While this qualitative behavior is established, obtaining accurate numerical results close to the transition where the antiferromagnetic correlation length diverges is especially difficult, even at half-filling where quantum Monte Carlo methods generally do not suffer from a sign problem. For this reason, the finite temperature three-dimensional half-filled model has been investigated by many methods, including e.g. the two-particle self-consistent approach (TPSC) [155, 156], lattice quantum Monte Carlo methods [154, 157–160] or diagrammatic [122, 126, 161–164] and cluster extensions [46, 165–169] of the dynamical mean-field theory (DMFT) [43–45]. Except for single-site DMFT which does not capture spatial fluctuations, most of the studies have investigated the transition from above by computing susceptibilities in order to find an estimate for T_N and possibly the associated critical exponent. But the ordered phase itself has rarely been stabilized and studied in details. For methods that simulate a finite lattice, such as determinantal quantum Monte Carlo (DQMC) or determinant diagrammatic Monte Carlo (DDMC), there is a natural reason for this: A phase transition to an ordered state cannot occur and only susceptibilities of the normal state can be used to locate the phase transition. Extensions of DMFT can potentially be used inside ordered phases but, to our knowledge, such studies have not been conducted for the three-dimensional Hubbard model so far (the two-dimensional case has been addressed in e.g. Refs [141, 170]).

5.2 Broken-symmetry perturbation theory

We have used the generalization of the CDet algorithm to broken-symmetry perturbation series to compute physical properties directly inside the antiferromagnetic phase [105]. As discussed

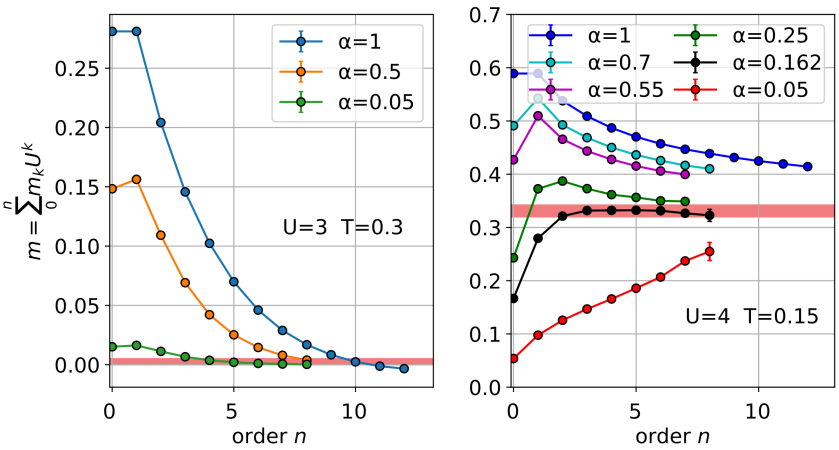

Figure 26: Partial sum for the magnetization for different choices of the external field $h = \alpha h_{\mathrm{MF}}$ in a case where the physical system is paramagnetic (left panel) and where it has antiferromagnetic order (right panel). Adapted from Ref. [105].

---

in Sec. 3.5, the idea of the method is to construct a perturbation theory starting from a non-interacting state placed in an external staggered magnetic field. The perturbation series is written in terms of a coupling ξ which defines both the strength of the local Coulomb interaction and of the external field acting on the system $(1 - \xi/U)h$. When $\xi = 0$ the external field is h and the non-interacting system already breaks the magnetic SU(2) symmetry. As ξ is increased, the external field gradually diminishes and eventually vanished at the physical value of interest $\xi = U$. At this value, the system described by the perturbation series is exactly the same as (92) and may or may not display antiferromagnetic order. In both events though, no symmetry is broken between the $\xi = 0$ state and the physical state at $\xi = U$ and one can hope that the underlying pole structure of the broken-symmetry perturbation series is well behaved so that it may be evaluated at $\xi = U$.

We have been able to consider systems that are large enough (most of the calculations where done for a $20 \times 20 \times 20$ lattice) that finite-size scaling was not necessary in order to extrapolate to the thermodynamic limit. The result at $\xi = U$ should not depend on the field strength h at $\xi = 0$. The parameter h can therefore be used to control the convergence of the series. In practice, optimal choices for h range between 0 and the effective field h_{MF} found in the antiferromagnetic mean-field solution of (92) at the physical interaction U. We therefore describe the choice of h with the scalar $\alpha \in [0, 1]$ such that $h = \alpha h_{\mathrm{MF}}$. An example of the effect of α on the convergence properties of the magnetization is shown in Fig. 26. In order to provide a confidence interval for our results, we use several resummation techniques (Padé, Dlog-Padé) for several values of α.

5.3 Magnetization and critical behavior

We start by analyzing the behavior of the magnetization close to the second-order phase transition at T_N. We compute the magnetization in two different complementary ways:

- We evaluate the magnetization by directly computing the average value $m = \langle n_{0\uparrow} \rangle - \langle n_{0\downarrow} \rangle$ within the CDet algorithm.
- We add an external staggered field H_{ext} to the Hamiltonian (92) that couples to S^z_r and compute the grand potential density Ω/L^3 with CDet. The magnetization is obtained from

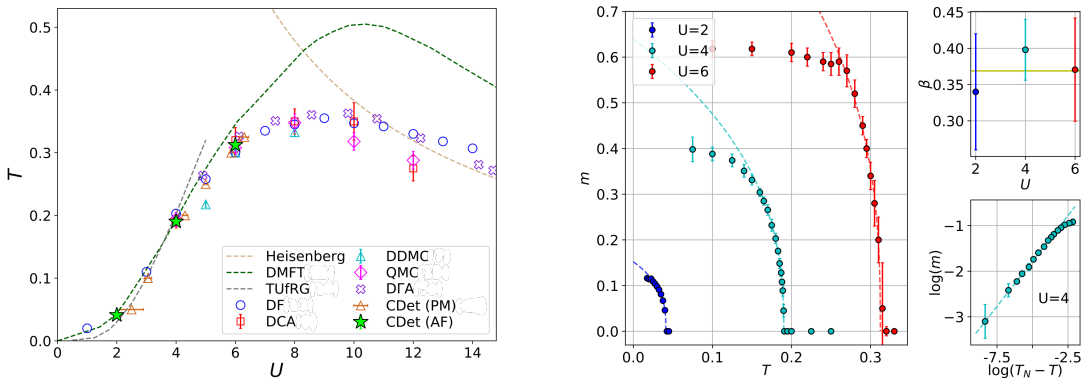

Figure 27: Left panel: Néel temperature for the three-dimensional Hubbard model at half-filling as obtained from different computational methods: DMFT [164], TUfRG [171], DF [164], DCA [165], DDMC [159], QMC [157], DΓA [163], CDet (PM) [160] and CDet (AF) (this work). Right panels: Magnetization m as a function of the temperature T for three values of the interaction U. The dashed curves are a fit of the form $a(T - T_N)^\beta$. The obtained values for T_N are displayed on the phase diagram on the left with green stars and the values of β are shown in the inset (the yellow line is the theoretical expectation for the $O(3)$ Heisenberg universality class). Adapted from Ref. [105].

---

several small fields by fitting the linear behavior of Ω

$$m = -\left.\frac{\partial \Omega}{L^3 \partial H_{\text{ext}}}\right|_{H_{\text{ext}}=0}, \tag{93}$$

The first approach is simpler to implement in practice, but the series for the magnetization become difficult to resum for $U > 6t$ at low temperatures. In this regime, the second method proves to be more efficient.

In Fig. 27, we display the magnetization as a function of temperature for different value of the interaction U. The obtained data is very accurate up to $U \sim 6t$. Above this value, we were not able to reliably resum the series close to the phase transition. The $m(T)$ curves all have the expected $(T - T_N)^\beta$ critical behavior close to the phase transition. This allows for a three parameter fit with a function $a(T - T_N)^\beta$ from which we can extract both the critical exponent β (see inset in Fig. 27) and the Néel temperature. We find $T_N(U = 2) = 0.0425(25)$, $T_N(U = 4) = 0.191(1)$ and $T_N(U = 6) = 0.315(5)$. These values are also shown on the phase diagram in Fig. 27 and compare well with other approaches. The found critical exponent is in very good agreement with the expected value $\beta = 0.3689(3)$ for the $O(3)$ Heisenberg universality class [172] as also found with other approaches such as dual fermions [164] or the dynamical vertex approximation [161, 173]. A novelty of the results is that they show the behavior of the magnetization inside the ordered phase. It is interesting to see that it reaches a saturation value quickly as temperature is decreased and even more so and larger value of U.

5.4 Double occupancy and entropy

More insight into the nature of the transition can be obtain by studying the behavior of the double occupancy $D = \langle n_\uparrow n_\downarrow \rangle$ across the transition. This is shown on the left panel of Fig. 28 for three different value of the coupling. The result at $U = 4t$ shows that, above the transition, the double occupancy decreases with increasing temperature. This is due to the Pomeranchuk effect discussed above in Sec. 4.5 for the two-dimensional case (see also Ref. [174]). The behavior of D below T_N is

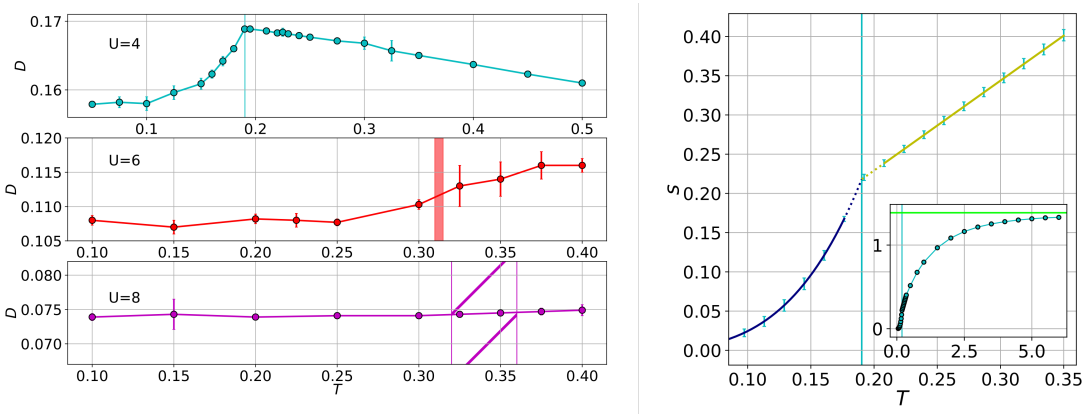

Figure 28: Left panel: Double occupancy $D = \langle n_\uparrow n_\downarrow \rangle$ as a function of the temperature T for three values of the Coulomb interaction U. Right panel: Entropy S as a function of the temperature T at $U = 4t$. The inset is the same plot over a larger temperature range and shows the high-temperature limit ln(4). Adapted from Ref. [105].

---

characteristic of a potential energy driven transition, with a rapid decrease as the antiferromagnetic order is stabilized. This is compatible with a Slater mechanism where the formation of an ordered state is accompanied by a localization of the electrons and a reduction of D. At the larger couplings $U = 6t$ and $U = 8t$ the double occupancy does not see a dramatic change across the transition. For those values of U, the system has not yet reached the Heisenberg regime where a kinetic energy driven transition is expected and would yield an increase of D as the temperature goes below T_N.

The right panel of Fig. 28 shows the entropy density S as a function of the temperature at $U = 4t$. The entropy is most easily computed from the temperature derivative of the grand potential

$$S = -\frac{\partial \Omega}{L^3 \partial T}. \tag{94}$$

In this regime, the entropy has a linear behavior almost immediately above T_N, showing that a good metallic state is realized. At very high temperatures, the entropy eventually saturates at the expected ln(4) value. At low temperatures below T_N, the entropy behaves as T^3, compatible with the T^3 scaling of the spin-wave contribution to the specific heat of an antiferromagnet [175]. Such measurements of the entropy can potentially be useful in connection with experiments on cold atoms, where entropy is the natural quantity to evaluate as it is conserved in closed traps.

5.5 Evolution inside the antiferromagnetic phase

We have measured the magnetization and double occupancy deeper into the antiferromagnetic dome. For the magnetization, it turned out to be more accurate to compute it from the derivative of the grand potential with respect to an external added field for value of $U > 6t$. The results are shown on Fig. 28 for several temperatures as a function of the interaction U. Interestingly, the series are easier to resum when the antiferromagnetic order in well established. We could reach values as large as $U = 18t$. The first observation is that both the double occupancy and the magnetization quickly reach a saturation value which almost does not change below $T = 0.2t$ above $U \simeq 5t$. The magnetization keeps on increasing at least until $U = 18t$. At any finite temperature, we expect it to eventually have a maximum, but at a larger value of U, well beyond the maximum of the dome at $U \simeq 8t$. The double occupancy has a first rapid decay when entering the magnetic dome and then regularly decreases. When the antiferromagnetism is prohibited, as can be done in dynamical mean-field calculations, there is a Mott transition at a critical value of U.

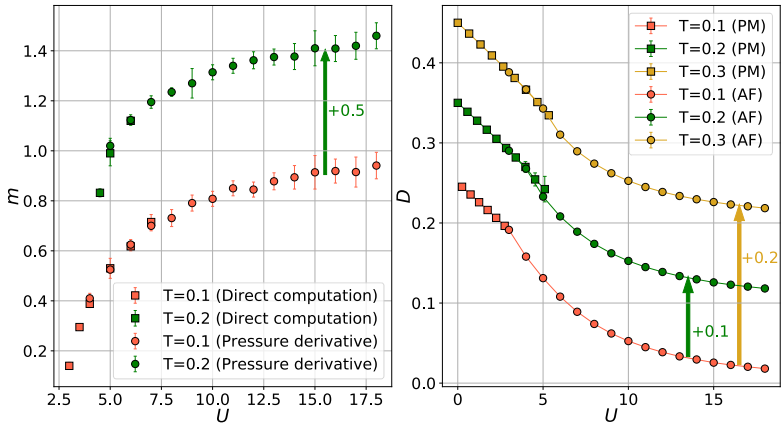

Figure 29: Physical properties inside the antiferromagnetic dome. Left panel: magnetization as a function of U for two temperatures. At small U, the magnetization is measured directly within CDet, while at larger values of U it is obtained via (93). Right panel: double occupancy as a function of U for three temperatures. Adapted from Ref. [105].

It is interesting to ask whether there are signatures of this transition when the antiferromagnetic order is established [176]. This question was addressed in Refs [141, 170] in two dimensions within a cellular dynamical mean-field approach. In our calculation, we however do not have access to the underlying normal state solution and can only measure the double occupancy of the ordered state. In the range of interactions that we could access, we are not able to see particular features in this quantity.

5.6 Conclusion

We have used the broken-symmetry perturbation series introduced in Sec. 3.5 to investigate the three-dimensional Hubbard model at half-filling. This approach is complementary to other methods as it is able to compute physical quantities in the ordered phase directly in the thermodynamic limit and no finite-size scaling analysis is necessary. We were able to compute the magnetization and double occupancy across the phase transition for values of $U < 6t$ in the weak-to-intermediate coupling regime. In the strong coupling regime, beyond the maximum of the antiferromagnetic dome, the series cannot be resummed reliably. It would be interesting to investigate whether a generalized RDet scheme would allow to reach larger values of the interaction U.

Inside the antiferromagnetic dome, the situation is more favorable and the magnetization and double occupancy can be computed to values of U as large as $U = 18t$. The double occupancy in the antiferromagnetic dome has a very smooth behavior as a function of U and does not provide striking insights into the nature of the weak to strong coupling crossover or the possible remnant of an underlying Mott transition that is observed in the normal state. Finding other observables that would be more expressive is an important next step.

A natural extension of this work is to go away from the half-filled case and investigate the incommensurate order and quantum criticality of the doped model. This would offer a complementary perspective to previous studies such as Refs [160, 173].

6 Doping the Hubbard model: magnetic and charge correlations and pseudogap

The two-dimensional Hubbard model that we have discussed at half-filling in Sec. 4 is a very rich platform to investigate the physics of strong correlations. It very much plays the role that the Ising model [13, 14] does in statistical physics but in the quantum many-body context. Its relevance goes well beyond that of a simple playground model and, even if it is not fully realistic at the microscopic level, features many important phenomena observed in a broad range of materials [19, 20]. In particular, in its hole-doped regime, it is often conjectured to be the minimal model capturing the main characteristics of high-temperature cuprate superconductors [5, 177]. The latter are a good example of how correlations can give rise to intricate physical properties. At low temperature, besides superconductivity, experiments find a rich diversity of phases with different kinds of intertwined long-range order, most notably charge density waves [10]. At larger temperature, the metallic non-superconducting "normal" state is highly unconventional with a partially destroyed Fermi surface resulting from the depletion of the number of electronic excitations and the formation of a pseudogap [6].

Understanding the relationship between these different effects with the help of the Hubbard model has proven to be a formidable challenge. While great progress has been achieved, including through collaborative efforts [30–32, 34], a consensus phase diagram for the Hubbard model is still missing [35, 36] and fundamental questions remain. Does the two-dimensional Hubbard model host superconductivity in some regimes of parameter? Is the pseudogap state a new kind of metallic state that could in principle be stabilized down to zero temperature, or is it a finite-temperature intermediate state which is always unstable to various kinds of long-range ordering? In that respect, what is the relationship between the strength of magnetic and charge correlations, their spatial extent and the onset of the pseudogap?

Many different computational techniques have addressed these questions and some regimes, as e.g. the half-filled case discussed in Sec. 4, are well understood. Away from half-filling at stronger coupling, which is the relevant regime for cuprate superconductors, the picture becomes more blurry and a dichotomy largely exists among computational studies. Wave-function based methods such as the density-matrix renormalization group (DMRG) [31, 178–180], variational Monte Carlo (VMC) [181], auxiliary field quantum Monte Carlo (AFQMC) [31, 182, 183], the density matrix embedding theory (DMET) [31, 184, 185] or inhomogeneous dynamical mean-field theory (iDMFT) [186–188] have addressed the nature of the ground state and demonstrated (when only nearest-neighbor hoppings are considered) that it is characterized by spin and charge ordering forming stripe patterns at low doping levels as proposed early on in the context of mean-field studies [189–192]. On the other hand, methods aimed at non-zero temperatures, mainly based on cluster extensions of the dynamical mean-field theory, have revealed that the Hubbard model hosts a pseudogap regime associated with magnetic correlations [46, 193–201]. The nature of the magnetic and charge correlations have also been studied with DMFT [202], iDMFT [203], determinant Quantum Monte Carlo (DQMC) [179, 204], the dynamical cluster approximation (DCA) [205], AFQMC [206] and the minimally entangled typical thermal states (METTS) [207]. However, the precise relation between magnetic and charge correlations and the pseudogap has not been carefully investigated. Answering crucial questions, such as the fate of the pseudogap state as temperature is lowered and how it connects to ground states with long-range order therefore calls for a "handshake" between different families of established computational methods and the development of new ones.

Our works in Refs [80, 208] are a first step in this direction. Using diagrammatic Monte Carlo, we obtain unbiased results for a broad range of parameters, including regimes with strong correlations displaying a pseudogap. At the same time, we also discuss the nature, strength and extent of

magnetic and charge correlations. Piecing together our results and those obtained in the ground state (mainly by Ref. [183]), we attempt to provide some answers to the questions above.

6.1 Model and physical observables

In the following, we consider the doped unfrustrated two-dimensional Hubbard model on a square lattice

$$\mathcal{H} = -t \sum_{\langle \boldsymbol{r},\boldsymbol{r}'\rangle,\sigma} t_{\boldsymbol{r}\boldsymbol{r}'} c^{\dagger}_{\boldsymbol{r}\sigma} c_{\boldsymbol{r}'\sigma} + U \sum_{\boldsymbol{r}} n_{\boldsymbol{r}\uparrow} n_{\boldsymbol{r}\downarrow} - \mu \sum_{\boldsymbol{r},\sigma} n_{\boldsymbol{r}\sigma}, \tag{95}$$

where the hopping amplitude t is only between nearest neighbors, U is the Coulomb repulsion and μ the chemical potential. The non-interacting dispersion relation is given by $\epsilon_{\boldsymbol{k}} = -2t(\cos(k_x) + \cos(k_y))$. Note that we do not consider next-nearest neighbor hoppings, $t' = 0$. We use the diagrammatic Monte Carlo algorithms described in Sec. 3 to compute physical observables on a square $L \times L$ lattice. For our simulations, we used $L = 64$ as we found it to be sufficient to eliminate finite-size effects. Note that there is in principle no technical limitations in considering larger systems. We investigated the temperature range $0.07t \leq T \leq 0.25t$ and coupling strengths up to $U = 8.5t$ for doping levels $\delta = 1 - \langle n_\uparrow + n_\downarrow \rangle$ going from half-filling ($\delta = 0$) up to 20% hole doping ($\delta = 0.2$).

Spin and charge susceptibilities In order to probe the spin and charge correlations, we use the momentum-resolved spin susceptibility (in real and reciprocal space), which provides a quantitative measure of magnetic ordering tendencies, and the momentum-resolved charge susceptibility, which characterizes the response of the system to an inhomogeneous density perturbation. The spin susceptibility in real space is

$$\chi_{\mathrm{sp}}(\boldsymbol{r}) = \int_0^{1/T} d\tau \, \langle S_z(\boldsymbol{r},\tau)\, S_z(\boldsymbol{0},0)\rangle, \tag{96}$$

where $S_z(\boldsymbol{r}) = \frac{1}{2}\left(n_{\boldsymbol{r}\uparrow} - n_{\boldsymbol{r}\downarrow}\right)$ is the z-component of the spin operator. Because the spin susceptibilities often peak close to the antiferromagnetic wave vector $\boldsymbol{Q} = (\pi,\pi)$, it is useful to also consider the staggered spin susceptibility $\chi^{\mathrm{st}}_{\mathrm{sp}}(\boldsymbol{r}) = (-1)^{x+y}\chi_{\mathrm{sp}}(\boldsymbol{r})$ which emphasizes the incommensurate behavior of the susceptibility. The Fourier transform of $\chi_{\mathrm{sp}}(\boldsymbol{r})$, $\chi_{\mathrm{sp}}(\boldsymbol{q})$, would diverge at the onset of long-range magnetic order of wave vector $\boldsymbol{q}$. Similarly, the charge susceptibility is defined by

$$\chi_{\mathrm{ch}}(\boldsymbol{r}) = \int_0^{1/T} d\tau \, \langle \delta n(\boldsymbol{r},\tau)\, \delta n(\boldsymbol{0},0)\rangle, \tag{97}$$

where $\delta n(\boldsymbol{r}) = \sum_\sigma n_{\boldsymbol{r}\sigma} - \langle n\rangle$, and $\langle n\rangle$ is the average number of particles per site $\langle n\rangle = \sum_\sigma \langle n_{\boldsymbol{r}\sigma}\rangle$. The Fourier transform of $\chi_{\mathrm{ch}}(\boldsymbol{r})$, $\chi_{\mathrm{ch}}(\boldsymbol{q})$, would diverges at the onset of long-range charge order of wave vector $\boldsymbol{q}$. In order to probe local correlations we also use the double occupancy

$$D = \langle n_{\boldsymbol{r}\uparrow}\, n_{\boldsymbol{r}\downarrow}\rangle, \tag{98}$$

which quantifies the formation of local moments. The entrance into the Mott-insulating regime can be characterized by an incompressible plateau in the density $\langle n\rangle$ as a function of the chemical potential μ. The spin and charge correlators were computed using the CDet algorithm with a mean-field chemical potential shift $\alpha = \alpha_{\mathrm{MF}} = \langle n_\sigma\rangle_0$, see Sec. 3.4.2. We also compared these results with those obtained by a modified version of the CDet algorithm that makes it possible to compute perturbation series at a fixed value of the interacting density $\langle n\rangle$, thank to a double expansion in both U and α (see Ref. [208] for details).

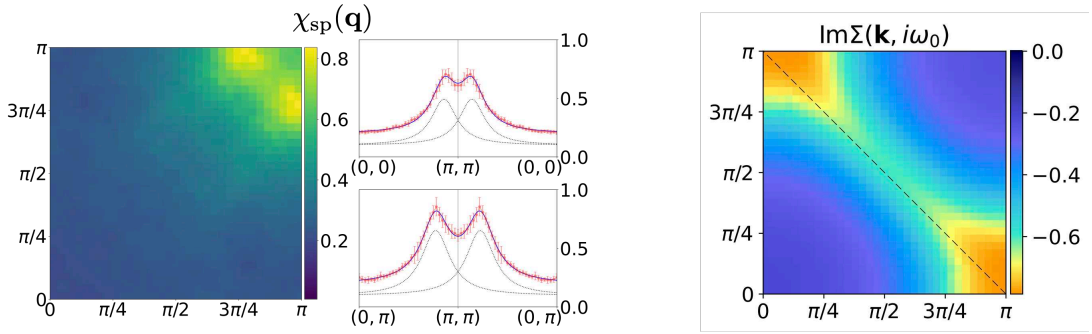

Figure 30: Typical results for one- and two-particle responses. Left panel: Momentum-space spin susceptibility $\chi_{sp}(\boldsymbol{q})$ for $U = 5t$, $T = 0.1t$ and $\langle n \rangle = 0.8$ over a quarter of the Brillouin zone (right). We also show a double-Lorentzian fit along the $\boldsymbol{q} = (Q, Q)$ (right top) and $\boldsymbol{q} = (Q, \pi)$ (right bottom) directions, where $Q \in [0, \pi]$. The solid blue line is the sum of the two dashed lines, which are Lorentzians. Right panel: Imaginary part of the self-energy $\Sigma(\boldsymbol{k}, i\omega_0)$ taken at the first Matsubara frequency over a quarter of the Brillouin zone. Parameters are $U = 4t, T = 0.2t$ and $\langle n \rangle \simeq 0.977$ Adapted from Refs [80, 208].

A typical result of a measured spin susceptibility is shown on the left panel of Fig. 30 for $U = 5t$, $T = 0.1t$ at 20% doping. In this example, the spin susceptibility has two incommensurate peaks close to (π, π). In order to extract the corresponding correlation length ξ, we fit these peaks using a double Lorentzian Ornstein-Zernike form with a constant offset

$$\chi_{sp}(\boldsymbol{q}) = A \left(\frac{1}{|\boldsymbol{q} - (Q_x, Q_y)|^2 + \xi^2} + \frac{1}{|\boldsymbol{q} - (Q_y, Q_x)|^2 + \xi^2} + \text{const} \right). \tag{99}$$

This procedure was also used e.g. in Refs [179, 205].

Self-energies and spectral functions The one-particle properties are obtained from the measurement of the self-energy $\Sigma(\boldsymbol{k}, i\omega_n)$ in reciprocal space and Matsubara frequencies. We use the ΣDet algorithm described in Sec. 3.2. With the self-energy, the Green function is found with the Dyson equation

$$G(\boldsymbol{k}, i\omega_n) = \left[G_0^{-1}(\boldsymbol{k}, i\omega_n) - \Sigma(\boldsymbol{k}, i\omega_n) \right]^{-1}. \tag{100}$$

Evaluating the Green function at the first Matsubara frequency gives a proxy $A(\boldsymbol{k})$ for the spectral function $A(\boldsymbol{k}, \omega = 0)$ at zero energy

$$A(\boldsymbol{k}, \omega = 0) \simeq A(\boldsymbol{k}) \equiv \mathrm{Im}G(\boldsymbol{k}, i\omega_0). \tag{101}$$

We sometimes find it useful to analyze the low-frequency behavior of the self-energy, to see whether it is more metallic-like or more insulating-like. To this effect, we compute the difference between the first two Matsubara frequency, which behaves like the slope

$$\Delta\mathrm{Im}\Sigma(\boldsymbol{k}) = \mathrm{Im}\Sigma(\boldsymbol{k}, i\omega_0) - \mathrm{Im}\Sigma(\boldsymbol{k}, i\omega_1). \tag{102}$$

$\Delta\mathrm{Im}\Sigma(\boldsymbol{k})$ is positive for a metallic-like self-energy and negative for an insulating-like self-energy.

6.2 Magnetic correlation regimes: the weak, the strong and the long

We start our discussion by a systematic analysis of the spin susceptibility $\chi_{sp}(\boldsymbol{q})$. It generally displays one or several peaks close to (π, π). In Sec. 6.3, we will discuss the commensurate-to-incommensurate crossover of the magnetic correlations. But here, we are first interested in the

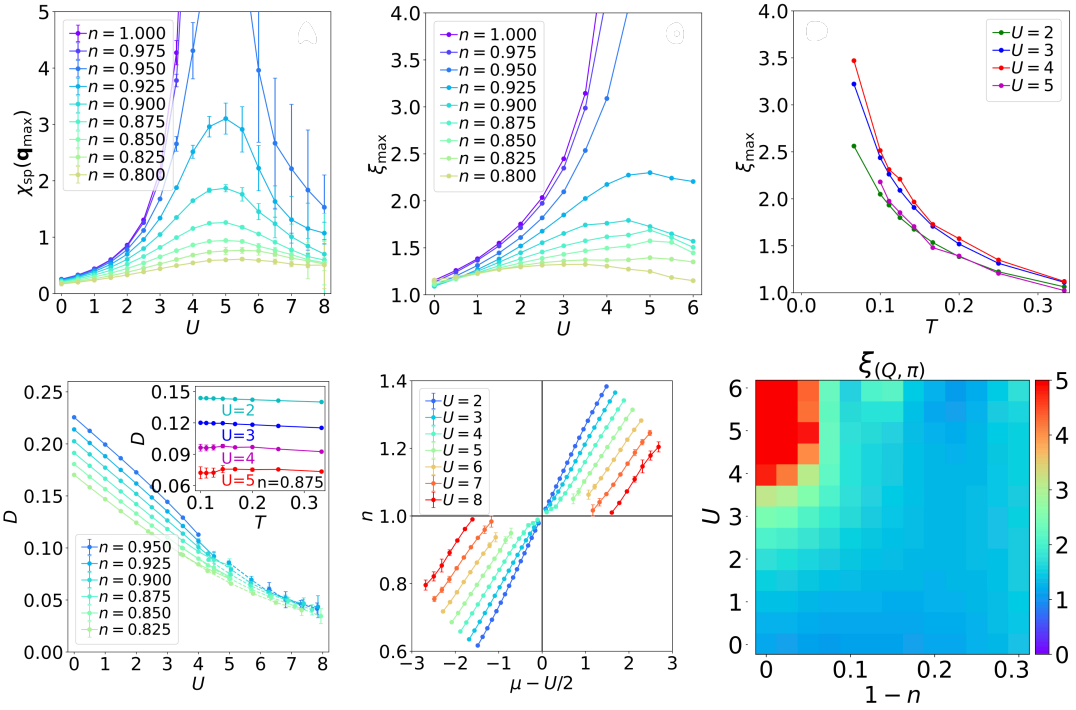

Figure 31: Top row: Maximum value of the spin susceptibility χ_{sp} over the Brillouin zone (left) for several doping levels. The associated correlation length ξ_{max} shown (middle) and evaluated for different temperatures (right). Bottom row: Double occupancy D as a function of U for several densities (left). The density versus chemical potential (middle) shows the development of a gap beyond $U \gtrsim 5t$. A diagram showing the correlation length as a function of U and doping. The temperature for the bottom row is always $T = 0.2t$. Adapted from Ref. [208].

---

typical strength and extent of the spin correlations and therefore focus on the value at its largest peak $\chi_{sp}(\boldsymbol{q}_{max})$ and use it to find the correlation length ξ_{max}, as discussed above. These results are shown on the first row of Fig. 31 and are complemented by double occupancy and density versus chemical potential data (second row). Together, these results show that there are three characteristic correlation regimes for the two-particle response of the system:

The weak-coupling regime For $U \lesssim 3t$ and $T \gtrsim 0.1t$, the system is in a weakly correlated regime. The double occupancy gradually decreases with increasing U and also decreases when the density goes away from half-filling, see the bottom left panel of Fig. 31 for $T = 0.2t$. The maximum value of the spin susceptibility and the associated correlation length slowly increase with U (two first panels on the top row). In this regime, the double occupancy decreases with increasing temperature (see inset in the double occupancy plot) because of the Pomeranchuk effect that we have already discussed in the half-filled case, Sec. 4.5. We observe this Pomeranchuk effect for all densities at least down to $n = 0.775$. Close to half-filling, we can observe a small change of slope in the density versus chemical potential curve (middle panel on the bottom row), indicating that the compressibility at half-filling is smaller than in the doped system.

The long correlation length regime When U is further increased, the maximal value of the spin susceptibility increases rapidly, even more so as one approaches half-filling, see Fig. 31. The weakly density-dependent position of the maximum for $T = 0.2t$ is around $U \simeq 4t - 5t$. In this intermediate coupling regime, the correlation length becomes large, especially close to half-filling

and as the temperature is lowered (see top right panel of Fig. 31). It decreases rapidly when the density is reduced and for $T \geq 0.1t$ it is only a couple of lattice sites long beyond 10% doping. The double occupancy as a function of U decreases more rapidly for densities close to half-filling, as a consequence of the larger correlation length, see bottom left panel. This is expected as the spins get more localized when ξ becomes large. The density versus chemical potential seem to indicate that there is a wider plateau but because of the long correlation length, it is difficult to obtain accurate results close to half-filling.

The strong local correlations regime For $U \gtrsim 6$ we enter a regime of strong correlations (at temperatures $T \sim 0.2t$). The double occupancy is only a fraction (about 25%) of its non-interacting value and becomes less dependent on the density. These (quasi) antiferromagnetic correlations are very local and the spin susceptibility and magnetic correlation length now decrease with increasing U, see top left and middle panels of Fig. 31. Another clear indication that this regime has strong correlations comes from the behavior of the density versus chemical potential. In this regime there is a clear plateau at half-filling showing a charge gap of the order $\Delta \sim U/2$. This is compatible with a Mott insulating state at half-filling [198, 209].

Magnetic crossover diagram Our results for the magnetic correlation length are summarized on the bottom right panel of Fig. 31. The intensity map shows that there is a clear dome close to half-filling and $U \simeq 5t$ where the correlation length is maximal. This dome separates a regime of long correlation length for $U \leq 4t - 5t$ where spin-correlation theory can be expected to provide a reasonable description of the physics with a regime at larger $U \geq 6t$ where the physics is qualitatively different and dominated by short-range (quasi) antiferromagnetic correlations.

6.3 Commensurate to incommensurate crossover

In this section, we further investigate the spin correlations in regimes where the correlation length is sizable. We focus in particular on the commensurate or incommensurate nature of the spin correlations by examining the spin susceptibility in momentum space $\chi_{\text{sp}}(\boldsymbol{q})$ and the staggered spin susceptibility in real space $\chi^{\text{st}}_{\text{sp}}(\boldsymbol{r})$ as a function of temperature, density and interaction strength. The results are shown on Fig. 32. It is readily clear that it is very important to have access to large lattices to resolve the details of the spin susceptibility.

The first row of Fig. 32 shows the density dependence at a fixed temperature $T = 0.2t$ and interaction $U = 5t$. This is the value of the interaction for which we find the largest spatial extent of the magnetic correlations in real space, see Fig. 31. Close to half-filling, the spin susceptibility $\chi_{\text{sp}}(\boldsymbol{q})$ is strongly peaked at $\boldsymbol{q} = (\pi, \pi)$. Correspondingly, in real space, the staggered susceptibility shows extended commensurate antiferromagnetic correlations. As the density is reduced, the peak first remains at (π, π) and below a critical density $n \simeq 0.95$ gradually splits into four separate peaks at $(\pi \pm \delta_s, \pi)$ and $(\pi, \pi \pm \delta_s)$, compatible with the square lattice symmetry. The peaks become weaker and wider as the density is further reduced. The real-space staggered spin susceptibility display incommensurate spin correlations for densities below $n \simeq 0.9$ with domain walls separating π-shifted regions with antiferromagnetically correlated spins. The correlation length quickly becomes shorter as the density is reduced. Let us readily mention here that the onset of incommensurate spin correlations is never accompanied by a significant redistribution of the charge in the range of parameters that we have studied, see Sec. 6.4 below.

The second row of Fig. 32 shows the dependence of the spin susceptibility when the interaction strength is changed for a fixed density $n = 0.875$ and temperature $T = 0.1t$. An increasing

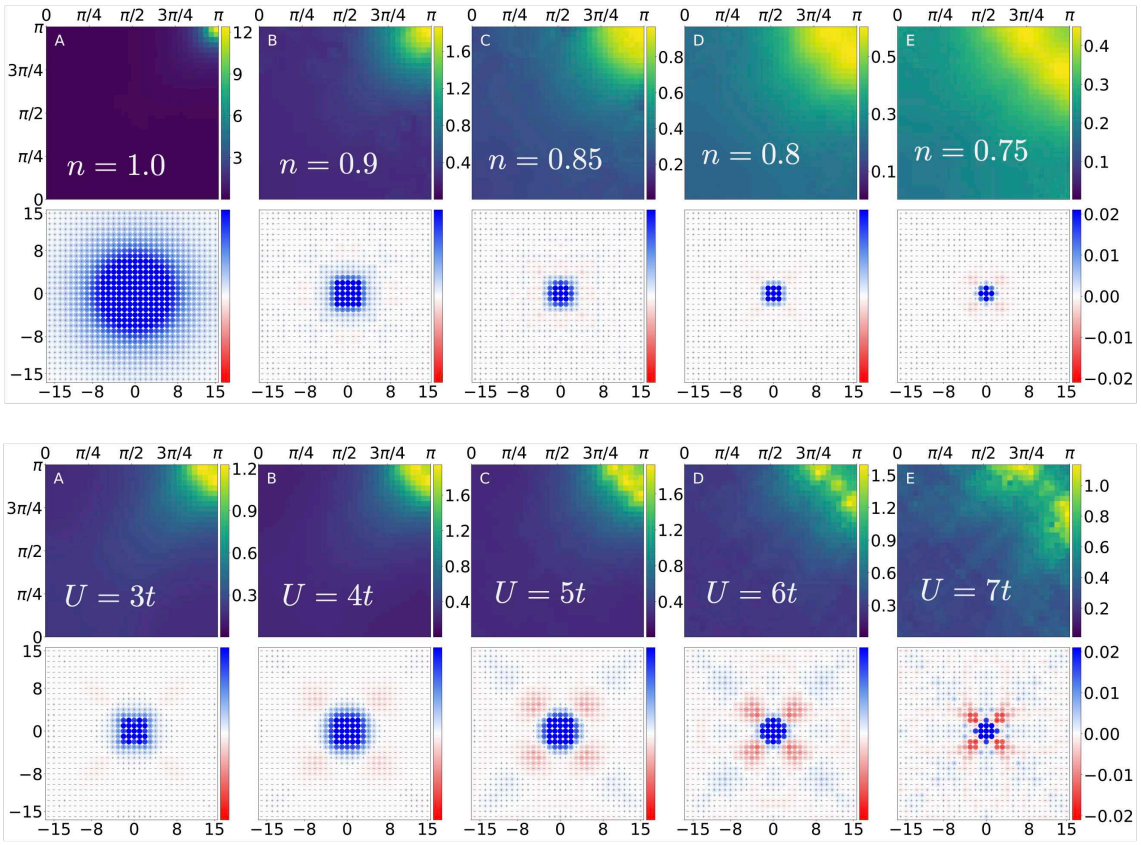

Figure 32: Intensity plots of the spin susceptibility $\chi_{\mathrm{sp}}(\boldsymbol{q})$ together with the corresponding real-space staggered spin susceptibility $\chi^{\mathrm{st}}_{\mathrm{sp}}(\boldsymbol{r}) = (-1)^{x+y}\chi_{\mathrm{sp}}(\boldsymbol{r})$. Top row: Evolution as a function of the doping for $U = 5t$ and $T = 0.2t$. Bottom row: Evolution as a function of U at a fixed density $n = 0.875$ and $T = 0.1t$. Adapted from Ref. [208].

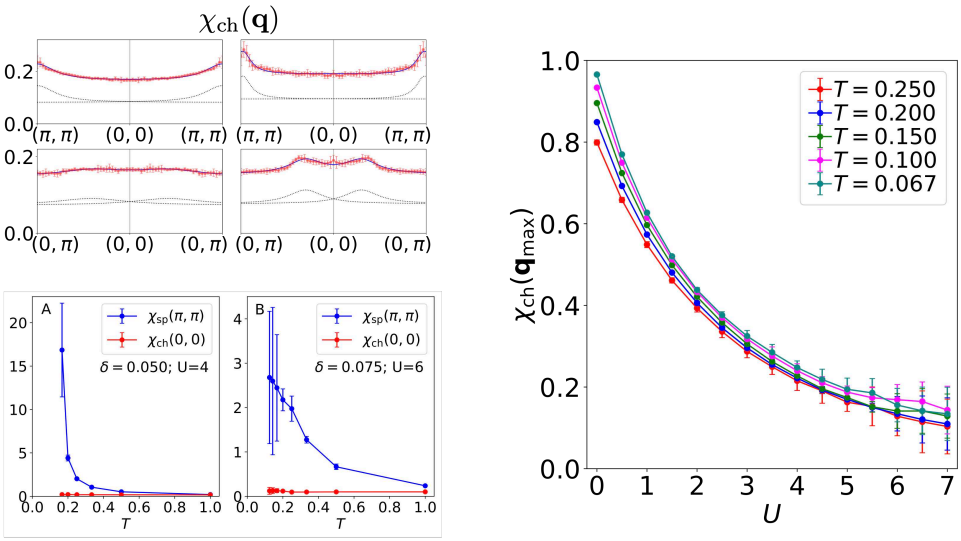

Figure 33: Left panel: Charge susceptibility $\chi_{\rm ch}(\boldsymbol{q})$ along two cuts in the Brillouin zone for $n = 0.8, U = 5t, T = 0.1$ (top left) and $n = 0.89, U = 5t, T = 0.067$ (top right). The temperature evolution of the spin susceptibility and the charge susceptibility is show for two sets of parameters on the bottom. Right panel: Maximum charge susceptibility $\chi_{\rm ch}(\boldsymbol{q}_{\rm max})$ for $n = 0.875$. This behavior can be contrasted to the spin susceptibility shown on Fig. 31. Adapted from Ref. [208].

---

interaction U also splits the peak that was originally at (π, π). Our results suggest that the peaks would remain incommensurate in the limit of very large coupling U, as was also seen in Ref. [210] using a slave-boson approach. Let us mention that we have also found a commensurate to incommensurate crossover as a function of temperature T.

The commensurate to incommensurate crossover has previously been addressed by other numerical methods, albeit at larger temperatures and with less momentum resolution. DQMC has been used at finite temperature and predominantly on the 16×4 cylinder geometry, first for the three-orbital Hubbard model [204] and then for the single-band Hubbard model [179]. The authors also found commensurate spin correlations close to half-filling that become incommensurate at larger doping. These findings have been confirmed in a recent DCA study on 8×8 clusters [205]. Also METTS calculations [207] found incommensurate correlations at $U = 10t$ and 1/16 doping.

6.4 Absence of charge redistribution in the intermediate temperature regime

In this section, we examine whether the onset of incommensurate spin correlations is accompanied by a charge response of the system, as was proposed in previous works [179, 204, 205, 207]. The latter suggest that the formation of incommensurate spin correlations with a wavevector $(\pi \pm \delta_s, \pi)$ is accompanied by incommensurate charge correlations with wavevector $(\pm\delta_c, 0)$ where $\delta_c \simeq 2\delta_s$. No conclusive evidence of charge correlations where found in Ref. [179] except for a weak boundary effect in the real-space staggered susceptibility. In Ref. [207] a clear $(\pm\delta_c, 0)$ peak becomes apparent below $T = 0.05$ for $n = 15/16$ and $U = 10$ and for a cylindrical width-four geometry. Finally, Ref. [205] sees a broadened maximum around the $(0, 0)$ wavevector which can be fitted with a double-Lorentzian revealing two distinct maxima at $(\pm\delta_c, 0)$.

In Fig. 33, we show results for the charge susceptibility $\chi_{\rm ch}(\boldsymbol{q})$ close to the $(0, 0)$ wave vector. We chose different parameters for which the spin susceptibility is large. We find that the charge susceptibility close to $(0, 0)$ is very flat. If we fit $\chi_{\rm ch}$ with a double Lorentzian we find two peaks at an incommensurate wave vector $(\pm\delta_c, 0)$. In general, we do not see a clear connection between

δ_c and δ_s. To a large extent, the structures that we see close to $(0,0)$ are already present in the Lindhard function of the non-interacting system [202, 211]. They do not increase with increasing interaction U or decreasing temperature T, as shown in the right panel of Fig. 33. This behavior is in striking contrast to the behavior of the spin susceptibility in Fig. 31. The charge response in the range of parameters that we studied is at least an order of magnitude smaller that the spin response, see bottom left panel of Fig. 33.

To summarize, our results indicate that, for the parameters that we investigated the charge correlations remain uniform over the lattice even when longer-range spin correlations develop. From our observations this absence of charge stripe correlations persists in the phase diagram at least down to $T \sim 0.10$ and for values of $U < 7$. It is an open and interesting question whether charge correlations would quickly start developing at lower temperatures or larger values of U [207].

6.5 Single-particle response: crossover diagram and spectral fingerprints

We now turn to an investigation of the single-particle properties of the doped Hubbard model and clarify how they are related to the spin and charge correlations discussed above and found in ground-state calculations. A systematic analysis of the self-energies and spectral functions reveals that there are three distinct physical regimes with qualitatively different spectral properties. They are separated by well-defined crossovers as a function of the interaction U and hole doping δ as shown on the first row of Fig. 34 for different temperatures. The regions on these plots correspond to:

The weakly correlated metal The blue region on the first row of Fig. 34 is a weakly correlated metal with an electron-like Fermi surface, very close to the non-interacting system. Note that we take a pragmatic definition of the Fermi surface at finite temperature by identifying it with the maximum of the spectral function proxy $A(\boldsymbol{k}) = -\frac{1}{\pi}\mathrm{Im}G(\boldsymbol{k}, i\omega_0)$. It is understood that a real Fermi surface only exists at $T = 0$, but the maximum of $A(\boldsymbol{k})$ nevertheless gives information about the location of low-energy excitations. The spectral weight in the weakly correlated metal is uniform along the Fermi surface and relatively large, compatible with a small self-energy and long-lived quasiparticles. A representative point of this regime is W.

The strongly correlated metal The green region found at stronger interactions and intermediate doping levels is a different metallic regime. The Fermi surface is hole-like after it has gone through an interaction-driven Lifshitz transition (green triangles in Fig. 34. The self-energy becomes sizable and the quasiparticle lifetime has decreased significantly. The point S is representative of this regime.

The pseudogap regime The red region on Fig. 34 is characterized by the existence of a pseudogap at the antinode $(\pi, 0)$. It can be identified by a suppression of spectral weight, a sudden increase of the self-energy at the antinode or by a reduction of the uniform magnetic susceptibility. All these criteria define slightly different crossover lines that are nevertheless all very close and have the same qualitative behavior. The lighter red area describes a regime where the self-energy undergoes a series of momentum-selective crossovers. Note that the pseudogap only appears at intermediate and strong coupling, where the Fermi surface is already hole-like, as was found in one of our earlier studies [200]. As temperature is lowered, the extent of the pseudogap regime increases. In order to address the question of the interplay between the spatial range of magnetic correlations and the formation of the pseudogap, we also depict on the first row of Fig. 34 contour

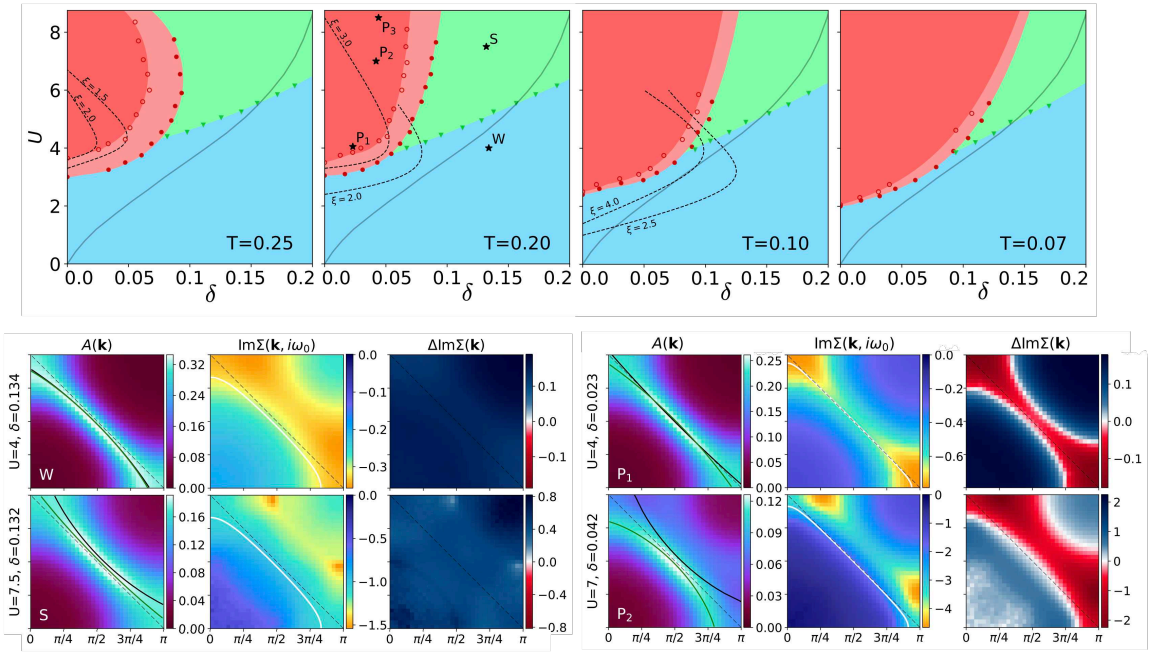

Figure 34: Top row: Three regimes with qualitatively different single-particle spectral behavior. The blue and green regions correspond to a weakly and strongly correlated metal, respectively. The red region corresponds to a regime with a pseudogap at the antinode. The dashed lines are contours of constant spin correlation length (see Fig. 31). The plain gray line, reproduced from Ref. [183], indicated where the ground state displays long-range spin/charge stripe ordering. Bottom row: Spectral function $A(\boldsymbol{k})$, imaginary part of the self-energy at the first Matsubara frequency $\mathrm{Im}\Sigma(\boldsymbol{k}, i\omega_0)$ and difference of the imaginary part between the first two Matsubara frequencies $\Delta\mathrm{Im}\Sigma(\boldsymbol{k}) = \mathrm{Im}\Sigma(\boldsymbol{k}, i\omega_0) - \mathrm{Im}\Sigma(\boldsymbol{k}, i\omega_1)$ over a quarter of the Brillouin zone for four points (see top row) characteristic of the different regimes. The white lines indicate the non-interacting Fermi surface. The green lines show the maximum of the spectral function. Finally, the zero-energy quasiparticle lines are shown in black. Adapted from Ref. [80].

lines of equal spin correlation length ξ (dashed black lines). At weak-to-intermediate interactions, the pseudogap is associated with fairly long-range spin correlations [34, 132, 145, 212], very much like the pseudogap discussed in the half-filled model at weak coupling in Sec. 4.7. At stronger coupling, instead, the pseudogap is already found at high temperature and in regimes where the correlation length is only a couple of lattice sites. This is an important qualitative difference between the nature of the weak coupling pseudogap (point P_1) and the strong coupling pseudogap (points P_2, P_3). We emphasize that the onset and extent of the pseudogap regime seems to be independent from the commensurate or incommensurate nature of the spin correlations discussed above. Indeed, for $T = 0.2t$ and $T = 0.1t$ the crossover from commensurate to incommensurate appears at roughly 10% and 7.5% hole doping, respectively, with a very weak U dependence.

In order to further characterize these different regimes, we show, on the second row of Fig. 34, momentum-resolved spectral properties at $T = 0.2t$: the spectral function proxy $A(\boldsymbol{k})$, the imaginary part of the self-energy at the first Matsubara frequency $\mathrm{Im}\Sigma(\boldsymbol{k}, i\omega_0)$ and the difference between the two first Matsubara frequencies which gives an indication about the low-frequency slope of the self-energy $\Delta\mathrm{Im}\Sigma(\boldsymbol{k}) = \Delta\mathrm{Im}\Sigma(\boldsymbol{k}, i\omega_0) - \Delta\mathrm{Im}\Sigma(\boldsymbol{k}, i\omega_1)$. This difference is positive in a conventional metal. These quantities are computed for the representative points discussed above:

- In the weakly correlated metal (W point, $T = 0.2t, U = 4, n = 0.866$), the Fermi surface (green line) obtained from the maximum of $A(\boldsymbol{k})$ is very close to the non-interacting one (white line). It also coincides with the zero-energy quasiparticle line obtained from $\epsilon_{\boldsymbol{k}} - \mu + \mathrm{Re}\Sigma(\boldsymbol{k}, i\omega_0) = 0$ (black line), which shows where the Fermi surface would be if lifetime effects coming from the imaginary part of the self-energy were neglected. Because the self-energy is small, the zero-energy quasiparticle line is almost unchanged.

- The strongly correlated metal (S point, $T = 0.2t, U = 7.5t, n = 0.868$) displays a reshaped Fermi surface and zero-energy quasiparticle line that become hole-like. This reshaping is the result of a correlation-induced Lifshitz transition induced by the momentum dependence of $\mathrm{Re}\Sigma(\boldsymbol{k}, i\omega_0)$. The green and black lines are slightly different because of prominent peaks in the imaginary part of the self-energy close to $(\pi, \pi/2)$. There is some nodal/antinodal differentiation with about 10% less spectral weight at the antinode. For both metallic regimes S and W, the difference $\Delta\mathrm{Im}\Sigma(\boldsymbol{k})$ is positive over the entire Brillouin zone, as expected for a metal.

- The weak-coupling pseudogap (P_1, $T = 0.2t, U = 4t, n = 0.977$) also has a hole-like zero-energy quasiparticle line resulting from the momentum dependence of the real part of the self-energy. However, because the peaks in the imaginary part of $\Sigma(\boldsymbol{k}, i\omega_0)$ have moved closer to $(\pi, 0)$, the interacting Fermi surface actually remains electron-like. The spectral weight at the antinode is also consequently reduce and roughly 13% smaller as compared to the node.

- In the strong-coupling regime (P_2, $T = 0.2t, U = 7t, n = 0.997$), the pseudogap is much more pronounced and leads to the formation of Fermi arcs around the nodal region. The zero-energy quasiparticle line is strongly modified and hole-like. The spectral function is broadened by lifetime effects and has a maximum that is electron-like but no longer corresponds to well established quasiparticles. For both P_1 and P_2, the difference $\Delta\mathrm{Im}\Sigma(\boldsymbol{k})$ is negative in a region just above the antiferromagnetic Brillouin zone, indicating that the self-energy is large close to the Fermi surface. This change of slope is a good indicator of the onset of the pseudogap regime and defines the red points on the plots of the first row of Fig. 34.

It is interesting to note that, as temperature is decreased in the pseudogap region, the imaginary part of the self-energy increases. But the largest peaks in the imaginary part are found above the antiferromagnetic Brillouin zone. As a result, the lifetime effects are stronger at the antinode,

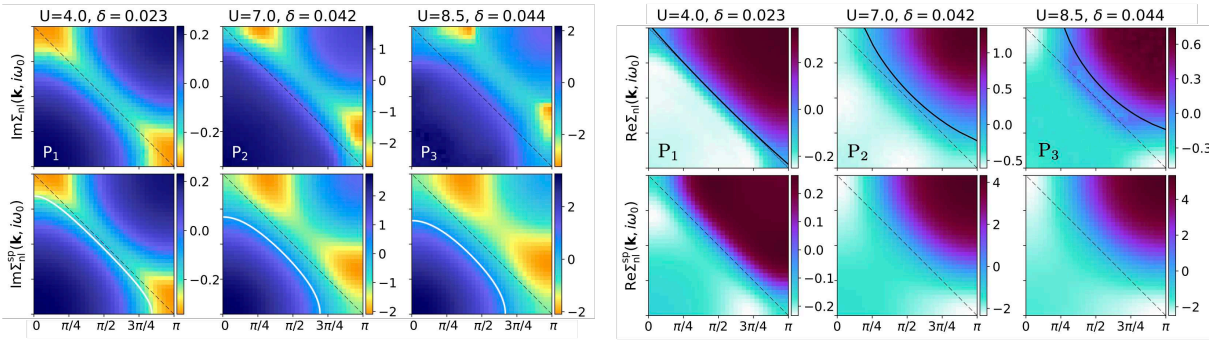

Figure 35: Comparison between the imaginary part (left) and real part (right) of the computed non-local self-energy $\Sigma_{\rm nl}(\boldsymbol{k}, i\omega_0)$ and the modified spin-fluctuation theory $\Sigma^{\rm sf}_{\rm nl}(\boldsymbol{k}, i\omega_n)$ at temperature $T = 0.2t$. The self-energies are shown for selected point in the pseudogap regime, see Fig. 34. Black lines indicate the zero-energy quasiparticle lines, while the white lines indicate the Fermi surface associated with the modified bare Green function $G(\boldsymbol{k}, i\omega_0, \bar{\mu})$. Adapted from Ref. [80].

---

leaving more coherent quasiparticles at the node. This nodal/antinodal dichotomy has also been discussed in cluster extensions of the dynamical mean-field theory [119, 193, 196–198]

6.6 Modified spin-fluctuation approach to the pseudogap

In our study of the weak coupling half-filled Hubbard model in Sec. 4, we have seen that spin-fluctuation theory was quite successful at describing the onset of the pseudogap in the quasi-ordered insulating low temperature regime [34, 132, 145, 212]. At strong coupling, the magnetic correlation length is much shorter and certainly does not satisfy the condition $\xi \gg v_F/\pi T$ for the renormalized classical regime (85). It is nevertheless interesting to ask whether the spectral properties can be described in terms of some spin fluctuation theory. Let us start by mentioning that previous works based on a fluctuation diagnostics [72, 199] have shown that the spin channel is indeed responsible for the onset of the pseudogap. Also, as discussed above, the spin susceptibility is by far the dominating susceptibility in the pseudogap region. As such, the pseudogap is unlikely to be due to the fluctuations of a low-T charge order. These arguments give a good motivation to try to describe the pseudogap in terms of a spin fluctuation inspired theory.

We start by dividing the self-energy into a local and non-local part: $\Sigma = \Sigma_{\rm loc} + \Sigma_{\rm nl}$. The local part is quite large, especially in the strong-coupling regime, and is not adequately approximated by spin-fluctuation theory. A better local self-energy is obtained e.g. from a dynamical mean-field theory calculation. For the non-local part, we use Hedin's equation $\Sigma = -G \star W \star \Gamma$ involving convolutional products over momenta and frequencies, with $W = U - U^2\chi_{\rm sp}$. Here Γ is the vertex function and $\chi_{\rm sp}$ is the dynamical spin susceptibility. We approximate this expression by considering the following ansatz for the non-local part of the self-energy:

$$\Sigma^{\rm sp}_{\rm nl}(\boldsymbol{k}, i\omega_0) = \bar{\gamma}\, U^2\, T \frac{1}{N} \sum_{\boldsymbol{q}} \frac{G_0(\boldsymbol{k}+\boldsymbol{q}, i\omega_0, \bar{\mu})}{(\boldsymbol{Q}-q)^2 + \bar{\xi}^{-2}}. \tag{103}$$

We have replaced the vertex Γ by a constant $\bar{\gamma}$ and the effective spin interaction W by an Ornstein-Zernike form of the commensurate spin susceptibility $\chi_{\rm sp}$ centered around $\boldsymbol{Q} = (\pi, \pi)$ and with correlation length $\bar{\xi}$. In the expression (103), we use a non-interacting form of the Green's function G_0 which, importantly, involves an adjustable chemical potential $\bar{\mu}$. We have also limited the frequency convolution to the zero bosonic Matsubara frequency, an approximation which is known to become more accurate at low-T when a pseudogap opens [34, 132]. We fit our numerically exact

data in order to extract the three parameters $\bar{\gamma}, \bar{\mu}, \bar{\xi}$. Note that we only consider the imaginary part of the self-energy in the optimization process. In Fig. 35, we compare the real and imaginary parts of the non-local part of the computed self-energy Σ_{nl} with the optimized spin-fluctuation expression $\Sigma_{\text{nl}}^{\text{sf}}$ for three points (P_1, P_2, P_3) inside the pseudogap region:

- In the weak-coupling pseudogap regime (point P_1, $T = 0.2t, U = 4t, n = 0.977$), the agreement between the fit and the original data is remarkable, both for the real and imaginary parts. The parameter $\bar{\mu} = -0.26t$ is somewhat lower than the non-interacting chemical potential corresponding to the density ($\mu_0 = -0.10t$). The parameter $\bar{\xi} = 5.0$ is close to the actual (commensurate) value of $\xi = 4.3$ obtained numerically. Finally, $\bar{\gamma} = 0.5$, which hints to the fact that the Γ vertex is relatively uniform and not very large.
- In the strong-coupling pseudogap regime (points P_2, $T = 0.2t, U = 7t, n = 0.958$ and point P_3, $T = 0.2t, U = 8.5, n = 0.956$), the spin-fluctuation still produces a qualitatively correct picture, especially for the imaginary part. Note that the fact that the extrema are roughly in the correct place comes from the freedom to tune $\bar{\mu}$ (see the white lines) in Fig. 35. This freedom to chose the non-interacting propagator is very much reminiscent of the freedom we use with the α-shift when optimizing the convergence radius of the perturbation series, as discussed in Sec. 3.4.2. The fitting procedure yields $\bar{\mu} = -0.89$, $\bar{\xi} = 1.60, \bar{\gamma} = 4.90$ for P_2 and $\bar{\mu} = -1.03$, $\bar{\xi} = 1.25$ and $\bar{\gamma} = 4.84$ for P_3. This shows that the Γ vertex becomes larger in this regime while the correlation length is short. Note that the real part of the self-energy has the correct trends, but the overall magnitude is four times too large.

Our results suggest that a properly modified spin-fluctuation theory can provide an excellent description of the non-local part of the self-energy in the weak-coupling pseudogap regime and still does qualitatively well in its strong-coupling region. In the latter regime, we found it difficult to quantitatively evaluate both the real and the imaginary part. We have also tried to allow for a complex phase in $\bar{\gamma}$ as suggested in Ref. [201], but this did not lead to a better fit. This is certainly a hint that momentum and frequency dependence of the vertex function become more important in the strong coupling regime.

6.7 Fate of the pseudogap at low temperature

One of the main motivation for our study of the doped Hubbard model is to try to establish a connection between the physical nature of the ground state and the finite temperature crossovers described above. Distinct families of computational methods have investigated these two limits [35, 36] but a complete handshake is still lacking. In the present context, an outstanding puzzle is the fate of the pseudogap region at the temperature is cooled down to $T = 0$. How does it connect to the spin/charge stripe order seen in the ground state? Do the Fermi arcs observed at finite temperature eventually evolve into a reconstructed Fermi surface? These questions continue to be a subject of intense debate in the context of cuprate superconductors [10].

In order to address these questions, we extrapolate the crossover lines that we find at several finite temperatures to $T = 0$ and compare with the ground-state result of Ref. [183]. The extrapolation procedure in shown on the left panel of Fig. 36. According to the region in parameter space, we find it easier to extrapolate our data by keeping the doping level δ or the interaction strength U fixed. We use the lowest two temperatures to do a linear extrapolation. This procedure is applied for both the pseudogap crossover line (red) and the Lifshitz transition line (green). The resulting zero-temperature diagram is shown on the right panel of Fig. 36. The red line separates a region with a pseudogap and a region with no pseudogap. The Lifshitz transition extrapolated at $T = 0$ follows this red line up to about 13% and then deviates. The black line is adapted from the AFQMC

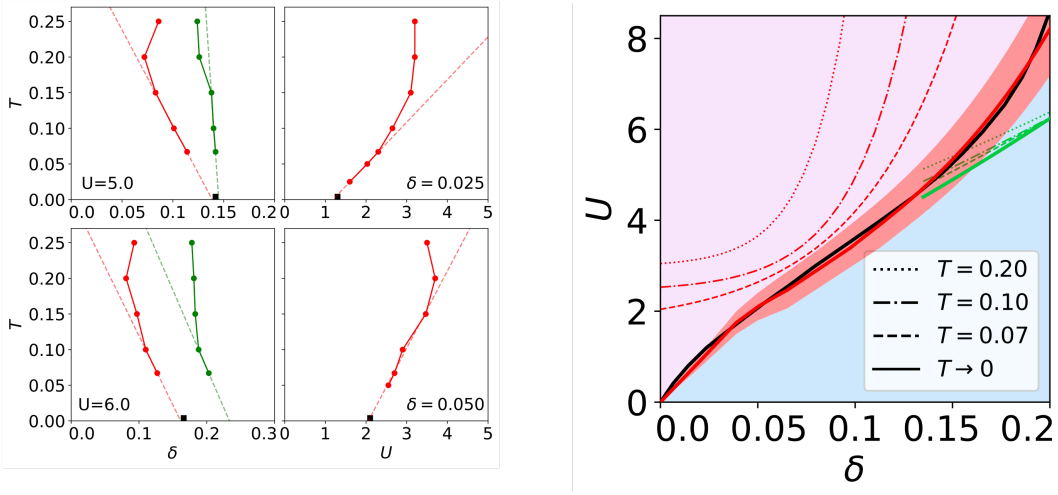

Figure 36: Left panel: Temperature dependence of the pseudogap crossover (red circles) and Lifshitz transition (green circles) at fixed interaction U or fixed doping δ. AFQMC ground-state results from Ref. [183] are shown as black squares. The dashed lines show our linear extrapolation from the lowest available temperatures. Right panel: Resulting zero-temperature extrapolation of the pseudogap crossover region (red line) as well as of the Lifshitz transition line (green line). The black line shows the phase transition line found in Ref. [183] a region with (pink) or without (blue) spin/charge stripe ordering. Adapted from Ref. [80].

---

study of Ref. [183] which is in good agreement with variational Monte Carlo results [182]. The line shows the transition between a state with long-range spin/charge stripe order [31, 180, 189–191] and a state with only short range charge and spin order in the ground state. Remarkably, our extrapolation to $T = 0$ of the pseudogap boundary is in near-perfect agreement with this phase transition line. This seems to indicate that the pseudogap regime eventually becomes stripe-ordered at zero T and that there is no range of doping where the ground state would be a genuine zero-temperature pseudogap phase. This is one of the important conclusions of our work.

6.8 Toward a comprehensive picture

The results that we have obtained for a broad range of parameters allow for a first step toward a unifying qualitative picture of the physical regimes of the doped two-dimensional Hubbard model. Our findings are summarized on the left panel of Fig. 37. At finite temperature, we identify three regimes: a weakly correlated metal (blue) with properties close to the non-interacting system, a strongly correlated metal (green) with a reshaped hole-like Fermi surface and a pseudogap region (red) with a suppression of spectral weight close to the antinode.

When extrapolated to zero temperature, our results seem to indicate that the pseudogap region eventually turns into a long-range ordered charge/spin stripe as found in Ref. [183]. We can therefore attempt to sketch a strong-coupling phase diagram as a function of temperature and doping level. This is shown on the right panel of Fig. 37. The pseudogap and Lifshitz crossovers are indicated by T^* and T_L. We also display the commensurate to incommensurate spin fluctuation crossover T_IC as well as the crossover from a short to a long spin correlation length T_ξ. At higher temperatures, the pseudogap formation is driven by spin correlations and the charge response is very weak. But eventually, at low temperatures, charge correlations should start to grow. This is expected if the ground state is stripe ordered. There is also evidence in Refs [206, 207] that charge correlations appear at low temperatures and that a finite-temperature phase transition to a charge long-range ordered state takes place [206]. From our data, we identify that the ideal

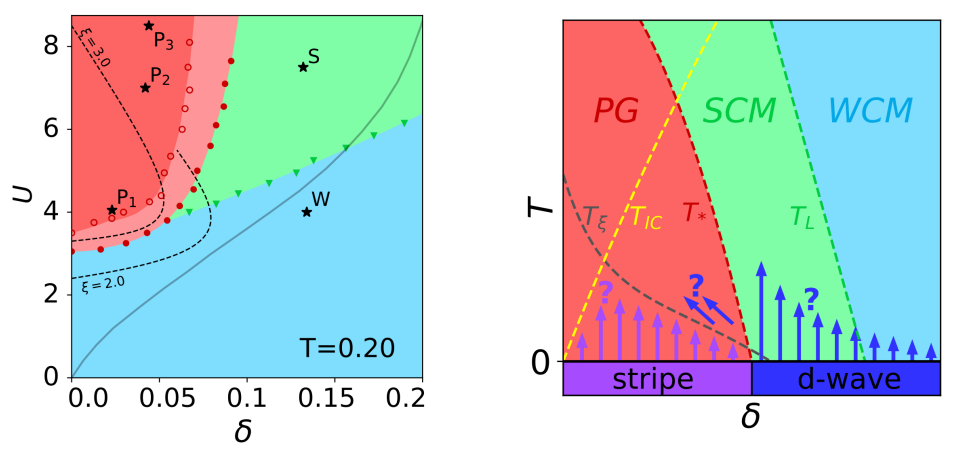

Figure 37: Summary of our results. Left panel: The three regimes with qualitatively different behavior single-particle spectral properties, as already shown in Fig. 34. Right panel: Proposed unifying picture at strong coupling. The pseudogap regime (below T^* in red) extrapolated to a stripe/charge ordered phase a $T = 0$. This may be preempted by a finite-temperature phase transition. The strongly correlated metal and the weakly correlated metal are shown in green and blue, respectively. The dashed gray line (T_ξ) sets a scale below which the magnetic correlation length is large. Below the yellow line (T_{IC}) magnetic correlations are incommensurate. Adapted from Ref. [80].

---

region of parameters to further investigate this question is for $n \simeq 0.9$ and $U \simeq 4t$, a place where long-range incommensurate spin correlations are present. When the doping is increase, the stripe order eventually disappears. In the weak-to-intermediate coupling regime and in the absence of other instabilities, the Hubbard model will eventually turn superconducting because of the Kohn-Luttinger effect [213], albeit at possibly very low temperatures. At stronger coupling, it has been shown that stripe order wins over superconductivity over a significant range of doping [32]. The situation just above the critical doping for stripe order is still under investigation but recent results seem to indicate that superconductivity exists over some range of doping [182].

In conclusion, we have investigated the two-dimensional Hubbard model using a numerically exact diagrammatic Monte Carlo algorithm. We have established crossover diagrams for single-particle properties as well as for magnetic properties. We have shown that a pseudogap regime exists both at weak coupling where the antiferromagnetic correlation length is large and at strong coupling where the correlation length is short ranged. A suitably modified spin-fluctuation theory was found to successfully reproduce some of the salient qualitative features of the pseudogap regime. An important result of our work is that the pseudogap regime eventually turns into a stripe-ordered phase at zero-temperature.

7 Conclusions and perspectives

We have described recent developments and some applications of a class of equilibrium diagrammatic Monte Carlo algorithms based on the original work of Prokof'ev and Svistunov [54]. The strength of the diagrammatic Monte Carlo approach is that it is not limited by the size of the system under consideration and can be used to directly address the thermodynamic limit where finite-size effects are absent. The initial method does however suffer from the fermionic sign problem which limits the number of perturbation series coefficients that can be computed.

On the methodological side, a first line of research has been aiming at improving the statistical variance in order to be able to evaluate more series coefficients. This has led to the development of algorithms that explicitly sum all relevant diagram topologies for a given set of internal interaction vertices [73, 78, 79] in an exponential effort, while the number of topologies is factorial. When the series is convergent, this makes it possible [77] to reach a given accuracy ϵ in a computational time that is a polynomial in ϵ^{-1}.

The availability of more coefficients gives access to more challenging regimes of correlated systems. But these regimes generally also lead to more intricate series that are difficult to resum with standard tools [81–85]. In practice, the resummation is often limited by the presence of poles (or pole-like structures) in the plane of the observable seen as a function of a complex coupling constant. This observation shifted further developments in a different direction, aiming this time at improving the convergence properties of the series. Progress could be made thank to the freedom that exists in choosing the starting point of the perturbation expansion: Different starting points generate different "paths" between the non-interacting system and the interacting one as the coupling constant is increased. As a result, some choices may lead to series that go through better-behaved complex plane structures [59, 72, 86–90] with faster convergence properties. A very interesting byproduct of the use of new starting points is the possibility to express broken-symmetry perturbation series that can yield physical observables directly in an ordered phase [105, 106].

We have used these improved algorithms to investigate the Hubbard model, an epitome of strongly correlated systems. We have mainly focused on its two-dimensional version on a square lattice with only nearest-neighbor hoppings. The opportunity to have unbiased results in non-trivial regimes and with very fine momentum resolution has proven to be a great asset. A systematic analysis of the single- and two-particle response of the system has allowed for a careful characterization of the different regimes of the model at half-filling [34] and in the doped case [80, 208]. In particular, we have investigated how spin-fluctuation mechanisms were related to the formation of a pseudogap, both in cases where the magnetic correlation length is large and when it is only a couple of lattice sites. Our study has also made a first attempt at connecting the pseudogap physics at finite temperature and the zero-temperature results of Ref. [183]. We find evidence that the pseudogap eventually goes through an instability at low temperatures and always becomes an ordered stripe state at zero temperature at low-to-intermediate doping.

These first investigations call for further work. In the doped two-dimensional case, an appealing next step is to include a non-zero next-nearest-neighbor hopping t' in order to make a more realistic contact with cuprate superconductors (for which t' typically lies in the interval $-0.4t \lesssim t' \lesssim -0.1t$) [214]. The fine momentum resolution in the computation of magnetic susceptibilities would allow e.g. to connect to neutron scattering experiments that have investigated the existence of incommensurate magnetic correlations, e.g. in La_2CuO_4 and $YBa_2Cu_3O_6$ compounds [215–217] and observed a linear relationship between the incommensuration vector and the superconducting temperature. Of course, there is the elephant in the room: the superconducting phase. The bottleneck that prevents accessing the superconducting properties is the increasingly complex pole structure that makes the resummation of the series impossible. It is likely that it will take important methodological advances before we are able to compute the normal state properties all the way

down to the critical temperature. But some steps can be taken before that. It would for example be instructive to measure the pairing susceptibility even at temperatures above the superconducting dome and investigate its dependence on doping or nearest-neighbor hopping. In a previous work [72], we have performed a fluctuation diagnostics comparing the contribution of different channels (spin, charge and pairing) to the self-energy. At the temperatures we could reach, $T \simeq 0.2t$, the signal in the pairing channel was extremely weak. But progress in the meanwhile makes it possible to go to temperature $T \simeq 0.07t$ and it would be very instructive to see whether the pairing susceptibility shows some evidence of the superconducting state. A different approach is to try to directly stabilize the superconducting solution, as we have done for superconductivity in the negative-U Hubbard model [106] or antiferromagnetism in the three-dimensional repulsive Hubbard model (Sec. 5). In these works, we have observed that the series is sometimes easier to compute and resum deep into the ordered phase than it is close to the phase transition. Constructing the series from a superconducting non-interacting system may provide a shortcut to the superconducting dome of the two-dimensional Hubbard model. Being able to determine whether the doped Hubbard model has a superconducting phase for $t' \neq 0$ and establishing its connection with single-particle properties such as the pseudogap is certainly one of the great challenges in the field.

While we have concentrated most of our discussion on single-band Hubbard models, the diagrammatic Monte Carlo method is quite versatile and perturbation series can be written for many different models. For example, results have been obtained for the polaron problem [55–58], the electron gas [59–61] or the unitary gas [62] to mention but a few. It would be exciting to explore whether other systems, such as frustrated spin systems, could also be approached with algorithms similar to those presented above. We have started to investigate an algorithm that uses a Majorana representation of a spin-1/2. Interestingly Majorana fermions also have a Wick theorem and a recursion very similar to Sec. 3.1 can be designed, except that determinants are replaced with Pfaffians. It is still an open question how the sign problem will behave in this representation and whether low temperatures are reachable.

Another largely unexplored territory is that of multiorbital models, which are essential for the study of more realistic models. A first work in this direction is Ref. [218] that designed a diagrammatic Monte Carlo algorithm for impurity models with general interactions and hybridizations. Introducing several coupling constants raises interesting questions about the most efficient way to design a perturbation series. Treating all interaction terms with the same expansion parameter seems to lead to very complex pole structures and difficult resummations. In that respect, it is worth investigating whether different expansions, maybe multiple expansions in several coupling constants, lead to better-behaved series.

At about the same time when the more recent diagrammatic Monte Carlo algorithms for equilibrium were being developed, several lines of research aiming at the construction of algorithms describing the real-time evolution of quantum systems were conducted. Among them are for example the inchworm algorithms [219–224] that construct propagators in time iteratively, reusing information obtained in previous steps and thus reducing the sign problem. Another class of algorithms compute the time integrals appearing in Feynman diagrams analytically [225–230]. This allows for a controlled continuation to the real axis. The complexity however comes from the very arduous expressions that need to be evaluated and algorithms that can perform symbolic calculations need to be implemented. Besides these efforts, maybe one of the most promising family of algorithms are those that implement an interaction expansion in the Keldysh [231] formalism. Very much like for the CDet algorithm, it has been shown that explicitly summing a class of diagrams, via a sum over all Keldysh indices for a given set of interaction vertices, leads to important cancellations and a great reduction of the variance [86, 232, 233]. Recent developments for this class of real-time algorithm also show that more accurate results can be obtained by replacing the stochastic integration by either integration based on low-discrepancy sequences (quasi Monte Carlo) [234, 235] or, more recently, by a low-rank tensor network representation of the function to be integrated [236–240].

These techniques have focused their attention on the real-time dynamics of quantum impurity problems. Whether they can be extended to a lattice model, possibly at equilibrium, is an outstanding question and a very exciting future line of research.

In summary, there has been an intense activity in the design of new diagrammatic Monte Carlo algorithm over the last years. It has lead to great improvements and encouraging first results in highly non-trivial regimes of strongly correlated systems that sometimes even set the current state-of-the-art of quantum many-body methods. But there are still many outstanding challenges ahead to make these algorithms more robust and applicable to a broader class of realistic models.

8 References

[1] E. Dagotto, "Complexity in strongly correlated electronic systems," Science **309**, 257–262 (2005).

[2] N. F. Mott, "The basis of the electron theory of metals, with special reference to the transition metals," Proceedings of the Physical Society. Section A **62**, 416 (1949).

[3] S. Sachdev, *Quantum Phase Transitions*, 2nd ed. (Cambridge University Press, Cambridge, 2011).

[4] D. J. Scalapino, "A common thread: The pairing interaction for unconventional superconductors," Rev. Mod. Phys. **84**, 1383–1417 (2012).

[5] J. G. Bednorz and K. A. Müller, "Possible high t_c superconductivity in the ba–la–cu–o system," Zeitschrift für Physik B Condensed Matter **64**, 189–193 (1986).

[6] B. Keimer, S. A. Kivelson, M. R. Norman, S. Uchida, and J. Zaanen, "From quantum matter to high-temperature superconductivity in copper oxides," Nature **518**, 179–186 (2015).

[7] P. W. Anderson, "More is different," Science **177**, 393–396 (1972).

[8] H. Alloul, P. Mendels, H. Casalta, J. F. Marucco, and J. Arabski, "Correlations between magnetic and superconducting properties of zn-substituted $yba_2cu_3o_{6+x}$," Phys. Rev. Lett. **67**, 3140–3143 (1991).

[9] H. Alloul, "What is the simplest model that captures the basic experimental facts of the physics of underdoped cuprates?" Comptes Rendus Physique **15**, 519–524 (2014).

[10] C. Proust and L. Taillefer, "The remarkable underlying ground states of cuprate superconductors," Annual Review of Condensed Matter Physics **10**, 409–429 (2019).

[11] N. E. Hussey, K. Takenaka, and H. Takagi, "Universality of the mott–ioffe–regel limit in metals," Philosophical Magazine **84**, 2847–2864 (2004).

[12] P. A. M. Dirac and R. H. Fowler, "Quantum mechanics of many-electron systems," Proc. R. Soc. Lond. A **123**, 714–733 (1929).

[13] E. Ising, "Beitrag zur theorie des ferromagnetismus," Zeitschrift für Physik **31**, 253–258 (1925).

[14] W. Lenz, "Beitrag zum verständnis der magnetischen erscheinungen in festen körpern," Physikalische Zeitschrift **21**, 613–615 (1920).

[15] J. Hubbard, "Electron Correlations in Narrow Energy Bands," Proc. R. Soc. Lond. A **276**, 238–257 (1963).

[16] J. Kanamori, "Electron Correlation and Ferromagnetism of Transition Metals," Progress of Theoretical Physics **30**, 275–289 (1963).

[17] M. C. Gutzwiller, "Effect of correlation on the ferromagnetism of transition metals," Phys. Rev. Lett. **10**, 159–162 (1963).

[18] J. Hubbard, "Electron Correlations in Narrow Energy Bands. III. An Improved Solution," Proc. R. Soc. Lond. A **281**, 401–419 (1964).

[19] M. Imada, A. Fujimori, and Y. Tokura, "Metal-insulator transitions," Rev. Mod. Phys. **70**, 1039–1263 (1998).

[20] J. Orenstein and A. J. Millis, "Advances in the physics of high-temperature superconductivity," Science **288**, 468–474 (2000).

[21] P. W. Anderson, "The resonating valence bond state in la_2cuo_4 and superconductivity," Science **235**, 1196–1198 (1987).

[22] I. Bloch, "Ultracold quantum gases in optical lattices," Nature Physics **1**, 23–30 (2005).

[23] R. Jördens, N. Strohmaier, K. Günter, H. Moritz, and T. Esslinger, "A mott insulator of fermionic atoms in an optical lattice," Nature **455**, 204–207 (2008).

[24] D. Greif, G. Jotzu, M. Messer, R. Desbuquois, and T. Esslinger, "Formation and dynamics of antiferromagnetic correlations in tunable optical lattices," Phys. Rev. Lett. **115**, 260401 (2015).

[25] M. F. Parsons, A. Mazurenko, C. S. Chiu, G. Ji, D. Greif, and M. Greiner, "Site-resolved measurement of the spin-correlation function in the fermi-hubbard model," Science **353**, 1253–1256 (2016).

[26] L. W. Cheuk, M. A. Nichols, K. R. Lawrence, M. Okan, H. Zhang, E. Khatami, N. Trivedi, T. Paiva, M. Rigol, and M. W. Zwierlein, "Observation of spatial charge and spin correlations in the 2d fermi-hubbard model," Science **353**, 1260–1264 (2016).

[27] A. Mazurenko, C. S. Chiu, G. Ji, M. F. Parsons, M. Kanász-Nagy, R. Schmidt, F. Grusdt, E. Demler, D. Greif, and M. Greiner, "A cold-atom fermi–hubbard antiferromagnet," Nature **545**, 462–466 (2017).

[28] E. H. Lieb and F. Y. Wu, "Absence of mott transition in an exact solution of the short-range, one-band model in one dimension," Phys. Rev. Lett. **20**, 1445–1448 (1968).

[29] T. Giamarchi, *Quantum Physics in One Dimension* (Oxford University Press, 2003).

[30] J. P. F. LeBlanc, A. E. Antipov, F. Becca, I. W. Bulik, G. K.-L. Chan, C.-M. Chung, Y. Deng, M. Ferrero, T. M. Henderson, C. A. Jiménez-Hoyos, E. Kozik, X.-W. Liu, A. J. Millis, N. V. Prokof'ev, M. Qin, G. E. Scuseria, H. Shi, B. V. Svistunov, L. F. Tocchio, I. S. Tupitsyn, S. R. White, S. Zhang, B.-X. Zheng, Z. Zhu, and E. Gull (Simons Collaboration on the Many-Electron Problem), "Solutions of the two-dimensional hubbard model: Benchmarks and results from a wide range of numerical algorithms," Phys. Rev. X **5**, 041041 (2015).

[31] B.-X. Zheng, C.-M. Chung, P. Corboz, G. Ehlers, M.-P. Qin, R. M. Noack, H. Shi, S. R. White, S. Zhang, and G. K.-L. Chan, "Stripe order in the underdoped region of the two-dimensional hubbard model," Science **358**, 1155–1160 (2017).

[32] M. Qin, C.-M. Chung, H. Shi, E. Vitali, C. Hubig, U. Schollwöck, S. R. White, and S. Zhang (Simons Collaboration on the Many-Electron Problem), "Absence of superconductivity in the pure two-dimensional hubbard model," Phys. Rev. X **10**, 031016 (2020).

[33] C.-M. Chung, M. Qin, S. Zhang, U. Schollwöck, and S. R. White (The Simons Collaboration on the Many-Electron Problem), "Plaquette versus ordinary d-wave pairing in the t'-hubbard model on a width-4 cylinder," Phys. Rev. B **102**, 041106 (2020).

[34] T. Schäfer, N. Wentzell, F. Šimkovic, Y.-Y. He, C. Hille, M. Klett, C. J. Eckhardt, B. Arzhang, V. Harkov, F. m. c.-M. Le Régent, A. Kirsch, Y. Wang, A. J. Kim, E. Kozik, E. A. Stepanov, A. Kauch, S. Andergassen, P. Hansmann, D. Rohe, Y. M. Vilk, J. P. F. LeBlanc, S. Zhang, A.-M. S. Tremblay, M. Ferrero, O. Parcollet, and A. Georges, "Tracking the footprints of spin fluctuations: A multimethod, multimessenger study of the two-dimensional hubbard model," Phys. Rev. X **11**, 011058 (2021).

[35] M. Qin, T. Schäfer, S. Andergassen, P. Corboz, and E. Gull, "The hubbard model: A computational perspective," Annual Review of Condensed Matter Physics **13**, 275–302 (2022).

[36] D. P. Arovas, E. Berg, S. A. Kivelson, and S. Raghu, "The hubbard model," Annual Review of Condensed Matter Physics **13**, 239–274 (2022).

[37] S. Zhang, "Auxiliary-field quantum monte carlo for correlated electron systems," in *Emergent Phenomena in Correlated Matter*, Schriften des Forschungszentrums Jülich. Reihe modeling and simulation, Vol. 3, edited by E. Pavarini, E. Koch, and U. Schollwöck (Forschungszentrum Jülich GmbH Zentralbibliothek, Verlag, 2013) p. 15.1.

[38] H. Shi and S. Zhang, "Infinite variance in fermion quantum monte carlo calculations," Phys. Rev. E **93**, 033303 (2016).

[39] H. Shi and S. Zhang, "Symmetry in auxiliary-field quantum monte carlo calculations," Phys. Rev. B **88**, 125132 (2013).

[40] M. Troyer and U.-J. Wiese, "Computational complexity and fundamental limitations to fermionic quantum monte carlo simulations," Phys. Rev. Lett. **94**, 170201 (2005).

[41] S. R. White, "Density matrix formulation for quantum renormalization groups," Phys. Rev. Lett. **69**, 2863–2866 (1992).

[42] U. Schollwöck, "The density-matrix renormalization group in the age of matrix product states," Annals of Physics **326**, 96–192 (2011), january 2011 Special Issue.

[43] A. Georges, G. Kotliar, W. Krauth, and M. J. Rozenberg, "Dynamical mean-field theory of strongly correlated fermion systems and the limit of infinite dimensions," Rev. Mod. Phys. **68**, 13–125 (1996).

[44] W. Metzner and D. Vollhardt, "Correlated lattice fermions in $d = \infty$ dimensions," Phys. Rev. Lett. **62**, 324–327 (1989).

[45] A. Georges and G. Kotliar, "Hubbard model in infinite dimensions," Phys. Rev. B **45**, 6479–6483 (1992).

[46] T. Maier, M. Jarrell, T. Pruschke, and M. H. Hettler, "Quantum cluster theories," Rev. Mod. Phys. **77**, 1027–1080 (2005).

[47] G. Rohringer, H. Hafermann, A. Toschi, A. A. Katanin, A. E. Antipov, M. I. Katsnelson, A. I. Lichtenstein, A. N. Rubtsov, and K. Held, "Diagrammatic routes to nonlocal correlations beyond dynamical mean field theory," Rev. Mod. Phys. **90**, 025003 (2018).

[48] E. Gull, A. J. Millis, A. I. Lichtenstein, A. N. Rubtsov, M. Troyer, and P. Werner, "Continuous-time monte carlo methods for quantum impurity models," Rev. Mod. Phys. **83**, 349–404 (2011).

[49] R. Blankenbecler, D. J. Scalapino, and R. L. Sugar, "Monte Carlo calculations of coupled boson-fermion systems. I," Phys. Rev. D **24**, 2278–2286 (1981).

[50] F. Assaad and H. Evertz, "World-line and Determinantal Quantum Monte Carlo Methods for Spins, Phonons and Electrons," in *Computational Many-Particle Physics*, Lecture Notes in Physics, Vol. 739, edited by H. Fehske, R. Schneider, and A. Weiße (Springer Berlin Heidelberg, 2008) pp. 277–356.

[51] C.-C. Chang, S. Gogolenko, J. Perez, Z. Bai, and R. T. Scalettar, "Recent advances in determinant quantum monte carlo," Philosophical Magazine **95**, 1260–1281 (2015).

[52] Y.-Y. He, M. Qin, H. Shi, Z.-Y. Lu, and S. Zhang, "Finite-temperature auxiliary-field quantum Monte Carlo: Self-consistent constraint and systematic approach to low temperatures," Phys. Rev. B **99**, 045108 (2019).

[53] Y.-Y. He, H. Shi, and S. Zhang, "Reaching the continuum limit in finite-temperature ab initio field-theory computations in many-fermion systems," Phys. Rev. Lett. **123**, 136402 (2019).

[54] N. V. Prokof'ev, B. V. Svistunov, and I. S. Tupitsyn, "Exact, complete, and universal continuous-time worldline monte carlo approach to the statistics of discrete quantum systems," Journal of Experimental and Theoretical Physics **87**, 310–321 (1998).

[55] N. V. Prokof'ev and B. V. Svistunov, "Polaron problem by diagrammatic quantum monte carlo," Phys. Rev. Lett. **81**, 2514–2517 (1998).

[56] A. S. Mishchenko, N. V. Prokof'ev, B. V. Svistunov, and A. Sakamoto, "Comprehensive study of fröhlich polaron," International Journal of Modern Physics B **15**, 3940–3943 (2001).

[57] N. Prokof'ev and B. Svistunov, "Bold diagrammatic monte carlo technique: When the sign problem is welcome," Phys. Rev. Lett. **99**, 250201 (2007).

[58] N. V. Prokof'ev and B. V. Svistunov, "Bold diagrammatic monte carlo: A generic sign-problem tolerant technique for polaron models and possibly interacting many-body problems," Phys. Rev. B **77**, 125101 (2008).

[59] K. Chen and K. Haule, "A combined variational and diagrammatic quantum monte carlo approach to the many-electron problem," Nature Communications **10**, 3725 (2019).

[60] J. P. F. LeBlanc, K. Chen, K. Haule, N. V. Prokof'ev, and I. S. Tupitsyn, "Dynamic response of an electron gas: Towards the exact exchange-correlation kernel," Phys. Rev. Lett. **129**, 246401 (2022).

[61] K. Haule and K. Chen, "Single-particle excitations in the uniform electron gas by diagrammatic monte carlo," Scientific Reports **12**, 2294 (2022).

[62] K. Van Houcke, F. Werner, E. Kozik, N. Prokof'ev, B. Svistunov, M. J. H. Ku, A. T. Sommer, L. W. Cheuk, A. Schirotzek, and M. W. Zwierlein, "Feynman diagrams versus fermi-gas feynman emulator," Nature Physics **8**, 366–370 (2012).

[63] A. N. Rubtsov, "Quantum monte carlo determinantal algorithm without hubbard-stratonovich transformation: a general consideration," Preprint **arXiv**, cond–mat/0302228 (2003).

[64] A. N. Rubtsov and A. I. Lichtenstein, "Continuous-time quantum Monte Carlo method for fermions: Beyond auxiliary field framework," Journal of Experimental and Theoretical Physics Letters **80**, 61–65 (2004).

[65] E. Bourovski, N. Prokof'ev, and B. Svistunov, "Truncated-determinant diagrammatic monte carlo for fermions with contact interaction," Phys. Rev. B **70**, 193101 (2004).

[66] A. N. Rubtsov, V. V. Savkin, and A. I. Lichtenstein, "Continuous-time quantum monte carlo method for fermions," Phys. Rev. B **72**, 035122 (2005).

[67] P. Werner and A. J. Millis, "Hybridization expansion impurity solver: General formulation and application to kondo lattice and two-orbital models," Phys. Rev. B **74**, 155107 (2006).

[68] P. Werner, A. Comanac, L. de' Medici, M. Troyer, and A. J. Millis, "Continuous-time solver for quantum impurity models," Phys. Rev. Lett. **97**, 076405 (2006).

[69] E. Gull, P. Werner, O. Parcollet, and M. Troyer, "Continuous-time auxiliary-field monte carlo for quantum impurity models," Europhysics Letters **82**, 57003 (2008).

[70] F. Šimkovic and R. Rossi, "Many-configuration markov-chain monte carlo," Preprint **arXiv**, 2102.05613 (2021).

[71] K. Van Houcke, E. Kozik, N. Prokof'ev, and B. Svistunov, "Diagrammatic monte carlo," Physics Procedia **6**, 95–105 (2010), computer Simulations Studies in Condensed Matter Physics XXI.

[72] W. Wu, M. Ferrero, A. Georges, and E. Kozik, "Controlling feynman diagrammatic expansions: Physical nature of the pseudogap in the two-dimensional hubbard model," Phys. Rev. B **96**, 041105 (2017).

[73] R. Rossi, "Determinant diagrammatic monte carlo algorithm in the thermodynamic limit," Phys. Rev. Lett. **119**, 045701 (2017).

[74] K. Griffin and M. J. Tsatsomeros, "Principal minors, part i: A method for computing all the principal minors of a matrix," Linear Algebra and its applications **419**, 107–124 (2006).

[75] F. i. c. v. IV and M. Ferrero, "Fast principal minor algorithms for diagrammatic monte carlo," Phys. Rev. B **105**, 125104 (2022).

[76] A. Björklund, T. Husfeldt, P. Kaski, and M. Koivisto, "Fourier meets möbius: Fast subset convolution," in *Proceedings of the Thirty-Ninth Annual ACM Symposium on Theory of Computing*, STOC '07 (Association for Computing Machinery, New York, NY, USA, 2007) p. 67–74.

[77] R. Rossi, N. Prokof'ev, B. Svistunov, K. V. Houcke, and F. Werner, "Polynomial complexity despite the fermionic sign," Europhysics Letters **118**, 10004 (2017).

[78] A. Moutenet, W. Wu, and M. Ferrero, "Determinant monte carlo algorithms for dynamical quantities in fermionic systems," Phys. Rev. B **97**, 085117 (2018).

[79] F. Šimkovic and E. Kozik, "Determinant monte carlo for irreducible feynman diagrams in the strongly correlated regime," Phys. Rev. B **100**, 121102 (2019).

[80] F. Simkovic, R. Rossi, A. Georges, and M. Ferrero, "Origin and fate of the pseudogap in the doped hubbard model," Preprint **arXiv**, 2209.09237 (2022).

[81] A. J. Guttmann, "Asymptotic analysis of coefficients," Phase transitions and critical phenomena **13**, 1–234 (1989).

[82] C. Brezinski, "Extrapolation algorithms and padé approximations: a historical survey," Applied Numerical Mathematics **20**, 299–318 (1996).

[83] P. Gonnet, S. Güttel, and L. N. Trefethen, "Robust padé approximation via svd," SIAM Review **55**, 101–117 (2013).

[84] G. A. Baker, "Application of the padé approximant method to the investigation of some magnetic properties of the ising model," Phys. Rev. **124**, 768–774 (1961).

[85] D. L. Hunter and G. A. Baker, "Methods of series analysis. iii. integral approximant methods," Phys. Rev. B **19**, 3808–3821 (1979).

[86] R. E. V. Profumo, C. Groth, L. Messio, O. Parcollet, and X. Waintal, "Quantum monte carlo for correlated out-of-equilibrium nanoelectronic devices," Phys. Rev. B **91**, 245154 (2015).

[87] R. Rossi, F. Werner, N. Prokof'ev, and B. Svistunov, "Shifted-action expansion and applicability of dressed diagrammatic schemes," Phys. Rev. B **93**, 161102 (2016).

[88] R. Rossi, F. Šimkovic, and M. Ferrero, "Renormalized perturbation theory at large expansion orders," Europhysics Letters **132**, 11001 (2020).

[89] F. Šimkovic, R. Rossi, and M. Ferrero, "Efficient one-loop-renormalized vertex expansions with connected determinant diagrammatic monte carlo," Phys. Rev. B **102**, 195122 (2020).

[90] A. J. Kim, N. V. Prokof'ev, B. V. Svistunov, and E. Kozik, "Homotopic action: A pathway to convergent diagrammatic theories," Phys. Rev. Lett. **126**, 257001 (2021).

[91] E. Kozik, M. Ferrero, and A. Georges, "Nonexistence of the luttinger-ward functional and misleading convergence of skeleton diagrammatic series for hubbard-like models," Phys. Rev. Lett. **114**, 156402 (2015).

[92] A. Stan, P. Romaniello, S. Rigamonti, L. Reining, and J. A. Berger, "Unphysical and physical solutions in many-body theories: from weak to strong correlation," New Journal of Physics **17**, 093045 (2015).

[93] R. Rossi and F. Werner, "Skeleton series and multivaluedness of the self-energy functional in zero space-time dimensions," Journal of Physics A: Mathematical and Theoretical **48**, 485202 (2015).

[94] J. Vučičević, N. Wentzell, M. Ferrero, and O. Parcollet, "Practical consequences of the luttinger-ward functional multivaluedness for cluster dmft methods," Phys. Rev. B **97**, 125141 (2018).

[95] A. J. Kim and V. Sacksteder, "Multivaluedness of the luttinger-ward functional in the fermionic and bosonic system with replicas," Phys. Rev. B **101**, 115146 (2020).

[96] T. Schäfer, G. Rohringer, O. Gunnarsson, S. Ciuchi, G. Sangiovanni, and A. Toschi, "Divergent Precursors of the Mott-Hubbard Transition at the Two-Particle Level," Phys. Rev. Lett. **110**, 246405 (2013).

[97] V. Janiš and V. Pokorný, "Critical metal-insulator transition and divergence in a two-particle irreducible vertex in disordered and interacting electron systems," Phys. Rev. B **90**, 045143 (2014).

[98] T. Schäfer, S. Ciuchi, M. Wallerberger, P. Thunström, O. Gunnarsson, G. Sangiovanni, G. Rohringer, and A. Toschi, "Nonperturbative landscape of the mott-hubbard transition: Multiple divergence lines around the critical endpoint," Phys. Rev. B **94**, 235108 (2016).

[99] O. Gunnarsson, G. Rohringer, T. Schäfer, G. Sangiovanni, and A. Toschi, "Breakdown of traditional many-body theories for correlated electrons," Phys. Rev. Lett. **119**, 056402 (2017).

[100] P. Thunström, O. Gunnarsson, S. Ciuchi, and G. Rohringer, "Analytical investigation of singularities in two-particle irreducible vertex functions of the Hubbard atom," Phys. Rev. B **98**, 235107 (2018).

[101] P. Chalupa, P. Gunacker, T. Schäfer, K. Held, and A. Toschi, "Divergences of the irreducible vertex functions in correlated metallic systems: Insights from the Anderson impurity model," Phys. Rev. B **97**, 245136 (2018).

[102] D. Springer, P. Chalupa, S. Ciuchi, G. Sangiovanni, and A. Toschi, "Interplay between local response and vertex divergences in many-fermion systems with on-site attraction," Phys. Rev. B **101**, 155148 (2020).

[103] M. Reitner, P. Chalupa, L. Del Re, D. Springer, S. Ciuchi, G. Sangiovanni, and A. Toschi, "Attractive effect of a strong electronic repulsion: The physics of vertex divergences," Phys. Rev. Lett. **125**, 196403 (2020).

[104] P. Chalupa, T. Schäfer, M. Reitner, D. Springer, S. Andergassen, and A. Toschi, "Fingerprints of the Local Moment Formation and its Kondo Screening in the Generalized Susceptibilities of Many-Electron Problems," Phys. Rev. Lett. **126**, 056403 (2021).

[105] R. Garioud, F. Šimkovic, R. Rossi, G. Spada, T. Schäfer, F. Werner, and M. Ferrero, "Precise many-body simulations of antiferromagnetic phases using broken-symmetry perturbative expansions," Preprint **arXiv**, 2210.17423 (2022).

[106] G. Spada, R. Rossi, F. Simkovic, R. Garioud, M. Ferrero, K. Van Houcke, and F. Werner, "High-order expansion around bcs theory," Preprint **arXiv**, 2103.12038 (2021).

[107] J. C. Slater, "Magnetic effects and the hartree-fock equation," Phys. Rev. **82**, 538–541 (1951).

[108] N. D. Mermin and H. Wagner, "Absence of ferromagnetism or antiferromagnetism in one- or two-dimensional isotropic heisenberg models," Phys. Rev. Lett. **17**, 1133–1136 (1966).

[109] P. C. Hohenberg, "Existence of long-range order in one and two dimensions," Phys. Rev. **158**, 383–386 (1967).

[110] F. Šimkovic, J. P. F. LeBlanc, A. J. Kim, Y. Deng, N. V. Prokof'ev, B. V. Svistunov, and E. Kozik, "Extended crossover from a fermi liquid to a quasiantiferromagnet in the half-filled 2d hubbard model," Phys. Rev. Lett. **124**, 017003 (2020).

[111] A. J. Kim, F. Simkovic, and E. Kozik, "Spin and charge correlations across the metal-to-insulator crossover in the half-filled 2d hubbard model," Phys. Rev. Lett. **124**, 117602 (2020).

[112] A. A. Katanin, A. Toschi, and K. Held, "Comparing pertinent effects of antiferromagnetic fluctuations in the two- and three-dimensional hubbard model," Phys. Rev. B **80**, 075104 (2009).

[113] T. Schäfer, F. Geles, D. Rost, G. Rohringer, E. Arrigoni, K. Held, N. Blümer, M. Aichhorn, and A. Toschi, "Fate of the false mott-hubbard transition in two dimensions," Phys. Rev. B **91**, 125109 (2015).

[114] G. Rohringer and A. Toschi, "Impact of nonlocal correlations over different energy scales: A dynamical vertex approximation study," Phys. Rev. B **94**, 125144 (2016).

[115] H. Park, K. Haule, and G. Kotliar, "Cluster dynamical mean field theory of the mott transition," Phys. Rev. Lett. **101**, 186403 (2008).

[116] P. Werner, E. Gull, O. Parcollet, and A. J. Millis, "Momentum-selective metal-insulator transition in the two-dimensional hubbard model: An 8-site dynamical cluster approximation study," Phys. Rev. B **80**, 045120 (2009).

[117] M. H. Hettler, A. N. Tahvildar-Zadeh, M. Jarrell, T. Pruschke, and H. R. Krishnamurthy, "Nonlocal dynamical correlations of strongly interacting electron systems," Phys. Rev. B **58**, R7475–R7479 (1998).

[118] M. H. Hettler, M. Mukherjee, M. Jarrell, and H. R. Krishnamurthy, "Dynamical cluster approximation: Nonlocal dynamics of correlated electron systems," Phys. Rev. B **61**, 12739–12756 (2000).

[119] O. Parcollet, G. Biroli, and G. Kotliar, "Cluster dynamical mean field analysis of the mott transition," Phys. Rev. Lett. **92**, 226402 (2004).

[120] S. Sakai, G. Sangiovanni, M. Civelli, Y. Motome, K. Held, and M. Imada, "Cluster-size dependence in cellular dynamical mean-field theory," Phys. Rev. B **85**, 035102 (2012).

[121] M. Klett, N. Wentzell, T. Schäfer, F. Simkovic, O. Parcollet, S. Andergassen, and P. Hansmann, "Real-space cluster dynamical mean-field theory: Center-focused extrapolation on the one- and two particle-levels," Phys. Rev. Res. **2**, 033476 (2020).

[122] A. Toschi, A. A. Katanin, and K. Held, "Dynamical vertex approximation: A step beyond dynamical mean-field theory," Phys. Rev. B **75**, 045118 (2007).

[123] T. Ayral and O. Parcollet, "Mott physics and spin fluctuations: A unified framework," Phys. Rev. B **92**, 115109 (2015).

[124] T. Ayral and O. Parcollet, "Mott physics and spin fluctuations: A functional viewpoint," Phys. Rev. B **93**, 235124 (2016).

[125] J. Vučičević, T. Ayral, and O. Parcollet, "Trilex and gw+edmft approach to d-wave superconductivity in the hubbard model," Phys. Rev. B **96**, 104504 (2017).

[126] A. N. Rubtsov, M. I. Katsnelson, and A. I. Lichtenstein, "Dual fermion approach to nonlocal correlations in the hubbard model," Phys. Rev. B **77**, 033101 (2008).

[127] A. N. Rubtsov, M. I. Katsnelson, A. I. Lichtenstein, and A. Georges, "Dual fermion approach to the two-dimensional hubbard model: Antiferromagnetic fluctuations and fermi arcs," Phys. Rev. B **79**, 045133 (2009).

[128] H. Hafermann, G. Li, A. N. Rubtsov, M. I. Katsnelson, A. I. Lichtenstein, and H. Monien, "Efficient perturbation theory for quantum lattice models," Phys. Rev. Lett. **102**, 206401 (2009).

[129] A. Rubtsov, M. Katsnelson, and A. Lichtenstein, "Dual boson approach to collective excitations in correlated fermionic systems," Annals of Physics **327**, 1320–1335 (2012).

[130] E. G. C. P. van Loon, A. I. Lichtenstein, M. I. Katsnelson, O. Parcollet, and H. Hafermann, "Beyond extended dynamical mean-field theory: Dual boson approach to the two-dimensional extended hubbard model," Phys. Rev. B **90**, 235135 (2014).

[131] E. A. Stepanov, E. G. C. P. van Loon, A. A. Katanin, A. I. Lichtenstein, M. I. Katsnelson, and A. N. Rubtsov, "Self-consistent dual boson approach to single-particle and collective excitations in correlated systems," Phys. Rev. B **93**, 045107 (2016).

[132] Y.M. Vilk and A.-M.S. Tremblay, "Non-perturbative many-body approach to the hubbard model and single-particle pseudogap," J. Phys. I France **7**, 1309–1368 (1997).

[133] A. M. S. Tremblay, "Two-particle-Self-Consistent Approach for the Hubbard model," in *Strongly Correlated Systems: Theoretical Methods*, edited by F. Mancini and A. Avella (Springer series, 2012) Chap. 13, pp. 409–453.

[134] W. Metzner, M. Salmhofer, C. Honerkamp, V. Meden, and K. Schönhammer, "Functional renormalization group approach to correlated fermion systems," Rev. Mod. Phys. **84**, 299–352 (2012).

[135] C. De Dominicis and P. C. Martin, "Stationary entropy principle and renormalization in normal and superfluid systems. ii. diagrammatic formulation," Journal of Mathematical Physics **5**, 31–59 (1964).

[136] N. E. Bickers, "Self-consistent many-body theory for condensed matter systems," in *Theoretical Methods for Strongly Correlated Electrons*, edited by D. Sénéchal, A.-M. Trembly, and C. Bourbonnais (Springer-Verlag New York Berlin Heidelbert, 2004) Chap. 6, pp. 237–296.

[137] C. Hille, D. Rohe, C. Honerkamp, and S. Andergassen, "Pseudogap opening in the two-dimensional Hubbard model: A functional renormalization group analysis," Phys. Rev. Research **2**, 033068 (2020).

[138] V. M. Galitskii and A. B. Migdal, "Application of quantum field theoretical methods to the many-body problem," Sov. Phys. JETP **34**, 139 (1958).

[139] A. Georges and W. Krauth, "Physical properties of the half-filled Hubbard model in infinite dimensions," Phys. Rev. B **48**, 7167–7182 (1993).

[140] A.-M. Daré, L. Raymond, G. Albinet, and A.-M. S. Tremblay, "Interaction-induced adiabatic cooling for antiferromagnetism in optical lattices," Phys. Rev. B **76**, 064402 (2007).

[141] L. Fratino, P. Sémon, M. Charlebois, G. Sordi, and A.-M. S. Tremblay, "Signatures of the mott transition in the antiferromagnetic state of the two-dimensional hubbard model," Phys. Rev. B **95**, 235109 (2017).

[142] S. Chakravarty, B. I. Halperin, and D. R. Nelson, "Low-temperature behavior of two-dimensional quantum antiferromagnets," Phys. Rev. Lett. **60**, 1057–1060 (1988).

[143] S. Chakravarty, B. I. Halperin, and D. R. Nelson, "Two-dimensional quantum Heisenberg antiferromagnet at low temperatures," Phys. Rev. B **39**, 2344–2371 (1989).

[144] K. Borejsza and N. Dupuis, "Antiferromagnetism and single-particle properties in the two-dimensional half-filled hubbard model: Slater vs. mott-heisenberg," Europhysics Letters **63**, 722 (2003).

[145] K. Borejsza and N. Dupuis, "Antiferromagnetism and single-particle properties in the two-dimensional half-filled Hubbard model: A nonlinear sigma model approach," Phys. Rev. B **69**, 085119 (2004).

[146] T. A. Maier, M. Jarrell, T. C. Schulthess, P. R. C. Kent, and J. B. White, "Systematic study of *d*-wave superconductivity in the 2d repulsive hubbard model," Phys. Rev. Lett. **95**, 237001 (2005).

[147] L. S. Ornstein and F. Zernike, "Accidental deviations of density and opalescence at the critical point of a single substance," Proc. Akad. Sci. **17**, 793 (1916).

[148] S. Moukouri, S. Allen, F. Lemay, B. Kyung, D. Poulin, Y. M. Vilk, and A.-M. S. Tremblay, "Many-body theory versus simulations for the pseudogap in the hubbard model," Phys. Rev. B **61**, 7887–7892 (2000).

[149] Y. M. Vilk and A.-M. S. Tremblay, "Destruction of fermi-liquid quasiparticles in two dimensions by critical fluctuations," Europhysics Letters **33**, 159 (1996).

[150] G. Sangiovanni, A. Toschi, E. Koch, K. Held, M. Capone, C. Castellani, O. Gunnarsson, S.-K. Mo, J. W. Allen, H.-D. Kim, A. Sekiyama, A. Yamasaki, S. Suga, and P. Metcalf, "Static versus dynamical mean-field theory of mott antiferromagnets," Phys. Rev. B **73**, 205121 (2006).

[151] D. Jaksch and P. Zoller, "The cold atom hubbard toolbox," Annals of Physics **315**, 52–79 (2005), special Issue.

[152] D. Greif, T. Uehlinger, G. Jotzu, L. Tarruell, and T. Esslinger, "Short-range quantum magnetism of ultracold fermions in an optical lattice," Science **340**, 1307–1310 (2013).

[153] R. A. Hart, P. M. Duarte, T.-L. Yang, X. Liu, T. Paiva, E. Khatami, R. T. Scalettar, N. Trivedi, D. A. Huse, and R. G. Hulet, "Observation of antiferromagnetic correlations in the hubbard model with ultracold atoms," Nature **519**, 211–214 (2015).

[154] J. E. Hirsch, "Simulations of the three-dimensional hubbard model: Half-filled band sector," Phys. Rev. B **35**, 1851–1859 (1987).

[155] A.-M. Daré, Y. M. Vilk, and A. M. S. Tremblay, "Crossover from two- to three-dimensional critical behavior for nearly antiferromagnetic itinerant electrons," Phys. Rev. B **53**, 14236–14251 (1996).

[156] A.-M. Daré and G. Albinet, "Magnetic properties of the three-dimensional hubbard model at half filling," Phys. Rev. B **61**, 4567–4575 (2000).

[157] R. Staudt, M. Dzierzawa, and A. Muramatsu, "Phase diagram of the three-dimensional hubbard model at half filling," The European Physical Journal B **17**, 411–415 (2000).

[158] T. Paiva, Y. L. Loh, M. Randeria, R. T. Scalettar, and N. Trivedi, "Fermions in 3d optical lattices: Cooling protocol to obtain antiferromagnetism," Phys. Rev. Lett. **107**, 086401 (2011).

[159] E. Kozik, E. Burovski, V. W. Scarola, and M. Troyer, "Néel temperature and thermodynamics of the half-filled three-dimensional hubbard model by diagrammatic determinant monte carlo," Phys. Rev. B **87**, 205102 (2013).

[160] C. Lenihan, A. J. Kim, F. Šimkovic, and E. Kozik, "Evaluating second-order phase transitions with diagrammatic monte carlo: Néel transition in the doped three-dimensional hubbard model," Phys. Rev. Lett. **129**, 107202 (2022).

[161] G. Rohringer, A. Toschi, A. Katanin, and K. Held, "Critical Properties of the Half-Filled Hubbard Model in Three Dimensions," Phys. Rev. Lett. **107**, 256402 (2011).

[162] T. Schäfer, A. Toschi, and J. M. Tomczak, "Separability of dynamical and nonlocal correlations in three dimensions," Phys. Rev. B **91**, 121107 (2015).

[163] J. Stobbe and G. Rohringer, "Consistency of potential energy in the dynamical vertex approximation," Phys. Rev. B **106**, 205101 (2022).

[164] D. Hirschmeier, H. Hafermann, E. Gull, A. I. Lichtenstein, and A. E. Antipov, "Mechanisms of finite-temperature magnetism in the three-dimensional Hubbard model," Phys. Rev. B **92**, 144409 (2015).

[165] P. R. C. Kent, M. Jarrell, T. A. Maier, and T. Pruschke, "Efficient calculation of the antiferromagnetic phase diagram of the three-dimensional hubbard model," Phys. Rev. B **72**, 060411 (2005).

[166] A. I. Lichtenstein and M. I. Katsnelson, "Antiferromagnetism and d-wave superconductivity in cuprates: A cluster dynamical mean-field theory," Phys. Rev. B **62**, R9283–R9286 (2000).

[167] G. Kotliar, S. Y. Savrasov, G. Pálsson, and G. Biroli, "Cellular dynamical mean field approach to strongly correlated systems," Phys. Rev. Lett. **87**, 186401 (2001).

[168] S. Fuchs, E. Gull, M. Troyer, M. Jarrell, and T. Pruschke, "Spectral properties of the three-dimensional hubbard model," Phys. Rev. B **83**, 235113 (2011).

[169] S. Fuchs, E. Gull, L. Pollet, E. Burovski, E. Kozik, T. Pruschke, and M. Troyer, "Thermodynamics of the 3d hubbard model on approaching the néel transition," Phys. Rev. Lett. **106**, 030401 (2011).

[170] L. Fratino, M. Charlebois, P. Sémon, G. Sordi, and A.-M. S. Tremblay, "Effects of interaction strength, doping, and frustration on the antiferromagnetic phase of the two-dimensional hubbard model," Phys. Rev. B **96**, 241109 (2017).

[171] J. Ehrlich and C. Honerkamp, "Functional renormalization group for fermion lattice models in three dimensions: Application to the hubbard model on the cubic lattice," Phys. Rev. B **102**, 195108 (2020).

[172] M. Campostrini, M. Hasenbusch, A. Pelissetto, P. Rossi, and E. Vicari, "Critical exponents and equation of state of the three-dimensional Heisenberg universality class," Phys. Rev. B **65**, 144520 (2002).

[173] T. Schäfer, A. A. Katanin, K. Held, and A. Toschi, "Interplay of Correlations and Kohn Anomalies in Three Dimensions: Quantum Criticality with a Twist," Phys. Rev. Lett. **119**, 046402 (2017).

[174] F. Werner, O. Parcollet, A. Georges, and S. R. Hassan, "Interaction-induced adiabatic cooling and antiferromagnetism of cold fermions in optical lattices," Phys. Rev. Lett. **95**, 056401 (2005).

[175] J. Van Kranendonk and J. H. Van Vleck, "Spin waves," Rev. Mod. Phys. **30**, 1–23 (1958).

[176] T. Pruschke and R. Zitzler, "From slater to mott–heisenberg physics: the antiferromagnetic phase of the hubbard model," Journal of Physics: Condensed Matter **15**, 7867 (2003).

[177] P. A. Lee, N. Nagaosa, and X.-G. Wen, "Doping a mott insulator: Physics of high-temperature superconductivity," Rev. Mod. Phys. **78**, 17–85 (2006).

[178] S. R. White and D. J. Scalapino, "Stripes on a 6-leg hubbard ladder," Phys. Rev. Lett. **91**, 136403 (2003).

[179] E. W. Huang, C. B. Mendl, H.-C. Jiang, B. Moritz, and T. P. Devereaux, "Stripe order from the perspective of the hubbard model," npj Quantum Materials **3**, 22 (2018).

[180] Y.-F. Jiang, J. Zaanen, T. P. Devereaux, and H.-C. Jiang, "Ground state phase diagram of the doped hubbard model on the four-leg cylinder," Phys. Rev. Res. **2**, 033073 (2020).

[181] K. Ido, T. Ohgoe, and M. Imada, "Competition among various charge-inhomogeneous states and *d*-wave superconducting state in hubbard models on square lattices," Phys. Rev. B **97**, 045138 (2018).

[182] S. Sorella, "The phase diagram of the hubbard model by variational auxiliary field quantum monte carlo," Preprint **arXiv**, 2101.07045 (2021).

[183] H. Xu, H. Shi, E. Vitali, M. Qin, and S. Zhang, "Stripes and spin-density waves in the doped two-dimensional hubbard model: Ground state phase diagram," Phys. Rev. Res. **4**, 013239 (2022).

[184] G. Knizia and G. K.-L. Chan, "Density matrix embedding: A simple alternative to dynamical mean-field theory," Phys. Rev. Lett. **109**, 186404 (2012).

[185] B.-X. Zheng and G. K.-L. Chan, "Ground-state phase diagram of the square lattice hubbard model from density matrix embedding theory," Phys. Rev. B **93**, 035126 (2016).

[186] R. Peters and N. Kawakami, "Spin density waves in the hubbard model: A dmft approach," Phys. Rev. B **89**, 155134 (2014).

[187] T. I. Vanhala and P. Törmä, "Dynamical mean-field theory study of stripe order and d-wave superconductivity in the two-dimensional hubbard model," Phys. Rev. B **97**, 075112 (2018).

[188] S. S. Dash and D. Sénéchal, "Charge- and pair-density-wave orders in the one-band hubbard model from dynamical mean field theory," Phys. Rev. B **103**, 045142 (2021).

[189] J. Zaanen and O. Gunnarsson, "Charged magnetic domain lines and the magnetism of high-T_c oxides," Phys. Rev. B **40**, 7391–7394 (1989).

[190] K. Machida, "Magnetism in la2cuo4 based compounds," Physica C: Superconductivity **158**, 192–196 (1989).

[191] H. J. Schulz, "Incommensurate antiferromagnetism in the two-dimensional hubbard model," Phys. Rev. Lett. **64**, 1445–1448 (1990).

[192] M. Kato, K. Machida, H. Nakanishi, and M. Fujita, "Soliton lattice modulation of incommensurate spin density wave in two dimensional hubbard model -a mean field study-," Journal of the Physical Society of Japan **59**, 1047–1058 (1990).

[193] A.-M. S. Tremblay, B. Kyung, and D. Sénéchal, "Pseudogap and high-temperature superconductivity from weak to strong coupling. towards a quantitative theory (review article)," Low Temperature Physics **32**, 424–451 (2006).

[194] G. Kotliar, S. Y. Savrasov, K. Haule, V. S. Oudovenko, O. Parcollet, and C. A. Marianetti, "Electronic structure calculations with dynamical mean-field theory," Rev. Mod. Phys. **78**, 865–951 (2006).

[195] A. Macridin, M. Jarrell, T. Maier, P. R. C. Kent, and E. D'Azevedo, "Pseudogap and antiferromagnetic correlations in the hubbard model," Phys. Rev. Lett. **97**, 036401 (2006).

[196] K. Haule and G. Kotliar, "Strongly correlated superconductivity: A plaquette dynamical mean-field theory study," Phys. Rev. B **76**, 104509 (2007).

[197] M. Ferrero, P. S. Cornaglia, L. De Leo, O. Parcollet, G. Kotliar, and A. Georges, "Pseudogap opening and formation of fermi arcs as an orbital-selective mott transition in momentum space," Phys. Rev. B **80**, 064501 (2009).

[198] E. Gull, M. Ferrero, O. Parcollet, A. Georges, and A. J. Millis, "Momentum-space anisotropy and pseudogaps: A comparative cluster dynamical mean-field analysis of the doping-driven metal-insulator transition in the two-dimensional hubbard model," Phys. Rev. B **82**, 155101 (2010).

[199] O. Gunnarsson, T. Schäfer, J. P. F. LeBlanc, E. Gull, J. Merino, G. Sangiovanni, G. Rohringer, and A. Toschi, "Fluctuation diagnostics of the electron self-energy: Origin of the pseudogap physics," Phys. Rev. Lett. **114**, 236402 (2015).

[200] W. Wu, M. S. Scheurer, S. Chatterjee, S. Sachdev, A. Georges, and M. Ferrero, "Pseudogap and fermi-surface topology in the two-dimensional hubbard model," Phys. Rev. X **8**, 021048 (2018).

[201] F. Krien, P. Worm, P. Chalupa, A. Toschi, and K. Held, "Spin scattering turns complex at strong coupling: the key to pseudogap and fermi arcs in the hubbard model," Preprint **arXiv**, 2107.06529 (2021).

[202] D. Vilardi, C. Taranto, and W. Metzner, "Dynamically enhanced magnetic incommensurability: Effects of local dynamics on nonlocal spin correlations in a strongly correlated metal," Phys. Rev. B **97**, 235110 (2018).

[203] M. Raczkowski and F. F. Assaad, "Melting of stripe phases and its signature in the single-particle spectral function," Phys. Rev. B **82**, 233101 (2010).

[204] E. W. Huang, C. B. Mendl, S. Liu, S. Johnston, H.-C. Jiang, B. Moritz, and T. P. Devereaux, "Numerical evidence of fluctuating stripes in the normal state of high-t_c cuprate superconductors," Science **358**, 1161–1164 (2017).

[205] P. Mai, S. Karakuzu, G. Balduzzi, S. Johnston, and T. A. Maier, "Intertwined spin, charge, and pair correlations in the two-dimensional hubbard model in the thermodynamic limit," Proceedings of the National Academy of Sciences **119**, e2112806119 (2022).

[206] B. Xiao, Y.-Y. He, A. Georges, and S. Zhang, "Temperature dependence of spin and charge orders in the doped two-dimensional hubbard model," Phys. Rev. X **13**, 011007 (2023).

[207] A. Wietek, Y.-Y. He, S. R. White, A. Georges, and E. M. Stoudenmire, "Stripes, antiferromagnetism, and the pseudogap in the doped hubbard model at finite temperature," Phys. Rev. X **11**, 031007 (2021).

[208] F. i. c. v. IV, R. Rossi, and M. Ferrero, "Two-dimensional hubbard model at finite temperature: Weak, strong, and long correlation regimes," Phys. Rev. Res. **4**, 043201 (2022).

[209] P. Werner and A. J. Millis, "Doping-driven mott transition in the one-band hubbard model," Phys. Rev. B **75**, 085108 (2007).

[210] D. Riegler, M. Klett, T. Neupert, R. Thomale, and P. Wölfle, "Slave-boson analysis of the two-dimensional hubbard model," Phys. Rev. B **101**, 235137 (2020).

[211] T. Holder and W. Metzner, "Incommensurate nematic fluctuations in two-dimensional metals," Phys. Rev. B **85**, 165130 (2012).

[212] T. A. Sedrakyan and A. V. Chubukov, "Pseudogap in underdoped cuprates and spin-density-wave fluctuations," Phys. Rev. B **81**, 174536 (2010).

[213] A. V. Chubukov, "Kohn-luttinger effect and the instability of a two-dimensional repulsive fermi liquid at t=0," Phys. Rev. B **48**, 1097–1104 (1993).

[214] E. Pavarini, I. Dasgupta, T. Saha-Dasgupta, O. Jepsen, and O. K. Andersen, "Band-structure trend in hole-doped cuprates and correlation with t_{cmax}," Phys. Rev. Lett. **87**, 047003 (2001).

[215] A. V. Balatsky and P. Bourges, "Linear dependence of peak width in $\chi(q,\omega)$ vs T_c for $\mathrm{yba_2cu_3O_{6+x}}$ superconductors," Phys. Rev. Lett. **82**, 5337–5340 (1999).

[216] K. Yamada, C. H. Lee, K. Kurahashi, J. Wada, S. Wakimoto, S. Ueki, H. Kimura, Y. Endoh, S. Hosoya, G. Shirane, R. J. Birgeneau, M. Greven, M. A. Kastner, and Y. J. Kim, "Doping dependence of the spatially modulated dynamical spin correlations and the superconducting-transition temperature in $\mathrm{la_{2-x}sr_xcuo_4}$," Phys. Rev. B **57**, 6165–6172 (1998).

[217] R. J. Birgeneau, C. Stock, J. M. Tranquada, and K. Yamada, "Magnetic neutron scattering in hole-doped cuprate superconductors," Journal of the Physical Society of Japan **75**, 111003 (2006).

[218] J. Li, M. Wallerberger, and E. Gull, "Diagrammatic monte carlo method for impurity models with general interactions and hybridizations," Phys. Rev. Res. **2**, 033211 (2020).

[219] G. Cohen, E. Gull, D. R. Reichman, and A. J. Millis, "Taming the dynamical sign problem in real-time evolution of quantum many-body problems," Phys. Rev. Lett. **115**, 266802 (2015).

[220] A. E. Antipov, Q. Dong, J. Kleinhenz, G. Cohen, and E. Gull, "Currents and green's functions of impurities out of equilibrium: Results from inchworm quantum monte carlo," Phys. Rev. B **95**, 085144 (2017).

[221] Q. Dong, I. Krivenko, J. Kleinhenz, A. E. Antipov, G. Cohen, and E. Gull, "Quantum monte carlo solution of the dynamical mean field equations in real time," Phys. Rev. B **96**, 155126 (2017).

[222] I. Krivenko, J. Kleinhenz, G. Cohen, and E. Gull, "Dynamics of kondo voltage splitting after a quantum quench," Phys. Rev. B **100**, 201104 (2019).

[223] J. Kleinhenz, I. Krivenko, G. Cohen, and E. Gull, "Dynamic control of nonequilibrium metal-insulator transitions," Phys. Rev. B **102**, 205138 (2020).

[224] J. Kleinhenz, I. Krivenko, G. Cohen, and E. Gull, "Kondo cloud in a one-dimensional nanowire," Phys. Rev. B **105**, 085126 (2022).

[225] A. Taheridehkordi, S. H. Curnoe, and J. P. F. LeBlanc, "Algorithmic matsubara integration for hubbard-like models," Phys. Rev. B **99**, 035120 (2019).

[226] A. Taheridehkordi, S. H. Curnoe, and J. P. F. LeBlanc, "Optimal grouping of arbitrary diagrammatic expansions via analytic pole structure," Phys. Rev. B **101**, 125109 (2020).

[227] A. Taheridehkordi, S. H. Curnoe, and J. P. F. LeBlanc, "Algorithmic approach to diagrammatic expansions for real-frequency evaluation of susceptibility functions," Phys. Rev. B **102**, 045115 (2020).

[228] J. Vučičević and M. Ferrero, "Real-frequency diagrammatic monte carlo at finite temperature," Phys. Rev. B **101**, 075113 (2020).

[229] J. Vučičević, P. Stipsić, and M. Ferrero, "Analytical solution for time integrals in diagrammatic expansions: Application to real-frequency diagrammatic monte carlo," Phys. Rev. Res. **3**, 023082 (2021).

[230] M. D. Burke, M. Grandadam, and J. P. F. LeBlanc, "Renormalized perturbation theory for fast evaluation of feynman diagrams on the real frequency axis," Phys. Rev. B **107**, 115151 (2023).

[231] P. Werner, T. Oka, and A. J. Millis, "Diagrammatic monte carlo simulation of nonequilibrium systems," Phys. Rev. B **79**, 035320 (2009).

[232] C. Bertrand, O. Parcollet, A. Maillard, and X. Waintal, "Quantum monte carlo algorithm for out-of-equilibrium green's functions at long times," Phys. Rev. B **100**, 125129 (2019).

[233] C. Bertrand, S. Florens, O. Parcollet, and X. Waintal, "Reconstructing nonequilibrium regimes of quantum many-body systems from the analytical structure of perturbative expansions," Phys. Rev. X **9**, 041008 (2019).

[234] M. Maček, P. T. Dumitrescu, C. Bertrand, B. Triggs, O. Parcollet, and X. Waintal, "Quantum quasi-monte carlo technique for many-body perturbative expansions," Phys. Rev. Lett. **125**, 047702 (2020).

[235] C. Bertrand, D. Bauernfeind, P. T. Dumitrescu, M. Maček, X. Waintal, and O. Parcollet, "Quantum quasi monte carlo algorithm for out-of-equilibrium green functions at long times," Phys. Rev. B **103**, 155104 (2021).

[236] Y. Núñez Fernández, M. Jeannin, P. T. Dumitrescu, T. Kloss, J. Kaye, O. Parcollet, and X. Waintal, "Learning feynman diagrams with tensor trains," Phys. Rev. X **12**, 041018 (2022).

[237] R. Peng, J. Gray, and G. K.-L. Chan, "Arithmetic circuit tensor networks, multivariable function representation, and high-dimensional integration," Phys. Rev. Res. **5**, 013156 (2023).

[238] I. Oseledets and E. Tyrtyshnikov, "Tt-cross approximation for multidimensional arrays," Linear Algebra and its Applications **432**, 70–88 (2010).

[239] S. Dolgov and D. Savostyanov, "Parallel cross interpolation for high-precision calculation of high-dimensional integrals," Computer Physics Communications **246**, 106869 (2020).

[240] L. I. Vysotsky, A. V. Smirnov, and E. E. Tyrtyshnikov, "Tensor-train numerical integration of multivariate functions with singularities," Lobachevskii Journal of Mathematics **42**, 1608–1621 (2021).